UNIVERSITY OF OKLAHOMA

GRADUATE COLLEGE

DEVELOPMENT AND CHARACTERIZATION OF A HIGH ENERGY PHASE CONTRAST X-RAY IMAGING SYSTEM PROTOTYPE

A DISSERTATION

SUBMITTED TO THE GRADUATE FACULTY

in partial fulfillment of the requirements for the

Degree of

DOCTOR OF PHILOSOPHY

By

MOLLY DONOVAN WONG
Norman, Oklahoma
2011

DEVELOPMENT AND CHARACTERIZATION OF A HIGH ENERGY PHASE CONTRAST X-RAY IMAGING SYSTEM PROTOTYPE

A DISSERTATION APPROVED FOR THE
SCHOOL OF ELECTRICAL AND COMPUTER ENGINEERING

BY

_____
Dr. Hong Liu, Chair

_____
Dr. John Jiang

_____
Dr. Joseph Havlicek

_____
Dr. Chen Ling

_____
Dr. Monte Tull

This dissertation is dedicated to my husband Philip, whose never-ending love, support, encouragement and faith have given me the confidence and the strength to achieve my dreams. Words cannot express my gratitude for being blessed with such a wonderful husband.

Acknowledgements

This work was supported in part by grants from the National Institute of Health (R01 CA104773), as well as a Department of Defense Breast Cancer research grant (W81XWH-08-1-0613). I would also like to gratefully acknowledge the support of the Charles and Jean Smith Chair endowment fund, as well as the University of Oklahoma Office of the Vice President for Research.

In addition, words cannot express my gratitude to Dr. Hong Liu, who has not only provided the ability and support to perform this innovative research in such a knowledge-rich environment, but has also tremendously benefited my research and individual growth through his tireless mentoring and encouragement.

I would also like to gratefully acknowledge the members of our research team: Dr. Yuhua Li, Dr. Da Zhang and Dr. Xingwei Wang, who have all provided a tremendous example of dedication and diligence, as well as continued support and help throughout this research.

Finally, I would like to express my gratitude to the other members of my committee, Dr. John Jiang, Dr. Joseph Havlicek, Dr. Chen Ling and Dr. Monte Tull, for their unbelievable help and encouragement throughout my research. I would like to especially thank Drs. Havlicek and Tull for their continued support and guidance through this degree, as well as my masters and undergraduate degrees.

Table of Contents

List of Tables viii
List of Figures ix
Abstract xiii
1 Introduction 1
1.1 Significance 1
1.2 Organization of Dissertation 4
2 Research Methods 6
2.1 Image Quality 6
2.1.1 Contrast, Noise and Resolution 6
2.1.2 Image Quality Concepts 8
2.1.3 Subjective Measurements 15
2.1.4 Objective Measurements 21
2.1.5 Clinical Measurements 24
2.2 Statistical Analysis 26
2.2.1 Statistical Comparison Methods 26
2.2.2 Error Analysis in Measurements and Calculations 28
2.3 Phase Contrast Imaging 30
2.3.1 Theory 30
2.3.2 Background 31
2.3.3 Potential Advantages 33
2.4 Radiation Dose 38
2.4.1 Introduction 38
2.4.2 Calculation 39
2.4.3 D_{gN} Factors 40
3 Development and Characterization of a Low Energy Phase Contrast System Prototype 44
3.1 System Design 44
3.1.1 X-ray Source Specifications 44
3.1.2 Image Detection Systems 44
3.1.3 Geometry of the Imaging System 45
3.1.4 Development of System Alignment Procedure 46
3.2 Image Quality Evaluation 49
3.2.1 CDMAM Observer Study 49
3.2.2 ACR Observer Study 52
3.2.3 Tissue-equivalent Phantom Image Comparison 54

4 Optimization of the MTF Edge Algorithm 58
4.1 Background 58
4.2 Experimental Design 60
4.3 Development of the Optimal Algorithm 61
4.3.1 Edge Equation 62
4.3.2 ESF Calculation 65
4.3.3 ESF Smoothing 68
4.3.4 LSF Calculation 73
4.3.5 LSF Smoothing 75
5 Comprehensive Error Analysis of Photon Fluence Contribution to the DQE 81
5.1 Background 81
5.2 Experimental Design 83
5.3 Error Analysis 84
5.3.1 Exposure Measurements 86
5.3.2 Spectrum Measurements 97
5.3.3 Photon Fluence 102
5.3.4 DQE 103
6 Effects of X-ray Beam Hardening on the DQE and Radiation Dose 108
6.1 Introduction 108
6.1.1 Beam Hardening 108
6.2 Preliminary Feasibility Study 109
6.2.1 Experimental Design 110
6.2.2 Results 114
6.2.3 Discussion 117
6.3 Comprehensive Investigation 118
6.3.1 Experimental Design 118
6.3.2 Results 121
6.3.3 Conclusion 126
7 Preliminary Feasibility of a High Energy Phase Contrast System Prototype 128
7.1 Introduction 128
7.2 Experimental Design 129
7.2.1 Joint Parameter Optimization 129
7.2.2 System and Measurement Components 130
7.2.3 Phantoms 132
7.3 Results 135
7.3.1 Wax Insert of ACR Phantom 135
7.3.2 Full ACR Phantom 137
7.3.3 Contrast-Detail Phantom 139
7.3.4 Acrylic Edge Phantom 141

7.3.5 Tissue-Equivalent Phantom 146
7.4 Discussion 148
8 Image Quality Comparison of High Energy Phase Contrast to High and Low Energy Conventional Images 150
8.1 Introduction 150
8.2 High Energy Conventional 151
8.2.1 Experimental Design 151
8.2.2 Results 152
8.3 Low Energy Conventional 156
8.3.1 Experimental Design 156
8.3.2 Results 158
8.4 Discussion 162
9 Image Quality and Dose Comparison of High Energy Phase Contrast with Low Energy Conventional Imaging 164
9.1 Introduction 164
9.2 Experimental Design 164
9.3 Results 167
9.3.1 Full ACR Phantom 167
9.3.2 Contrast-Detail Phantom 169
9.3.3 Acrylic Edge Phantom 171
9.3.4 Tissue-Equivalent Phantom 173
9.4 Conclusion 174
10 Conclusion 176
10.1 Summary 176
10.2 Future Research Direction 180
Bibliography 183

List of Tables

Table 1: Comparison of ACR observer study results for three sets of comparison images between phase contrast and conventional modes. 54

Table 2: Results of calculations of the measured exposure X_i. 88

Table 3: The results of the measurements of *R1* and *R2* with a standard ruler. 91

Table 4: Comparison of the calculation of the magnification factors M_r and M_i determined by the ruler and image methods, respectively. 92

Table 5: Results of the following image method calculations: the number of pixels representing the magnified ion chamber in the image (L_i), and the actual diameter of the chamber measured by a caliper (D_a). 94

Table 6: Comparison of the exposure calculation results determined by the ruler and image methods. 95

Table 7: Results of the calculations of the mean and variance values for the photon fluence per unit exposure. 100

Table 8: Photon fluence calculation results, including mean, total error and relative error, which were calculated with the exposure and spectrum measurement results. 103

Table 9: Comparison of the average glandular dose (D_g) measurements corresponding to the four levels of beam hardening in the preliminary study. 117

Table 10: Exposure times for the range of object/ filter combinations investigated in this study, which were selected individually to provide a constant detector entrance exposure of 10 mR. 120

Table 11: Comparison of the photon fluence (q) values for the ten object/filter combinations investigated in this study. 124

Table 12: Comparison of the average glandular dose (D_g) measurements corresponding to the five levels of beam hardening in the comprehensive study. 126

Table 13: Exposure times for the range of kV and *M* combinations investigated, which were selected individually to maintain a constant object entrance exposure of 1 R. 131

Table 14: Comparison of wax insert ACR scores from the observer study of the images corresponding to the range of x-ray energy/magnification factor combinations investigated. 137

Table 15: Comparison of full ACR scores from the observer study of the images corresponding to the range of x-ray energy/magnification factor combinations investigated. 139

Table 16: Experimental settings for the comparison of high energy phase contrast imaging and low energy conventional imaging, which were selected to maintain a constant object entrance exposure of 1 R and a constant focal spot size of 7 µm. 157

Table 17: Average glandular dose calculation values for the comparison of high energy phase contrast imaging and low energy conventional imaging. A target D_g value was selected, and the exposure times were determined separately for each mode in order to deliver the corresponding absorbed dose. 166

Table 18: Comparison of ACR scores for the high energy phase contrast and low energy conventional images of the ACR phantom. 168

List of Figures

Figure 1: Illustration of the response of an imaging system to: (a) a line stimulus (LSF), and (b) an edge stimulus (ESF). 11

Figure 2: Modulation transfer function of an imaging system. 12

Figure 3: Contrast-detail phantom (A) and corresponding x-ray image (B)....16

Figure 4: Photograph of the CDMAM Phantom. Each matrix square for a specific thickness and diameter consists not only of an object in the center of the square, as in standard contrast-detail phantoms, but also an object in one of the corners selected at random. 19

Figure 5: Illustration of the test objects represented in the Nuclear Associates ACR phantom 18-220, which includes groups of fibers, specks and masses. 20

Figure 6: Detective quantum efficiency (DQE) calculated for an imaging system. 24

Figure 7: Illustration of the x-ray configurations for (a) conventional imaging and (b) phase contrast imaging. 33

Figure 8: Comparison of CDMAM images acquired at 60 kV, 167 µA and 30 s in (a) conventional mode, and (b) phase contrast mode. 50

Figure 9: Comparison of contrast-detail curves generated from the observer study comparing conventional and phase contrast images at 60 kV, 167 µA and 30 s. 51

Figure 10: Comparison of ACR images acquired at 40 kV, 250 µA and 30 s in (a) conventional mode, and (b) phase contrast mode. 53

Figure 11: Comparison of 1 mm thick chicken breast images acquired at 40 kV, 250 µA and 30 s in (a) conventional mode, and (b) phase contrast mode. 55

Figure 12: Comparison of 4 mm thick chicken breast images acquired at 40 kV, 250 µA and 30 s in (a) conventional mode, and (b) phase contrast mode. 56

Figure 13: Flow Chart of Processing Steps in MTF Edge Algorithm 62

Figure 14: Comparison of edge equation lines determined through the following methods: (a) linear regression, (b) Hough transformation, and (c) Canny edge detection. 64

Figure 15: Illustration of ESF curves resulting from different ROI sizes of (a) 30, (b) 60 and (c) 120 rows and columns around the edge. 66

Figure 16: Illustration of ESF curves resulting from ROI sizes of 60 columns and (a) 30, (b) 60, and (c) 120 rows across the edge. 67

Figure 17: Illustration of ESF curves resulting from ROI sizes of 60 rows and (a) 30, (b) 60, and (c) 120 columns across the edge. 68

Figure 18: ESF smoothing with data binning method in (a) the upper tail and (b) the edge transition, using a range of percentages of pixel pitch for bin size. 70

Figure 19: ESF smoothing with average filter method in (a) the upper tail and (b) the edge transition, using a range of window sizes. 71

Figure 20: ESF smoothing with median filter method in (a) the upper tail and (b) the edge transition, using a range of window sizes. 72

Figure 21: ESF smoothing with polynomial fit method in (a) the upper tail and (b) the edge transition. 72

Figure 22: Results from ESF smoothing with a three-step iterative process of data binning, polynomial fitting and median filter smoothing. The entire ESF curve is given in (a) and the data integrity along the edge transition is illustrated in (b). 73

Figure 23: LSF curves calculated through finite element differentiation with (a) two element kernels, and (b) three element kernels. 75

Figure 24: Comparisons of LSF smoothing methods: (a) cropping the tails, (b) median filtering, (c) average filtering, and (d) applying a polynomial fit method. 78

Figure 25: Updated flow chart of the MTF edge algorithm steps indicating the optimal method selected for each step. 79

Figure 26: Illustration of the relationship between the number of exposure measurements acquired and the random error within the measurements. 89

Figure 27: Illustration of the x-ray configuration utilized for calculation of the magnification factor by the ruler method. 90

Figure 28: Illustration of the relationship between *R2*, which represents the SID, and the resulting variance in the magnification calculation by the ruler method. 96

Figure 29: Illustration of the relationship between the number of spectrum measurements acquired and the random error within the measurements. 101

Figure 30: Comparison of an individual spectrum measurement (gray) with a mean spectrum from 40 measurements (black). 102

Figure 31: Detective quantum efficiency (DQE) determined with the mean photon fluence value calculated in this study. 104

Figure 32: Illustration of the error contributed to the DQE by the photon fluence calculation for each frequency represented in the DQE. 105

Figure 33: Illustrations of the x-ray configurations utilized in this study for: (a) measurement of the detective quantum efficiency, and (b) measurement of the average glandular dose. 110

Figure 34: Comparison of the x-ray spectra for the four levels of beam hardening: no object, small BR12 (0.5 cm), medium BR12 (1 cm), and large BR12 (2 cm). 114

Figure 35: Comparison of the MTF values corresponding to the levels of beam hardening. 115

Figure 36: Comparison of the NPS values corresponding to the levels of beam hardening. 115

Figure 37: Comparison of the DQE values corresponding to the levels of beam hardening. 116

Figure 38: Illustration of the x-ray configuration utilized for the DQE and average glandular dose calculations in this study. 119

Figure 39: Comparison of the x-ray spectra for the range of beam hardening levels. The spectra were acquired at 60 kV, 20 W (a) without an object in the path of the x-ray beam, and (b) with the 5 cm BR12 object in the path. 122

Figure 40: Comparison of the MTF for the range of beam hardening levels (a) without an object in the path of the x-ray beam, and (b) with the 5 cm BR12 object in the path. 122

Figure 41: Comparison of the NPS for the range of beam hardening levels (a) without an object in the path of the x-ray beam, and (b) with the 5 cm BR12 object in the path. 123

Figure 42: Comparison of the NEQ for the range of beam hardening levels (a) without an object in the path of the x-ray beam, and (b) with the 5 cm BR12 object in the path. 124

Figure 43: Comparison of the DQE for the range of beam hardening levels (a) without an object in the path of the x-ray beam, and (b) with the 5 cm BR12 object in the path. 125

Figure 44: The high energy phase contrast x-ray imaging system configuration utilized in this study. 130

Figure 45: Comparison of ACR wax insert phantom images, which were acquired at a magnification factor of 2.5 and an x-ray energy of (a) 100 kV, (b) 120 kV, and (c) 140 kV. 136

Figure 46: Comparison of full ACR phantom images, which were acquired at an x-ray energy of 100 kV and a magnification factor of (a) 2.0, (b) 2.5, and (c) 3.0. 138

Figure 47: Comparison of contrast-detail phantom images, which were acquired at an x-ray energy of 120 kV and a magnification factor of (a) 2.0, (b) 2.5, and (c) 3.0. 140

Figure 48: Comparison of contrast-detail curves generated from the phase contrast images corresponding to the range of x-ray energy/magnification factor combinations. 141

Figure 49: Comparison of acrylic edge phantom images, which were acquired at a magnification factor of 3.0 and an x-ray energy of (a) 100 kV, (b) 120 kV, and (c) 140 kV. 142

Figure 50: Comparison of acrylic edge images acquired at the following experimental settings providing similar entrance exposures: (left) conventional mode at 20 KV, 20W, 114s, and (right) phase contrast mode at 60 KV, 20 W, 10s. 143

Figure 51: Edge profiles determined from the comparison images in the previous figure: (left) conventional mode at 20 KV, 20W, 114s, in which no overshooting is indicated, and (right) phase contrast mode at 60 KV, 20 W, 10s, which clearly demonstrates the overshooting resulting from the phase contrast effect. 144

Figure 52: Comparison of edge profiles for an x-ray energy of 120 kV, which demonstrate the difference in the overshooting effect for the range of magnification factors. 145

Figure 53: Comparison of edge profiles for a magnification factor of 2.5, which demonstrates the difference in the overshooting effect for the range of magnification factors. 145

Figure 54: Comparison of edge profiles for the entire range of x-ray energies and magnification factors. 146

Figure 55: Comparison of tissue-equivalent phantom images, which were acquired at an x-ray energy of 140 kV and a magnification factor of (a) 2.0, (b) 2.5, and (c) 3.0. 148

Figure 56: Comparison of system configurations for (a) phase contrast imaging mode and (b) conventional imaging mode. The same *R1* value was utilized to facilitate comparison of phase contrast and conventional images with similar object entrance exposures. 151

Figure 57: Comparison of full ACR phantom images acquired at 100 kV and $M = 2$ in (a) phase contrast mode, and (b) conventional mode. 153

Figure 58: Comparison of full ACR phantom images acquired at 100 kV and $M = 2.5$ in (a) phase contrast mode, and (b) conventional mode. 154

Figure 59: Comparison of full ACR phantom images acquired at 100 kV and $M = 3$ in (a) phase contrast mode, and (b) conventional mode. 154

Figure 60: Comparison of tissue-equivalent phantom images acquired at 140 kV and $M = 2$ in (a) phase contrast mode, and (b) conventional mode. 155

Figure 61: Comparison of tissue-equivalent phantom images acquired at 140 kV and $M = 2.5$ in (a) phase contrast mode, and (b) conventional mode. 155

Figure 62: Comparison of tissue-equivalent phantom images acquired at 140 kV and $M = 3$ in (a) phase contrast mode, and (b) conventional mode. 156

Figure 63: Comparison of full ACR phantom images acquired at the following experimental settings: (a) 100 kV, 100 µA, 109s, *M* = 2.5 (phase contrast mode), and (b) 40 kV, 250 µA, 122s, *M* = 1 (conventional mode). 158

Figure 64: Comparison of contrast-detail phantom images acquired at the following experimental settings: (a) 100 kV, 100 µA, 109s, *M* = 2.5 (phase contrast mode), and (b) 40 kV, 250 µA, 122s, *M* = 1 (conventional mode). 159

Figure 65: Comparison of acrylic phantom images acquired at the following experimental settings: (a) 100 kV, 100 µA, 109s, *M* = 2.5 (phase contrast mode), and (b) 40 kV, 250 µA, 122s, *M* = 1 (conventional mode). 161

Figure 66: Edge profiles determined from the acrylic edge comparison images: (a) 100 kV, 100 µA, 109s, *M* = 2.5 (phase contrast mode), which clearly demonstrates the overshooting resulting from the phase contrast effect, and (b) 40 kV, 250 µA, 122s, *M* = 1 (conventional mode), in which no overshooting is indicated. 161

Figure 67: Comparison of tissue-equivalent phantom images acquired at the following experimental settings: (a) 100 kV, 100 µA, 109s, *M* = 2.5 (phase contrast mode), and (b) 40 kV, 250 µA, 122s, *M* = 1 (conventional mode). 162

Figure 68: Comparison of full ACR phantom images acquired at the following experimental settings: (a) 100 kV, 100 µA, 72s, *M* = 2.5 (phase contrast mode), and (b) 40 kV, 250 µA, 192s, *M* = 1 (conventional mode). 168

Figure 69: Comparison of contrast-detail phantom images acquired at the following experimental settings: (a) 100 kV, 100 µA, 72s, *M* = 2.5 (phase contrast mode), and (b) 40 kV, 250 µA, 192s, *M* = 1 (conventional mode). 170

Figure 70: Comparison of contrast-detail curves generated from the high energy phase contrast and low energy conventional phantom images. 171

Figure 71: Comparison of acrylic edge phantom images acquired at the following experimental settings: (a) 100 kV, 100 µA, 72s, *M* = 2.5 (phase contrast mode), and (b) 40 kV, 250 µA, 192s, *M* = 1 (conventional mode). 172

Figure 72: Edge profiles determined from the acrylic edge comparison images: (a) 100 kV, 100 µA, 72s, *M* = 2.5 (phase contrast mode), which clearly demonstrates the overshooting resulting from the phase contrast effect, and (b) 40 kV, 250 µA, 192s, *M* = 1 (conventional mode), in which no overshooting is indicated. 172

Figure 73: Comparison of tissue-equivalent phantom images acquired at the following experimental settings: (a) 100 kV, 100 µA, 72s, *M* = 2.5 (phase contrast mode), and (b) 40 kV, 250 µA, 192s, *M* = 1 (conventional mode). 174

Abstract

The field of mammography receives constant research attention focused on improving the balance between the benefits of cancer screening and the risks of harmful radiation to the patient. As a result, numerous advancements have been made throughout the history of mammography, which have not only improved the ability to detect cancer at an earlier stage, but also to diagnose previously undetectable cancer. Numerous clinical trials have demonstrated the decrease in mortality rates. Due to the potential for saving lives, along with the recent public concerns regarding radiation dose, significant research attention remains focused on investigating methods for further improving the detection capabilities and reducing the radiation dose. However, the similar absorption characteristics of normal and malignant tissue present a challenge in differentiating between them using conventional x-ray imaging. The current method for providing higher image quality involves utilizing anti-scatter grids and operating at much lower x-ray energies than other radiography fields, both of which result in an increased radiation dose. An emerging technology called phase contrast imaging, which is based not only on absorption but also the effects produced by x-ray phase changes, holds the potential to increase the x-ray energy and remove the grid without compromising the image quality, which could reduce the patient dose and thus benefit the field of mammography. Preliminary studies in phase contrast imaging at the same energy as conventional imaging have indicated the ability to reduce the radiation dose without negatively impacting the diagnosis capabilities. However, existing challenges in clinical implementation have prevented the

technology from further progress. The goal of the research presented in this dissertation comprises a thorough investigation of the potential of high energy phase contrast imaging to overcome these challenges and further reduce the radiation dose without decreasing the detection ability. Following an introductory chapter, Chapter 2 presents a detailed description of the necessary methods required to perform the dissertation research. The methods are separated into four categories: image quality, statistical methods, phase contrast imaging, and radiation dose. Chapters 3 through 6 encompass four preliminary studies accomplished to demonstrate a thorough understanding of the research methods, as well as to evaluate the feasibility of the research and corresponding motivation in the medical imaging field. The development and preliminary feasibility investigation of a high energy phase contrast imaging system prototype is presented in Chapter 7, followed by an image quality comparison to high and low energy conventional imaging with similar entrance exposures in Chapter 8. Chapter 9 presents a comprehensive image quality and dose comparison of high energy phase contrast and low energy conventional imaging. Finally, the summary and discussion of results are presented in Chapter 10, along with planned research direction for future studies.

This dissertation encompasses numerous original contributions, perhaps the most significant of which were the demonstration of the ability of phase contrast imaging to deliver acceptable image quality for detection and diagnosis at higher x-ray energies than investigated previously, as well as the comprehensive comparison of high energy phase contrast imaging with low energy conventional imaging. These

results clearly demonstrate the ability of phase contrast imaging to sustain the image quality improvement at high x-ray energies and for clinical thicknesses without an increase in the radiation dose. In addition, each of the preliminary studies involved the development of novel methods or techniques to improve existing procedures. First, the step-by-step optimization of the MTF algorithm presented in Chapter 4 was an original approach, which also included the application of new methods to several of the steps, resulting in an optimized algorithm with significantly improved accuracy. Next, Chapter 5 presented the development of a quantitative method to determine the error contributed to any calculated result by each of the represented components, as well as a new method for calculating the magnification factor that considerably reduces the error, especially for clinical systems. Chapter 6 presented the novel application of the existing method of beam hardening to reduce the radiation dose without affecting the detection capability, which holds the potential to greatly benefit mammography and related fields.

The research presented in this dissertation is a strong indication of the potential of high energy phase contrast imaging to dramatically benefit x-ray imaging fields such as mammography by improving the ability to detect and diagnose diseases at earlier stages or when previously undetectable without increasing the radiation dose. The ability to improve the capability to diagnose disease without increasing the risk of harmful radiation to the patient would significantly improve the balance between the risks and benefits of cancer screening, which holds the potential to revolutionize the fields of x-ray imaging and lower mortality rates.

1 Introduction

1.1 Significance

Mammography is the most widely used diagnostic technique for breast cancer detection,[1] and clinical trials have proven its ability to decrease mortality rates.[1-17] Due to the widespread usage, as well as the potential for saving lives, mammography has received constant research focus since the development of dedicated mammography systems began in the 1950s.[18] Breast cancer is a progressive disease and small tumors generally indicate an early stage, the detection of which results in a more favorable prognosis, due to a history of more successful treatment.[19] Therefore, early detection has been a constant goal throughout the development of mammography. The technology has evolved over the past 60 years with a consistent focus on balancing the need for adequate image quality to allow early detection of breast cancer with minimizing patient dose to reduce the risk of harmful radiation. However, the physical formulation of the x-ray images, which relies solely on attenuation contrast, has remained the same throughout the years. Attenuation contrast is based on the principle that x-rays are absorbed in varying amounts according to the biological properties of structures within an object, which generate differences in contrast on the x-ray image.[20] For example, the difference in biological composition between bones and soft tissue produces very high contrast between them on an x-ray image. However, the extremely similar composition of normal and malignant breast tissue[20-22] results in very low contrast, which presents a significant challenge for cancer detection in the field of mammography. As a result, much higher

quality is required in mammography to highlight the differences between normal and malignant tissue with adequate contrast. Since conventional x-ray formation relies on attenuation alone, improving the image quality can be accomplished only a few ways: lowering the x-ray energy to increase the amount of radiation absorbed by the tissue,[20-21, 23] and utilizing an anti-scatter grid between the object and detector to reduce the image degradation caused by scattered x-rays.[20, 24] Both methods improve the signal-to-noise ratio, and thus the image quality, of the image; however, this is accomplished at the expense of an increased radiation dose to the patient. In fact, grids typically increase the dose by a factor of 3 or more.[24] Unfortunately, the significant challenge of providing adequate image quality for detection and diagnosis, while minimizing the radiation dose to the patient, has not been overcome as of yet.

However, an emerging technology called phase contrast imaging has the potential to improve this difficult balance between image quality and radiation dose. Phase contrast imaging is based on the definition of x-rays as electromagnetic waves, which therefore also experience phase changes when passing through objects, resulting in contrast produced by refraction effects as well as attenuation effects on the resultant image.[21, 25-30] The amount of refraction is also dependent on biological properties of the structures within an object, and contrast in the image is produced according to differences in phase shifts between structures. Theoretical comparisons for given types of tissue indicate that the refraction amounts are much larger than the attenuation amounts; [25, 31-33] thus the ability to form an x-ray image exhibiting both attenuation and refraction holds the potential to significantly improve the quality of

the image. Therefore, phase contrast imaging has received extensive research focus, and numerous studies have indicated the potential of the new technology to benefit the fields of radiography, especially mammography. First, the improvement in image quality has been consistently reported.[21-22, 26-28, 30-32, 34-36] The ability to maintain the image quality improvement with increasing object thickness has also been thoroughly investigated,[21, 26-28, 30-31, 35-36] which is of critical importance in mammography due to the thickness of the breast. In addition, the ability to decrease the radiation dose to the patient through removal of the grid has also been reported.[22, 26, 34] Finally, studies have indicated that the phase contrast effect decreases much more slowly than attenuation with increasing x-ray energy;[22-23, 25, 30, 37-38] thus, the use of phase contrast imaging could sustain the image quality improvements at higher x-ray energies than conventional imaging. Due to the increased penetrability and lower absorption of x-ray photons at higher energies,[20, 39] the patient dose could be further reduced by increasing the x-ray energy, which is the foundation of the research presented in this dissertation. The typical x-ray energies for diagnostic radiography range from 15 to 150 kilovolts (kV).[20] Due to the restrictions imposed by attenuation imaging detailed above, mammography currently operates on the lower end of the range. The topic of higher x-ray energies for reduced dose has been thoroughly investigated by other radiography fields, such as chest radiography, which generally operates between 120 and 150 kV.[40-43] A few studies have investigated the potential of increasing the x-ray energy for mammography using phase contrast imaging to 60,[27-28, 38, 44] 86,[37] or even 110 kV,[31, 45] and have received encouraging results. To the best of my knowledge, the

potential of utilizing x-ray energy ranges such as those in chest radiography for mammography has not been reported previously.

The focus of the research presented in this dissertation comprises a thorough investigation of the potential of applying higher x-ray energies to the field of mammography through the use of phase contrast imaging, which holds the potential not only to improve the image quality for earlier detection of disease, but also to reduce the risk of harmful radiation to the patient. In addition to the dose benefits of increasing the x-ray energy, the dissertation research also has the potential to overcome an existing challenge in phase contrast imaging involving the number of output quanta generated with the x-ray source, which will be discussed in more detail in the following chapters.

1.2 Organization of Dissertation

The organization of the dissertation is as follows. First, Chapter 2 presents a detailed description of the necessary methods required to perform the dissertation research, which are separated into four categories: image quality, statistical methods, phase contrast imaging, and radiation dose. The next four chapters encompass the preliminary studies accomplished to demonstrate a thorough understanding of the research methods, as well as to evaluate the feasibility of the research and corresponding motivation in the medical imaging field. First, Chapter 3 details the development and characterization of a low energy phase contrast imaging system prototype. Next, Chapter 4 presents a method for optimization of the modulation

transfer function (MTF) algorithm. A comprehensive error analysis of the photon fluence contribution to the detective quantum efficiency (DQE) is detailed in Chapter 5, and Chapter 6 describes an investigation on the effects of a technique known as x-ray beam hardening on the DQE and radiation dose. The next three chapters present the design and completion of the dissertation research. First, the development and preliminary feasibility investigation of a high energy phase contrast imaging system prototype is presented in Chapter 7. Next, an image quality comparison to high and low energy conventional imaging at similar entrance exposures is presented in Chapter 8, followed by a comprehensive image quality and dose comparison of high energy phase contrast imaging with low energy conventional imaging in Chapter 9. Finally, the summary and discussion of results and research direction for future studies are presented in Chapter 10.

2 Research Methods

The comprehensive image quality and performance evaluation of a high energy phase contrast x-ray imaging system requires the knowledge and application of numerous research methods. The following four sections will present in detail these topics, with each section including development of the supporting theories, application of the methods, and analysis and comparison of the results. First, a thorough understanding of image quality, including the concepts forming its foundation, the methods through which it is assessed and compared, and the ability to improve it in a variety of applications is the foundation of this research. Next, extensive knowledge of the theory and application of statistical analysis methods is essential for a comprehensive evaluation and comparison of image quality. The third concept involves the development and application of phase contrast imaging, which is an important area of knowledge for which comprehensive understanding is imperative to successful completion of this research. Finally, radiation dose is a critical concept in diagnostic imaging, due to the risk of harm to the patient with excessive exposure. Therefore, knowledge of the factors influencing the radiation dose and estimation of the dose in a research environment are key factors in achieving the goals of this research.

2.1 Image Quality

2.1.1 Contrast, Noise and Resolution

Three fundamental concepts combine to describe the quality of an image: contrast, noise and resolution. First, contrast is the difference in intensity values between

regions in an image.[20, 39] For example, an image with black on one half and white on the other exhibits very high contrast between the two areas, while an image divided by similar grey scale values would have much lower contrast. The contrast, therefore, defines the ability of the viewer to distinguish the different areas within an image, which is essential in images utilized for diagnosis where the different areas may represent diseased tissue.

Next, noise is the existence of pixel values that do not convey meaningful information about the objects within the image. Instead, noise introduces a random or stochastic component to the image, which has the effect of blurring or distorting the image. The presence of noise in an x-ray image can mostly be attributed to the Poisson distribution of x-ray photons, with additional noise introduced by the imaging and detection components.[20, 39] The Poisson distribution is expressed as follows:[20, 39, 46-47]

$$P(X = k) = e^{-q} \cdot \frac{q^k}{k!}, \tag{1}$$

which describes the probability of k photons per unit area when q is the mean number of photons. The definition of the Poisson distribution gives the following distribution properties:[46-47]

$$\begin{aligned} E(X) &= \mu(X) = q, \\ Var(X) &= \sigma^2(X) = q \end{aligned} \tag{2}$$

which indicates that the mean and the variance are equal. Thus, the standard deviation is equal to the square root of the mean. This is an important property in x-ray imaging, as the mean represents the number of photons and the standard deviation

represents the noise.[20, 39] Since the noise is directly related to the mean number of photons, the number of photons can be adjusted to influence the amount of noise in an image, which will be discussed further in the next section.

Resolution, which is also referred to as spatial resolution, describes the minimum distance between distinguishable objects in an image.[20, 39] The traditional example of spatial resolution is the capability of an imaging system to clearly depict two objects as they become smaller and closer together. Represented by very small resolution values, high resolution is exhibited by two distinct objects within the image. On the other hand, low resolution is evidenced by the objects appearing as one object in the image, which is represented by larger values. One can see the importance of adequate spatial resolution to image quality, especially in diagnostic imaging, as the ability to distinguish an area of disease from the surrounding healthy tissue is critical to detection.

2.1.2 Image Quality Concepts

Image quality is defined by the three foundation concepts discussed in the previous section: contrast, noise and resolution. Several principles of image quality that are based on these concepts will be presented in this section.

Signal-to-noise ratio

First, the signal-to-noise ratio (SNR) is a measurement utilized to quantify the noise corruption that has occurred in an image. It is defined as the ratio of the strength of the useful image information, which is referred to as the signal, to the noise in the

image.[20, 39] Improved image quality is achieved by increasing the signal strength and reducing the noise; therefore a larger SNR value corresponds to higher image quality. The signal strength is characterized by the mean number of x-ray photons, which was defined as q in the previous section. The noise was defined as the standard deviation within the image, which was equal to $\sqrt{q}$, due to the Poisson nature of x-ray photons. The two quantities can therefore be combined to determine the SNR as follows:[20, 39]

$$SNR = \frac{q}{\sqrt{q}} = \sqrt{q}. \quad (3)$$

As demonstrated in Eq. (3), the SNR of an image can be increased by increasing the number of photons utilized to form the image. However, increasing the number of photons also increases the amount of radiation absorbed by the patient, which results in a tradeoff between SNR and radiation dose.

Rose model

Another important image quality concept involves a criterion of acceptable image quality developed by Albert Rose, a pioneer in the field of image quality research. The Rose model was based on a two-year study facilitated by Richard Blackwell, in which 20 subjects performed thousands of perception tests regarding the ability to view a circle of varying sizes on a background of varying contrasts and noise levels. Blackwell developed a graphical relationship between the ability to distinguish an object within an image to the size and contrast of the object and the noise in the image.[48] Based on these results, Rose developed a theoretical model relating the observer's ability to distinguish an object within an image to the SNR of the image.[49-

[50] Rose's theory therefore combines the three foundation concepts of image quality to specify a minimum SNR for object perception within an image, which is defined as a value in the range from 5 to 7.[20, 39, 49-50] Medical imaging researchers and clinical technicians widely utilize the Rose model to define the acceptable image quality for new and established systems, as well as to estimate the size of the smallest distinguishable object within an image having a specified contrast and noise.

Point spread function, line spread function and edge spread function

An important concept for defining the spatial resolution of an x-ray imaging system involves the response of the system to a specific input. For example, the image obtained from a single point stimulus is called the point spread function (PSF), which is considered a detailed description of a system's spatial resolution.[20, 39] The x-ray imaging systems studied in this research are considered isotropic, in which the blurring effects are equal in all directions. In addition, if the system produces a constant response on the image regardless of the location of the stimulus, then the system is considered stationary,[46] and x-ray imaging systems can be considered as such for calculation purposes.[20]

Next, the response of an x-ray imaging system to a line stimulus is defined as the line spread function (LSF), which thoroughly describes the spatial resolution of a stationary, isotropic system.[20, 39] In addition, the LSF provides a simpler measurement, as the slit must only be aligned in one dimension with the focal spot, instead of both dimensions as the point stimulus.[20, 39] In addition, a cross section of

the image is utilized instead of the entire image. An example of the line spread function is given in Figure 1(a).[51]

Finally, the edge spread function (ESF) describes the response of an imaging system to an edge stimulus, which is simpler to obtain experimentally than either the LSF or PSF, as the only requirement is a sharp edge, rather than an extremely small hole or narrow line. In addition, the ESF is not as sensitive to physical imperfections, misalignment or scattered radiation.[52-53] A cross section of the image across the edge is also utilized to illustrate the ESF, an example of which is provided in Figure 1(b).[51]

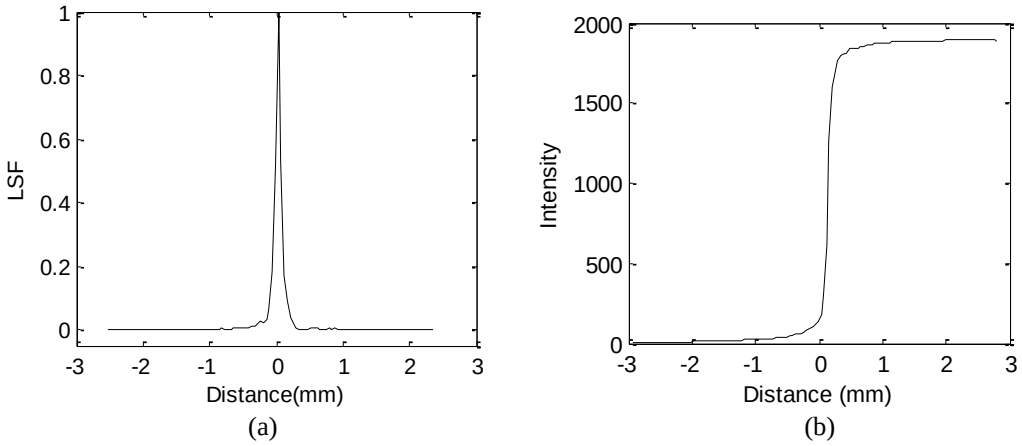

Figure 1: Illustration of the response of an imaging system to: (a) a line stimulus (LSF), and (b) an edge stimulus (ESF).

Modulation transfer function

Based on the response functions presented in the previous section, the modulation transfer function (MTF) provides a comprehensive description of the resolution properties of a system. This is accomplished through defining the modulation amount of input amplitudes as a function of the size of the object, which corresponds to spatial frequency.[20, 39] Utilizing the MTF, one can quantify the amount of object

contrast recorded on the image for an object of a specific size. Determining the ability of a system to acquire an image with acceptable contrast has established the MTF as a widely-accepted measurement of system performance, not only in research fields for evaluation of new systems, but also in clinical environments for verification of continued performance of established systems.

The MTF is calculated through normalizing the absolute value of the Fourier transform of the LSF.[54-56] The LSF can be determined directly through the use of a line stimulus[54-58] or through differentiation of the ESF.[20, 39] As detailed previously, the use of an edge is a simple and accurate method for determining the ESF, and numerous studies have verified the reliability and efficiency of the edge method in determination of the MTF.[51-53, 58-66] An example of an MTF calculated through the use of the edge method is given in Figure 2.[51]

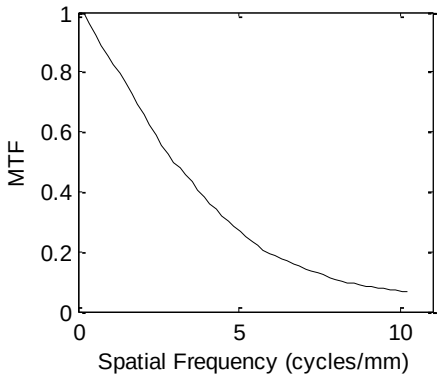

Figure 2: Modulation transfer function of an imaging system.

As expected, the curve demonstrates the ability of the imaging system to modulate low frequencies (ie, large objects) with very high percentages (expressed as fractions in Figure 2). The modulation ability decreases to 0 as the objects become smaller than

the sampling frequency of the system. This is also known as the Nyquist frequency, which is determined from the pixel pitch (Δx), or sampling rate, of the detector as follows:[20, 39, 67]

$$f_{Nyquist} = \frac{1}{\Delta x / 2}(cycles / mm). \quad (4)$$

Noise power spectrum

The noise power spectrum (NPS) is an established determination of the noise processed by a system.[68-73] The NPS, which is also denoted the Wiener spectra or power spectral density (PSD), demonstrates the level of noise in the image as a function of spatial frequency.[20, 39] Similar to the amplitude modulation capabilities of an imaging system illustrated in Figure 2, the ability of the system to modulate noise also decreases as the spatial frequency decreases.

The NPS is determined by calculating the Fourier transform of the autocorrelation function (ACF).[39, 46] The ACF is a measurement of similarity within a data set, and is thus a mathematical tool for locating repeating patterns, such as the presence of periodic signals within the data. The ACF is determined through the following formula:[39, 46]

$$C(\Delta_x, \Delta_y) = E\left\{ I(x, y) I(x + \Delta_x, y + \Delta_y) \right\}, \quad (5)$$

where E denotes the expected value function, which operates on the image I, averaging the correlation between each point $I(x, y)$ and $I(x+\Delta_x, y+\Delta_y)$ in the image. The autocorrelation function for an x-ray imaging system provides the measurement

of spatial resolution when the input is uniform noise, which is produced through acquiring an image without an object in the path of the x-ray beam[20, 39] and referred to as the noise-only image.

Due to the stochastic nature of noise in x-ray images, the experimental calculation of the two-dimensional NPS typically involves separating the noise-only image into numerous smaller regions and averaging the NPS values calculated from each region.[68-70, 72-74] The central portion of the image is utilized to eliminate the non-uniformities that typically occur near the edges.[68] The region size is determined through balancing a tradeoff between smaller variance with smaller regions and finer frequency resolution with larger regions.[68, 72] In addition, the size of the regions have traditionally been selected as a power of two to facilitate efficient Fourier transform computations. The NPS calculations for each region will be performed utilizing the following formula:[68, 72-73]

$$NPS(u,v) = \frac{\Delta x \cdot \Delta x}{N_x \cdot N_y} \left\langle \left| FT(u,v) \right|^2 \right\rangle, \tag{6}$$

where Δx is the pixel pitch of the detector, N_x and N_y are the number of pixels represented by the smaller regions and $\left\langle \left| FT(u,v) \right|^2 \right\rangle$ is the ensemble average of the squares of the Fourier transforms of the smaller regions. In this way, the regions can be averaged to determine a NPS for each image, and then the overall two-dimensional NPS is determined through averaging the individual NPS results.

The one-dimensional NPS is also of research interest, not only to present a clear illustration of the spatial frequency in a single dimension, but also for calculation of additional image quality measurements such as the DQE, which will be discussed in a later section. Numerous studies have investigated methods for calculation of the one-dimensional NPS from the two-dimensional NPS.[68-70, 73, 75-76] The method that was utilized in the dissertation research involves the use of a slice consisting of four data lines parallel to and immediately adjacent to the axes of the two-dimensional NPS.[68, 73] For each coordinate *(u, v)* in the slice, the corresponding one-dimensional value is calculated as follows:

$$NPS(f) = \sqrt{u^2 + v^2}. \tag{7}$$

2.1.3 Subjective Measurements

Subjective comparison methods involve the use of human observers to identify distinguishable objects within images to provide a qualitative description of the image quality. The test tools utilized to produce the desired objects on x-ray images are referred to as phantoms. Numerous different types of phantoms are used extensively throughout clinical and investigational medical imaging. Typically an observer study includes evaluation of the images by numerous clinicians or researchers, and the mean results are utilized to provide a simple and accurate comparison between two imaging systems or techniques. Numerous subjective comparison methods exist, and a few of the methods that have been extensively utilized due to accuracy and efficiency will be presented in this section.

Contrast-Detail Analysis

Contrast-detail analysis is a subjective comparison method based upon the theory of the Rose model, which utilizes similar methods to the early Blackwell studies detailed previously. Contrast-detail analysis has been widely-accepted as a simple and effective method for comparison of medical imaging systems.[44, 77-81] Contrast-detail phantoms typically consist of a matrix of circles with varying diameters along one axis to represent object size, and varying thicknesses along the other axis to produce contrast within the image.[20, 39] An example of a contrast-detail phantom and a corresponding x-ray image are provided in Figure 3.

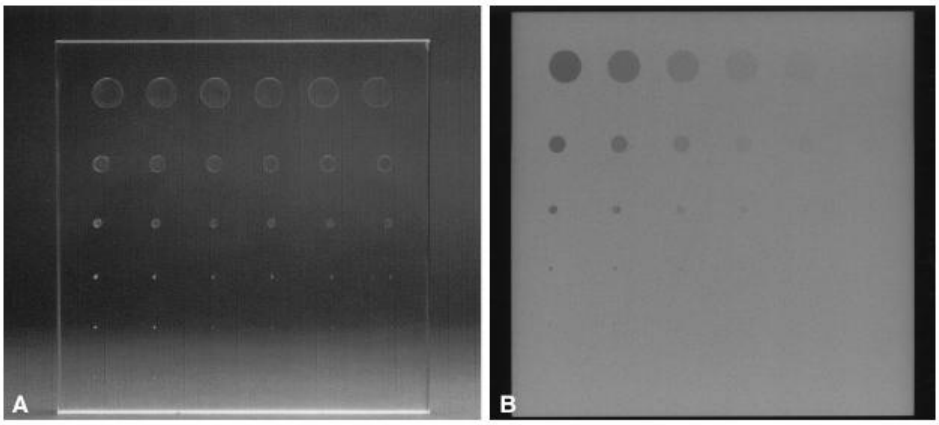

Figure 3: Contrast-detail phantom (A) and corresponding x-ray image (B).

The analysis involves an observer identifying the minimum perceptible contrast (ie, object thickness) in the image for each object size. Results from numerous observers are averaged, and the result is compiled into a contrast-detail curve, in which size is represented on the x-axis and contrast or thickness is represented on the y-axis. The curve therefore indicates the contrast required to distinguish an object as a function of the object size. A typical curve begins in the upper left corner, indicating large

contrast values required for small diameters, and decreases to the lower right corner, exemplifying smaller contrast values needed for large objects. Thus the curve illustrates the resolving power of the system, and curves for different systems or techniques can easily be compared. A system exhibiting higher performance produces a contrast-detail curve located closer to the x-y axis. Improved spatial resolution is indicated by the curve being closer to the y-axis, which demonstrates the ability to distinguish a smaller object at the same contrast level. Similarly, improved contrast resolution is exemplified through the ability to distinguish an object of the same size at a smaller contrast level, which is indicated through the curve being closer to the x-axis.[20, 39, 82]

CDMAM

The disadvantage of conventional contrast-detail analysis involves the known placement of the objects, which can compromise the results due to observer bias.[83-86] Thus, one can see the motivation for utilizing a different type of contrast-detail phantom known as the CDMAM phantom, which is shown in Figure 4.[87] The CDMAM phantom eliminates the known location bias through the use of semi-randomized object placement. As illustrated in the figure, each matrix location not only contains an object in the center, as in standard contrast-detail phantoms, but also a second object randomly located in one of the corners. The observer must successfully indicate the location of the corner object in the analysis, thus employing a four-alternative fixed-choice method, which has been proven to significantly improve the accuracy of the contrast-detail analysis.[77, 88-89] An x-ray system or

technique is evaluated by the CDMAM comparison method based on a procedure detailed by the manufacturer.[90] After acquisition of the comparison CDMAM images, they are randomly presented to a group of independent observers for analysis. The observers score each of the images by indicating the location of the corner object for each square in which the object is distinguishable. The results are then graded for determination of the accuracy of the observer responses, through comparing the locations indicated by each observer to the true locations of the randomly placed cylinders. A correction scheme must then be applied to reduce the error introduced through random guesses. The scheme is based on two rules: every true indication must have two correctly identified adjacent squares to be considered true, and a false with three correctly identified adjacent squares is considered true. After application of the scheme, the observer results are averaged and a contrast-detail curve is generated for each of the comparison images. The curves illustrate the smallest correctly-identified gold thickness for each diameter represented in the phantom. Statistical comparison methods are then applied to each set of comparison curves to determine if the image quality differences between the images are statistically significant. This is accomplished through constructing a Student *t* confidence interval around each point, which will be detailed in Section 2.2.1.

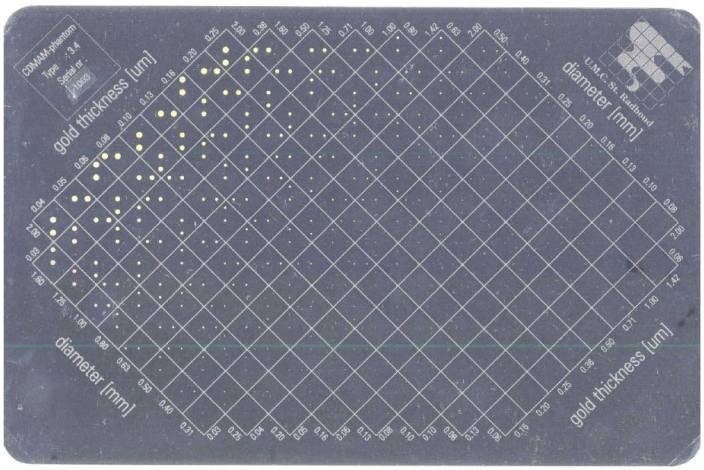

Figure 4: Photograph of the CDMAM Phantom. Each matrix square for a specific thickness and diameter consists not only of an object in the center of the square, as in standard contrast-detail phantoms, but also an object in one of the corners selected at random.

ACR

The American College of Radiology (ACR) phantom provides a standard mammographic quality control evaluation of image quality,[91-92] which is utilized extensively in both clinical and research environments[21, 34, 36, 38, 81, 93-94] for reliable image quality comparisons. The phantom provides comprehensive evaluation from a mammography perspective by containing three separate types of objects, each providing the ability to test system performance based on a specific clinical detection purpose. The objects include specks simulating calcifications, fibers representing fibrous calcifications within tissue ducts, and masses imitating tumors or tissue masses.[92] Calcifications are tiny calcium deposits within the breast tissue, which are known as a frequent indication of breast cancer.[95-98] The phantom includes several objects of each type ranging in size, from objects that should be visible on any imaging system to those that will be difficult to discern on even the highest performing systems. The Nuclear Associates Model 18-220 ACR phantom

configuration, which was utilized in the dissertation research, is illustrated in Figure 5.[92]

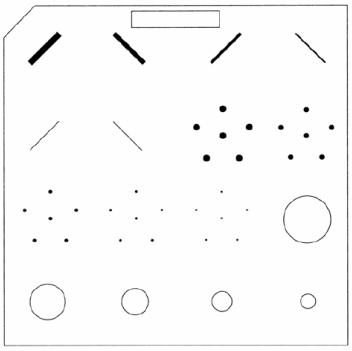

Figure 5: Illustration of the test objects represented in the Nuclear Associates ACR phantom 18-220, which includes groups of fibers, specks and masses.

An x-ray system or technique is evaluated by the ACR comparison method based on the mammography quality control specifications,[91] which involve the number of objects of each type that are distinguishable on an x-ray image. For example, one point is awarded for each fiber that is completely visible on the image, while 0.5 points are given if more than half of the fiber is evident. Specks contribute a full point for four or more visible specks, and half a point if two or three specks are noticeable. Finally, masses receive half a point for illustrating a density difference in contrast to the background, and a full point if the difference has a generally circular shape. Separate scores are determined through this method for each of the groups, and the scores are added together to achieve the total ACR score.

An ACR observer study consists of numerous observers identifying the objects within the images. The means of the observers' scores are utilized to determine individual group scores as well as overall scores for each system or technique. Two systems or

techniques are easily compared by determining the higher ACR score, which correlates to improved image quality performance. In addition, the individual groups can be compared separately to determine the system that delivers superior performance for each type of mammography test object.

2.1.4 Objective Measurements

Objective comparison methods consist of mathematical calculations performed on the imaging data, which provide quantitative descriptions of the image quality and allow for impartial comparison between two imaging systems. The MTF and NPS, which were discussed in Section 2.1.2, provide measurements of an imaging system that can be compared objectively for determination of superior signal and noise modulation, respectively, provided by the imaging system. A comprehensive quantitative determination of the image quality provided by an imaging system is the detective quantum efficiency (DQE),[20, 39, 99] which will be presented in detail in the following section.

Detective quantum efficiency (DQE)

The detective quantum efficiency (DQE) describes the overall SNR of the system output given the SNR of the input:[20, 39, 100]

$$DQE(f) = \frac{SNR_{OUT}^2}{SNR_{IN}^2}. \tag{8}$$

The formula can be expressed in terms of quantities from the previous sections through the following derivation. First, the input SNR can be determined through the

use of Eq. (3), which describes the SNR in terms of the mean number of input x-ray photons q:

$$SNR^2_{IN} = (\sqrt{q})^2 = q. \tag{9}$$

Next, the output SNR calculation is based on the mean output signal $S_{OUT}(f)$ and the mean output noise $N_{OUT}(f)$:

$$SNR^2_{OUT} = \frac{S^2_{OUT}(f)}{N^2_{OUT}(f)}. \tag{10}$$

As detailed in Section 2.1.2, the output signal and noise quantities are described by the MTF and NPS, respectively. Both quantities can be represented as the product of their zero frequency value, or normalization factor, and their normalized form, as follows:[100-101]

$$SNR^2_{OUT} = \frac{S^2_{OUT}(0) \cdot MTF^2(f)}{N^2_{OUT}(0) \cdot NPS(f)}. \tag{11}$$

Recalling the definition of the NPS, the represented quantity is already squared and therefore does not require the additional step. Eq. (11) can be further simplified through substitution of Eq. (10) for a value of $f = 0$:[100-101]

$$SNR^2_{OUT} = SNR^2_{OUT}(0) \cdot \frac{MTF^2(f)}{NPS(f)} = NEQ(f), \tag{12}$$

where $SNR^2_{OUT}(0)$ is the large area signal, which represents the average intensity of an output image pixel, assuming a uniform x-ray beam absorbed by the detector. Also referred to as $S(0)$, the large area signal is calculated experimentally by determining the mean pixel value from a noise-only image.[68, 73, 75, 102-103] The noise equivalent quanta (NEQ) is a combination of the MTF, NPS and $S(0)$ describing the number of

quanta recorded at each spatial frequency, which provides information regarding the maximum attainable value of the output SNR.[63, 68, 70, 104-105] Combining the equations for input and output SNR from Eqs. (9) and (12) provides the calculation of the DQE through the following equation:[68, 73, 75, 100-102]

$$DQE(f) = \frac{S(0)^2 \cdot MTF(f)^2}{NPS(f) \cdot q} = \frac{NEQ(f)}{q}. \quad (13)$$

As detailed previously, the photon fluence (q) represents the square of the ideal SNR of the incident x-ray beam, as characterized by the Poisson distribution of x-ray photons.[20, 39] The value of q is determined experimentally by calculating the number of incident photons per square millimeter, which is accomplished through multiplying the radiation exposure by the photon fluence per unit exposure determined from the x-ray spectrum.[73, 103, 106-107] The radiation exposure is measured through the use of a calibrated ionization chamber placed directly in the center of the x-ray beam, in the absence of additional measurement or acquisition devices to eliminate errors caused by x-ray backscatter. The x-ray spectrum is measured through the use of an x-ray spectrometer, which is placed directly in the center of the path of the x-ray beam preceded by a pair of tungsten collimators. Spectral measurements typically utilize collimation to limit the incident photon fluence to an acceptable level for the small surface area of the spectrometer detector.[108-110] An example of the DQE is provided in Figure 6.[103] Due to the combination of the image quality foundation concepts of noise, contrast and resolution, the DQE is considered a standard image quality determination method[20, 39, 71, 99-100] and is therefore widely used in both clinical and research environments.

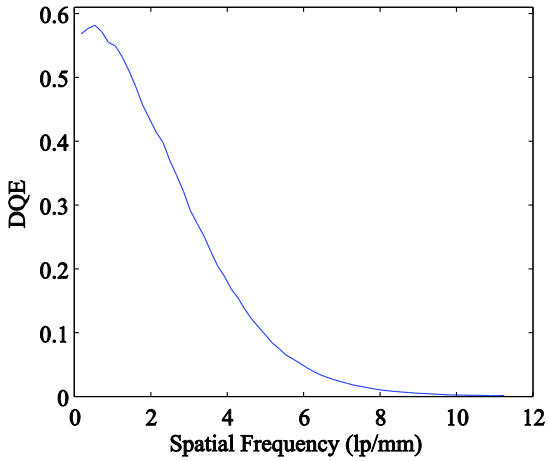

Figure 6: Detective quantum efficiency (DQE) calculated for an imaging system.

2.1.5 Clinical Measurements

Clinical measurement methods facilitate the comparison of image quality performance on images directly pertaining to clinical applications. These methods provide a direct qualitative indication of the performance of the imaging system for disease detection and diagnosis purposes, which is the motivation of medical imaging research. In addition to image quality measurements, clinical methods also provide more accurate dose measurement capabilities.[111] Therefore, these methods are an extremely valuable research tool for evaluation of imaging system performance. In ideal circumstances, clinical measurements include the comparison of actual clinical images, such as human breast tissue acquired from biopsy and lumpectomy procedures in a medical facility.[22, 35-36, 112] However, due to the difficulty of utilizing human tissue in a research environment, numerous research studies have investigated the use of tissue-equivalent phantoms, which consist of materials that simulate human tissue on an x-ray image. The phantom composition includes BR12, which is a

homogeneous material simulating a tissue composition of 50% glandular tissue and 50% adipose tissue,[29, 113-116] polymethyl methacrylate (PMMA),[117-118] commercially fabricated phantoms of various thicknesses and glandular compositions,[119-120] and custom-fabricated phantoms.[35, 112, 121] In addition, numerous studies have utilized tissues of animals to simulate human tissue, such as lamb liver specimens,[27] small aquarium fish,[28] and raw chicken breast specimens.[36]

Another technique in clinical comparisons involves the use of additional materials to simulate the presence of disease within the body. For example, calcifications can be simulated through the addition of crushed calcium tablets to tissue-equivalent specimens, as the relative ability to distinguish calcifications on a clinical image is of critical importance in the comparison.

A new tissue-equivalent phantom has recently been developed that not only provides qualitative analysis, but also incorporates the quantitative comparison method of ACR.[122] This phantom therefore combines objective and subjective comparison methods, resulting in a comprehensive image quality comparison with a single phantom. Due to this considerable benefit, Chapters 7 through 9 will present comparisons utilizing this phantom. To the best of my knowledge, previous research studies utilizing this phantom have not been presented previously.

2.2 Statistical Analysis

The application of statistical analysis is an essential step in commercial and research environments in numerous areas of concentration. Statistics provides a quantitative comparison of values and methods to determine the significance, if any, of differences between them. In addition, the ability to identify and quantify the error contributed through calculation and measurement of any value provides insight into potentially reducing the error amount. For both of these reasons, which will be presented in detail in this section, statistical analysis is a central focus of the research proposed in this paper.

2.2.1 Statistical Comparison Methods

The application of quantitative comparison methods requires detailed statistical analysis for accurate determination of the amount of image quality difference, if any, between the systems or techniques in comparison. In selecting appropriate statistical methods to apply in research studies, two main factors must be taken into consideration: sample size and existence of a known variance.[46-47, 123] First, while sample sizes that are typically employed in research studies appear to be large to the research group conducting the study, they are actually relatively small from a statistical standpoint, as small sample consideration is typically applied to data sets with less than twenty[46] or thirty samples.[123] Secondly, statistical comparison methods such as the normal distribution[46-47, 123] rely on the assumption that the true variance among the data is a known value. However, this is not a valid assumption in an experimental setting, and the calculations must be adjusted appropriately. For both of

these reasons, the Student *t* distribution is frequently utilized in research environments for analyzing collected data, due to its proven ability to construct accurate confidence intervals on smaller data sets with unknown variance.[46-47, 123]

The application of a Student *t* distribution to a data set is accomplished through the following steps. First, an estimator for the sample variance is calculated with the following formula:[46-47, 123]

$$S = \sqrt{\frac{1}{n-1}\sum_{i=1}^{n}(Y_i - \bar{Y})^2}, \tag{14}$$

where n is the sample size, Y_i represents the data value measured for sample i, and $\bar{Y}$ is the mean value calculated from all of the data values. This estimator is known as the *S*-value, and represents the unbiased version of the maximum likelihood estimator for the variance.[46-47, 123]

Next, a Student *t* confidence interval is constructed around each data point for the purpose of determining the variance among the data values measured for that point. A 95% confidence interval is typically utilized,[46-47, 123] and the number of degrees of freedom is represented by $n - 1$. The corresponding confidence interval is calculated as follows:[46-47, 123]

$$\bar{Y} \pm t_{\frac{\alpha}{2}, n-1} \cdot \frac{S}{\sqrt{n}}, \tag{15}$$

where n is the number of samples, $\bar{Y}$ is the mean value, S is the value calculated with Eq. (14), and $t_{\frac{\alpha}{2},n-1}$ is the Student t value corresponding to the selected confidence interval with $n - 1$ degrees of freedom. The confidence intervals represent the variance among the measured data, and can be utilized for comparison purposes between two samples. For example, confidence intervals can be constructed for contrast-detail curves and ACR scores resulting from observer studies, or for MTF, NPS and DQE curves calculated from numerous images. Then the confidence intervals for two imaging systems or techniques can be compared to determine if one system or technique provides superior performance by a statistically significant amount.

2.2.2 Error Analysis in Measurements and Calculations

The total amount of error in a measurement is defined as a combination of two types of error: random error and systematic error.[124] Random error, denoted as ε, refers to statistical fluctuation, or differences in repeated measurements of the same value, and is estimated by the variance within the measured values. Systematic error (β) is a measurement of accuracy, or the difference between the measured value and the true value. Since the true value is not typically known, the systematic error must be estimated. This is accomplished through analysis of the significant sources of systematic error, such as the accuracy of the measuring devices and data processing algorithms. Assuming the random and systematic error components to be independent, the total variance according to both types of error can be calculated as follows:[124]

$$\sigma_i^2 = \sigma_\varepsilon^2 + \sigma_\beta^2. \quad (16)$$

The propagation of the error from each factor in a measurement contributes to the overall error in the result, which is represented by the data reduction equation:[124-125]

$$r = r(x_1, x_2, x_3, ..., x_n), \quad (17)$$

where r is the final result of the measurement, and the x_i values correspond to each of the measurements contributing to the overall calculation. The mean and variance of r can be estimated according to the individual measurements as follows:[47, 124-125]

$$\mu_r = r(\mu_1, \mu_2, \mu_3, ..., \mu_n) \quad (18)$$

and

$$\sigma_r^2 = \sum_{i=1}^{n} \sigma_i^2 \left(\frac{\partial r}{\partial x_i} \right)^2, \quad (19)$$

where μ_i is the mean and σ_i^2 is the total variance of each individual measurement x_i, and $\left(\frac{\partial r}{\partial x_i} \right)$ is known as the sensitivity coefficient, which determines the influence of each factor on the total error in the result. The use of the mean value of each measurement for the calculation of r minimizes the random error, and determining the factors resulting in the largest contribution to the total variance provide insight for reducing the overall error in the result. In order to facilitate direct comparisons of the error introduced by the individual measurements or calculations, the relative error for each can be determined by calculating the coefficient of variation.[20, 126] This is necessary for comparison purposes, due to the fact that the variance is dependent on the magnitude of the value it describes. The relative error is calculated as follows:[126]

$$S_i = \frac{\sigma_i}{\mu_i}. \tag{20}$$

2.3 Phase Contrast Imaging

2.3.1 Theory

X-ray scattering in tissue corresponds to the index of refraction of the tissue, which is a complex quantity that can be represented mathematically as follows:[25, 29, 31-33]

$$n = 1 - \delta + i\beta. \tag{21}$$

In Eq. (21), δ is the real portion of the index, representing the refractive index decrement which accounts for the x-ray phase shift, and β is the imaginary part, which is responsible for the x-ray attenuation. The parameters δ and β are defined by the following formulas:[32]

$$\delta = \left(\frac{r_e \cdot \lambda^2}{2\pi} \right) \sum_l N_l \left(Z_l + f_l^r \right) \tag{22}$$

and

$$\beta = \left(\frac{r_e \cdot \lambda^2}{2\pi} \right) \sum_l \left(N_l \cdot f_l^i \right), \tag{23}$$

where λ represents the wavelength of the x-rays, r_e is the classic electron radius, and the remaining properties apply to element l in the object: Z_l is the atomic number, N_l represents the atomic density, f_l^r is the real part of the anomalous scattering factor,

and f_l^i is the imaginary part. The *z*-projection of the corresponding phase change, which is denoted $\Phi(x, y)$, and the linear attenuation coefficient $\mu(x, y)$ that are experienced by the x-ray are represented by the following equations:[33]

$$\Phi(x,y) = \frac{-2\pi}{\lambda} \int \delta(x,y,z)dz \tag{24}$$

and

$$\mu(x,y) = \frac{4\pi}{\lambda} \int \beta(x,y,z)dz, \tag{25}$$

for a z-propagating incident plane wave. With these equations, calculations can be made to determine relative values for Φ and μ for specific elements by utilizing each element's atomic number, density, calculated anomalous scattering factors,[127] and linear attenuation coefficients.[128] Application of these theoretical calculations illustrates that the difference in x-ray phase shifts can be up to 1000 times greater than the difference in linear attenuation coefficients for a given type of tissue.[25, 31-33] Thus the technology of phase contrast imaging holds the potential to significantly improve the field of mammography, due to the ability to formulate images based on phase shifts as well as attenuation differences.

2.3.2 Background

As a result of the extensive research attention, three types of phase contrast imaging have surfaced: diffraction-enhanced imaging (DEI), x-ray interferometry, and in-line

phase contrast imaging.[25] DEI[22, 25, 129-131] and interferometry[25, 32, 132] both rely on monochromatic sources and complicated system configurations involving perfect crystals, which have been significant challenges in proving the feasibility of clinical implementation. On the other hand, in-line phase contrast imaging utilizes polychromatic x-rays from a microfocus source, both of which are readily available and clinically acceptable.[27-29] First, the conventional use of polychromatic radiation is feasible with in-line phase contrast imaging because the intensity of the refractive differences is independent of wavelength.[27-28] Next, the phase contrast effect requires high spatial coherence to produce the optimal image quality improvement.[28-29] This can be facilitated through a large source to object distance, although this presents a challenge in clinical implementation. However, high spatial coherence can also be attained through the use of an x-ray source with an extremely small focal spot size, which is known as a microfocus source.[28-29] Another benefit of in-line phase contrast imaging in regards to clinical feasibility is that it utilizes a very similar configuration to conventional x-ray imaging, with the exception of an air gap between the object and the detector. Both configurations are illustrated for comparison purposes in Figure 7.

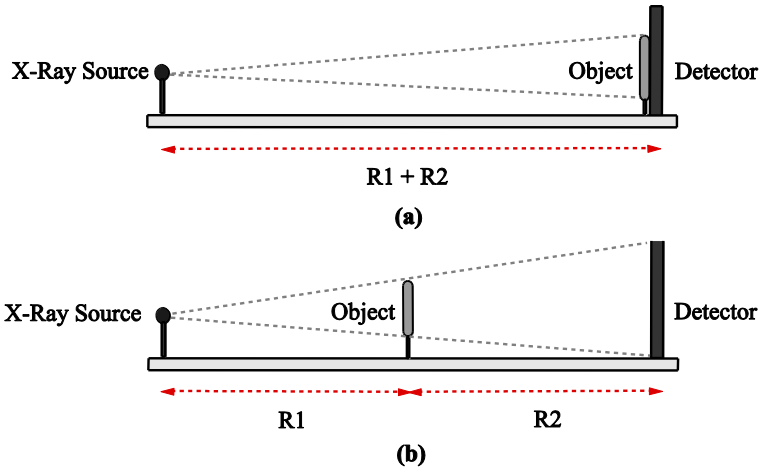

Figure 7: Illustration of the x-ray configurations for (a) conventional imaging and (b) phase contrast imaging.

The air gap in phase contrast imaging produces the phase contrast effect through the propagation of the x-rays after refraction within the object. This distance allows the phase gradients produced by differences in refraction amounts within the object to be superimposed on the intensity variations produced by the attenuation differences.[21, 25] The result is an x-ray image comprised of both attenuation and phase contrast effects, demonstrating significantly enhanced visibility on the boundaries between materials. These areas typically experience attenuation effects as well, and the combination results in pronounced edge enhancement between areas of different properties within the image.[21, 23, 25-26, 31, 38]

2.3.3 Potential Advantages

Numerous studies have investigated the benefits provided by phase contrast imaging in comparison to conventional x-ray imaging. First, the improvement in image quality has been widely reported.[21-22, 26-28, 30-31, 34-36, 38] The enhanced image quality can be

attributed to a combination of several factors. First, as detailed previously, the edge enhancement effect occurs as a result of the superimposition of attenuation and refraction effects on the resultant image. This combination improves the contrast of the image, most notably in areas where both refraction and attenuation effects are produced, such as boundaries between materials with different properties. Thus the edge effect has the potential to benefit mammography, due to the slightly different properties between normal and malignant breast tissue that are difficult to distinguish based only on attenuation.

The image quality enhancement in phase contrast imaging can also be attributed to the magnification introduced by the air gap as a result of similar triangle geometry, which is represented by the following formula:[20, 39]

$$M = \frac{R1 + R2}{R1}, \tag{26}$$

where *R1* is the source-to-object distance and *R2* is the object-to-detector distance, which are both represented in Figure 7. Magnification increases the sampling rate and thus the Nyquist frequency, which results in improved spatial resolution.[20, 39] The magnification could potentially result in image blurring if the focal spot is not sufficiently small to minimize the penumbra effect, which is also known as geometric unsharpness and is caused by the finite focal spot size.[20, 39] However, the magnification introduced by the use of a microfocus source combines with the edge enhancement in phase contrast imaging to counteract the unsharpness and enhance the quality of the image.[26, 34] The amount of phase contrast effect corresponds to the

amount of magnification, which is controlled by the distances of *R1* and *R2*. Selection of the magnification factor is therefore a critical step in designing a phase contrast system, as it represents a tradeoff between optimal phase contrast effect and image quality. The magnification factor must be large enough for the phase contrast effect to provide a noticeable improvement to the image quality. As illustrated in Figure 7, the conventional configuration consists of the object placed in contact with the detector, which results in a magnification factor of 1 and does not produce any phase contrast effect on the image. On the other hand, if the magnification factor is too large, the spatial coherence can no longer be maintained and the phase contrast effect spreads across the entire image instead of only enhancing the edges.[21, 34] Recent studies investigating the selection of these values to optimize the phase contrast effect while maintaining the spatial coherence have indicated this can be achieved with a magnification factor of around 2.[29, 31, 34, 38, 45]

Another benefit of phase contrast imaging in comparison to attenuation imaging concerns the ability to maintain the image quality improvement with increasing object thickness, which is of critical importance in mammography due to the thickness of the breast. Under compression, an average breast thickness of 4.5 centimeters is assumed by the Institute of Physical Sciences in Medicine (IPSM) for the standard patient,[133] which renders disease detection within breast x-ray images a difficult task. However, compressed breasts of patients with larger than average breasts can be much thicker, which presents an even more difficult challenge in conventional mammography. Studies comparing the image quality delivered by phase contrast imaging in

comparison to conventional imaging have demonstrated that the phase contrast effect does not decrease with object thickness as quickly as the absorption effect.[21, 26-28, 30-31, 35-36, 94]

The use of the air gap also provides an image quality improvement, as it increases the distance that scattered photons must travel after interaction, which changes the photon trajectory and thus reduces the amount reaching the detector. This is known as scatter rejection, which directly improves the SNR in the image due to the fact that the scattered photons contribute only to the noise.[20, 39] The resultant image quality improvement is comparable to that provided by the grid typically used in conventional imaging.[22, 26, 34] Thus the grid could potentially be removed, thereby reducing the patient dose without negatively affecting the image quality.

Next, the benefit upon which this research is based is the ability to increase the x-ray energy through the use of phase contrast imaging. This can be attributed to the principle that phase contrast imaging does not rely solely on attenuation. Theoretical calculations relating the parameters from Eq. (21) to x-ray energy (E) indicate that the attenuation factor β is proportional to E^{-4}, while the x-ray phase shift factor δ is proportional to E^{-2}, which demonstrates that the phase contrast effect decreases more slowly than the absorption amount with increasing x-ray energy.[25] Studies have validated these theoretical calculations with experimental results indicating that the image quality provided by the phase contrast effect does not decrease with an increase in x-ray energy, in contrast to the quality provided by attenuation alone.[22-23, 25, 30, 37-38] The use of phase contrast imaging could therefore sustain the image quality

improvements at higher x-ray energies than conventional imaging. Due to the increased penetrability and lower absorption of x-ray photons at higher energies,[20, 39] the patient dose can be further reduced by increasing the x-ray energy.

In addition to the dose benefits of increasing the x-ray energy, the dissertation research also has the potential to overcome an existing challenge in phase contrast imaging involving the number of output quanta generated with the microfocus source. The number of quanta *N* generated is represented as follows:[20]

$$N \propto kV^2 \cdot mAs\ , \tag{27}$$

where *kV* represents the x-ray energy and *mAs* indicates a quantity representing the tube current in units of milliamperes (mA) multiplied by the exposure time in units of seconds (s). A microfocus source produces a limited tube current as compared to conventional sources, due to the smaller focal spot size. For the same x-ray energy and exposure time, a reduction in tube current reduces the x-ray quanta output proportionately. Therefore, the exposure time must be increased when utilizing the same x-ray energy, in order to balance the reduced number of x-ray quanta.[22, 28, 31] For example, consider a conventional x-ray source with tube current of 100 mA and a microfocus x-ray source with a tube current of 4 mA, both operating at 25 kV. The reduction in tube current by a factor of 25 increases the exposure time from the standard clinical time of 1 second to 25 seconds, which hinders the clinical feasibility due to the requirement of patients to hold their breath during exposure. However, increasing the x-ray energy instead of the exposure time requires only an increase by a factor of 5 from 25 kV to 125 kV, which is clinically feasible. Therefore, phase

contrast imaging at high energies holds the potential to produce the same number of x-ray quanta at clinical exposure times, which is an indication of the clinical feasibility and corresponding ability to benefit the field of mammography by reducing the dose without negatively affecting the detection capability.

2.4 Radiation Dose

2.4.1 Introduction

As mentioned repeatedly in the previous sections, there have been two primary research goals throughout the history of mammography: decrease the risk of harm to the patient by reducing the radiation dose, and increase the image quality to improve the ability to detect and diagnose diseases. Unfortunately, many methods developed to reduce the radiation dose result in decreased image quality, while methods designed to improve the image quality also increase the radiation dose. As a result, continuous research attention has been focused on the challenge of balancing this tradeoff between image quality and radiation dose. The research efforts have produced numerous technological advancements that have improved the tradeoff, not only through increased image quality but also with reduced radiation dose.[1, 18, 24, 111] Nevertheless, many studies have challenged the risk versus benefit tradeoff of breast screening.[134-136] However, the American Cancer Society (ACS) continues to recommend routine breast screenings as an important part of breast cancer prevention.[137] The ACS recommendation is based primarily on the results of numerous randomized controlled trials demonstrating the success of mammography in reducing the breast cancer mortality rate.[2-17] The proven ability to save lives has

therefore established mammography as the most widely used diagnostic technique for detecting breast cancer.[1] In order to continue to prevail over the risk versus benefit skepticism, as well as compete with other technologies threatening to replace mammography, the challenge remains to further improve the tradeoff between image quality and radiation dose, which is the primary goal of the research presented in this paper.

2.4.2 Calculation

In the early years of mammography, measurement of the entrance exposure to the breast was typically utilized to estimate the radiation risk to the patient.[111] However, measurement of the exposure at the surface of the breast does not provide the necessary information, which is the amount of radiation absorbed within the body. A comprehensive measurement is therefore necessary to provide a more accurate estimation of the patient dose. First, it is important to note that breast tissue composition is typically separated into two categories: glandular and adipose. Glandular refers to the tissue bearing glands, while adipose refers to the tissue constituted mostly of fat cells. Breast cancer typically arises in the glandular tissue,[20, 138] thus the dose to the glandular tissue is the quantity of interest in evaluating the risks of mammography. The average glandular dose has therefore been established as the standard measurement of radiation dose in mammography, and guidelines have been created by numerous national and international councils for its calculation and supervision in clinical environments.[133, 138-142] The formula for calculation of the average glandular dose D_g is as follows:

$$D_g = D_{gN} \cdot X_{ESE}\,, \tag{28}$$

where D_{gN} is the normalized average glandular dose coefficient and X_{ESE} is the object entrance exposure, or entrance skin exposure (ESE). D_{gN} is a conversion factor between entrance skin exposure and average glandular dose, and is determined by experimental and computer simulation methods based on the following factors: radiation quality (x-ray energy or half value layer), x-ray tube target material, filter material, breast thickness and breast tissue composition,[20] all of which will be detailed in the following section. X_{ESE} is typically calculated as the average of numerous exposure measurements at the surface of the object, which is measured by placing the ion chamber in the path of the x-ray beam in precisely the same location at which the object is placed during the imaging process, in the absence of any other imaging or measurement components to reduce the risk of x-ray backscatter.

2.4.3 D_{gN} Factors

As mentioned previously, mammography typically operates at the lower end of the diagnostic x-ray energy range, with energies between 20 and 35 kV. The x-ray tubes utilized in mammography were designed specifically for these low energy values, by employing target and filter materials with very low characteristic peak values. The most common x-ray tube target materials are Molybdenum (Mo) and Rhodium (Rh), although Tungsten (W) has recently become more common.[1, 20, 24] The most common clinical filter materials are also Mo and Rh. The breast thickness and composition are typically based on the definition of a “standard breast”, which is used for dose estimation purposes due to the impracticality of physically measuring the precise

thickness and breast composition for each patient individually. The standard compressed breast thickness is 4.5 cm, and the tissue composition is 50% adipose, 50% glandular.[133] However, studies have investigated thicknesses ranging from 2 to 12 cm and compositions ranging from 0% adipose-100% glandular to 100% adipose-0% glandular, in an effort to provide thorough estimations of the dose ranges for different breast compositions.

As mentioned in the previous section, the D_{gN} value can be determined through numerous simulation methods. One of the most common methods is a Monte Carlo calculation,[46-47] which performs a simulation of a mammographic exam incorporating a specific set of values for the D_{gN} factors. Monte Carlo simulations are applied through creating a mathematical model representing the breast dimensions and composition, along with the x-ray beam utilized for imaging. The x-ray imaging procedure is simulated, and photons are selected stochastically for tracking. The number of tracked photons that are deposited inside the breast model is utilized to determine the total energy deposition for calculation of the average glandular dose coefficient. Present day computers can simulate approximately 10^8 photons for tracking; however, a single mammographic exam can generate approximately 10^{12} photons. Although the number of photons tracked in the Monte Carlo simulations is much smaller than the actual number of photons in a clinical exam, the calculated coefficients have exceptional precision.[111]

Due to the complexity of the calculation, as well as the small range of values for each factor that currently exists for mammography, numerous studies have published tables of values for use in both clinical and research environments.[113, 143-154] However, measurements performed with non-typical mammography values, such as investigational studies performed with higher x-ray energies as presented in this research, require new D_{gN} calculations to be performed. Therefore, the D_{gN} values for the studies presented in the following chapters will be estimated according to the experimental parameters through a Monte Carlo simulation process detailed in previous studies.[152-154] The Monte Carlo breast model designed for the dissertation research will assume a semi-elliptical breast shape with a uniformly distributed composition of glandular and adipose tissue, which is contained by a layer of skin with thickness of 0.4 cm.[152-153] The assumed shape represents a typical compressed breast for the craniocaudal projection, and is also utilized by the FDA in development of dosimetry tables.[150] The simulation will consist of a range of breast thicknesses, as well as compositions ranging from 100% glandular- 0% adipose to 0% glandular- 100% adipose, which represent breast compositions from dense to fatty breasts. Elemental compositions of both types of tissues will be consistent with previous studies;[152, 155] along with the photon cross sections, form factors and scattering functions[156] utilized for calculation of the mass attenuation coefficients for the tissue compositions. The Monte Carlo model will be applied to each x-ray spectrum corresponding to a particular set of D_{gN} values, which will be acquired through the use of a spectrometer as detailed previously. Each spectrum will first be normalized into bins representing x-ray energies with 1 kV increments. The normalized average

glandular dose coefficient corresponding to each set of D_{gN} factors will then be estimated from the corresponding spectrum through weighting the spectrum value for each energy increment with the corresponding mass attenuation coefficient. The resultant D_{gN} value represents the conversion factor in Eq. (28), and the average glandular dose D_g is then determined through multiplication by the object entrance exposure.

3 Development and Characterization of a Low Energy Phase Contrast System Prototype

3.1 System Design

3.1.1 X-ray Source Specifications

A microfocus x-ray source (Model L8121-01, Hamamatsu Photonics, Japan) was utilized for the prototype system design. The x-ray tube consists of a tungsten target and a beryllium output window with a thickness of 200 micrometers (μm). The distance from the focal spot to the output window is 17 μm, and the diameter of the focal spot is 7 μm for tube operation at an output power of 10 Watts (W). The source provides adjustable tube current and adjustable tube voltage ranging from 40 to 150 kilovolts (kV), which are controlled precisely by a software application interfacing directly with the x-ray source. The parameters must be varied inversely to deliver a constant power output in order to maintain a consistent focal spot size.

3.1.2 Image Detection Systems

Two image detection systems were utilized in the image quality comparisons to provide a thorough investigation between images acquired on systems with varying image formulation methods, dynamic ranges and limiting resolution values. The first system applied the technology of computed radiography (CR),[20] which utilizes imaging plates to absorb the incident x-rays and store the intensity information until a readout process is performed by the system. The readout process formulates a digital

image corresponding to the intensity values recorded at each pixel location. The CR system employed for this research (Regius 190, Konica Minolta Medical Imaging, Wayne, New Jersey) provides mammography plate processing with a sampling frequency of 43.75 μm, and the size of the plates utilized was 24 by 30 centimeters (cm).

The second detection system was a direct flat panel detector system,[20] which formulates images through the use of a thin film transistor (TFT) matrix with a layer of photoconductor material on the surface. Direct detection involves formulating the image directly from the x-ray interactions with the photoconductor material, instead of utilizing a scintillator to convert the x-ray photons to visible light photons first. The direct flat panel detector system (DirectRay, Hologic Corporation, Delaware USA) employed in this study utilizes amorphous selenium as the photoconductor material and a TFT matrix active area with dimensions of 14 by 17 inches, or 35 by 43 cm, and provides a sampling frequency of 139 μm. The detector is controlled through a software application provided by the manufacturer, which enforces a maximum exposure time of 30 seconds. In addition, careful consideration must be taken in selection of the x-ray configuration settings to avoid saturation of the image by exceeding the upper limit of the dynamic range.

3.1.3 Geometry of the Imaging System

The prototype system allows operation in both conventional and phase contrast mode through utilizing the corresponding configurations, both of which are illustrated in

Figure 7. The ability to employ the same system for both conventional and phase contrast images provides an extremely accurate comparison between the modes. As demonstrated in the figure, the conventional mode consists of the object in contact with the detector, while the phase contrast mode relies on the air gap between the object and the detector. As detailed in Section 2.3.2, the phase contrast effect is produced during the propagation of the x-rays towards the detector after exiting the object. The distance traveled by the x-rays before reaching the detector (*R2* in Figure 7) controls the amount of magnification, which represents a tradeoff between optimal phase contrast effect and image quality. As indicated previously, the value of 2 has been reported to provide an adequate balance for this tradeoff, and was therefore utilized as a starting point for the evaluation of the optimal magnification factor for this research. The investigation consisted of image quality evaluation across a range of magnification factors, in an effort to determine the optimal value for the low energy phase contrast system prototype. The results of the evaluation demonstrated that a magnification factor of 2.8 was optimal for the system.[36, 44]

3.1.4 Development of System Alignment Procedure

The system prototype was designed and constructed for the purpose of this research, and consists of the source, object and detection components mounted at precisely-adjustable locations along the supporting structure. As detailed previously, the system provides flexibility for configuration in either conventional or phase contrast mode, through placement of the object either in contact with the detector or a specific distance in front of the detector to introduce the air gap for phase contrast imaging.

The system also allows the simple and precise placement of additional components, such as x-ray exposure and spectrum measurement devices. This flexibility facilitates efficient and reliable adjustment of the necessary components of the system, which is extremely useful in a research environment.

A significant consideration in ensuring accurate x-ray image and measurement acquisition is maintaining exact alignment among all of the components.[52, 108-110, 157-161] For this reason, a precise alignment approach based on the use of two laser positioning devices was developed for this research.[162] Previous studies had reported alignment techniques based on a single laser or similar methods, such as the combination of a laser projector and reflectors to indicate the correct relative position between the subject, detector and the x-ray beam,[52, 157, 160-161] the combination of laser positioning and pinhole focal spot radiography,[109, 158] the use of a single laser indicating the focal spot position,[108] and the use of a multi-pinhole plate and telescope-based observation,[110] but the two-laser approach had not been presented previously, to the best of my knowledge.

The new technique involved the use of one laser pointing towards the x-ray source, parallel to the axis on which the object, detector and other imaging devices are placed, and a second laser originating from the opposite direction and calibrated to coincide with the first beam. The coincident beams thus provide a visible indication of the path of the x-ray beam, which can be utilized as a convenient and accurate guide for alignment of the imaging and measurement devices within the beam.

A thorough investigation of the accuracy of the method was performed, through measurement of the degree of coincidence of the laser beams on a transparent grid with one millimeter spacing. The *(x, y)* grid coordinates for each beam were measured separately at several locations along the supporting structure, by adjusting the placement of the transparent grid on the structure and recording the precise coordinates of the beam on the grid. The same grid coordinates were recorded for both beams, which confirmed the precise coincidence of the laser beams for the one millimeter grid precision. In addition, the beams both produced constant grid coordinate values regardless of the position of the transparent grid along the supporting structure.

The application of the laser alignment procedure to the acquisition of an x-ray spectrum was also performed, in an effort to demonstrate the operation of the procedure as well as to verify the importance of precise alignment. The x-ray spectrum was measured through the use of an x-ray spectrometer with a 3 x 3 x 1 mm^3 Cadmium telluride (CdTe) detector (Amptek Incorporated, Bedford, Massachusetts), using a pair of tungsten collimators provided by the manufacturer.[163] The alignment process is necessary to ensure that both collimators are aligned in the path of the x-ray beam, and the x-ray beam output from the collimators is centered on the input window of the CdTe detector. Previous to the use of the dual-laser alignment process, this alignment presented a significant challenge. However, the application of the dual-laser alignment process adequately achieves and verifies the precise alignment of the collimators and detector with the x-ray beam.

3.2 Image Quality Evaluation

A comprehensive image quality investigation was conducted to evaluate the performance of the low energy phase contrast system prototype in comparison with conventional imaging. The following sections detail the comparison studies performed, including a thorough description of the methods and results for each comparison.

3.2.1 CDMAM Observer Study

The first comparison study comprised of a contrast-detail comparison of phase contrast and conventional x-ray imaging operation of a system prototype.[44] As detailed in Section 2.1.3, contrast-detail evaluation is a widely-accepted subjective image quality comparison method that demonstrates the quality provided by a system according to the ability of observers to distinguish test objects of varying size and contrast in the images. Also detailed previously, the use of the CDMAM phantom for the contrast-detail analysis further enhances the accuracy of the observer study results, as it provides a four alternative forced-choice location of the test objects instead of known locations. To the best of our knowledge, a CDMAM comparison of phase contrast and conventional imaging had not previously been presented.

In this study, a tube potential of 60 kV and a tube current of 167 μA were utilized for both conventional and phase contrast images. In an effort to provide numerous comparisons, three sets of images were acquired at exposure times of 30, 40 and 50 seconds, which correspond to 5.01, 6.68 and 8.35 milliampere-seconds (μAs),

respectively. As detailed previously, the tube current multiplied by the exposure time is a commonly used measurement in x-ray imaging, as the two quantities together are proportional to the quantity of x-ray photons incident on the object, which is desired information for dose estimation purposes. Six images were therefore acquired for comparison, and the computed radiography image detection system was utilized for image retrieval. The conventional and phase contrast images acquired with the shortest exposure time are provided in Figure 8 (a) and (b), respectively.[44] The qualitative comparison clearly reveals improved contrast in the phase contrast image. The remaining two sets of comparison images reveal similar results and will therefore be omitted for purposes of brevity.

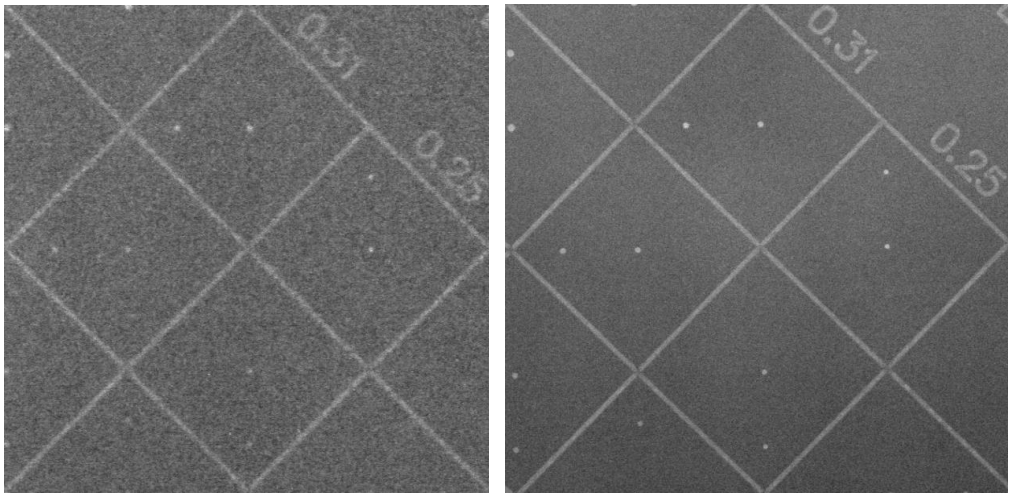

(a) (b)

Figure 8: Comparison of CDMAM images acquired at 60 kV, 167 µA and 30 s in (a) conventional mode, and (b) phase contrast mode.

After acquisition of the six images, the CDMAM observer study process presented in Section 2.1.3 was conducted with a group of five independent observers. After each of the observers had scored the images by indicating the location of the corner object

for each square in which the object was distinguishable, the grading and correction schemes were applied to obtain the final result for each observer. The observer results were then averaged and a contrast-detail curve was generated for each of the six images, providing separate quantitative comparisons between phase contrast and conventional imaging for each of the µAs values utilized. The comparison of one set of curves is provided in Figure 9.[44] As detailed previously, superior image quality is demonstrated by the closer proximity of the phase contrast curve to the x-y axis, indicating improved resolving power for objects with smaller diameters and lower contrast. Statistical comparison methods were then applied to each set of comparison curves through constructing a Student *t* confidence interval around each point, as detailed in Section 2.2.1. The statistical difference in image quality between the phase contrast and conventional images is demonstrated by the noticeable separation of confidence intervals on the curves in Figure 9. The results were consistent for all exposure times utilized in the study.

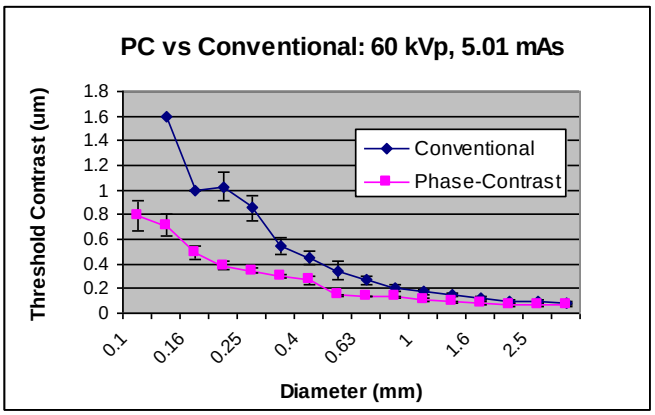

Figure 9: Comparison of contrast-detail curves generated from the observer study comparing conventional and phase contrast images at 60 kV, 167 µA and 30 s.

The results of the side-by-side comparison of the CDMAM phantom images and the contrast-detail curves generated from the observer study both clearly indicate improved image quality provided by the phase contrast images as compared to the conventional images.

3.2.2 ACR Observer Study

The next image quality comparison between phase contrast and conventional images at the same x-ray energy consisted of an observer study utilizing the ACR phantom.[36] As detailed in Section 2.1.3, the ACR phantom represents a standard image quality control procedure for clinical mammography systems and is therefore a widely-accepted comparison method for research environments.

In this study, three sets of experimental settings were utilized in an effort to provide a thorough comparison between phase contrast and conventional imaging. This was accomplished by adjusting the tube potential across a range from 40 to 60 kV, while altering the tube current to maintain a constant focal spot diameter. The exposure time was held constant at 30 seconds, and the corresponding energy and current values were as follows: 40 kV and 250 μA, 50 kV and 200 μA, and 60 kV and 166 μA. The settings correspond to μAs values of 7.5, 6.0 and 4.98, respectively. The wax insert of the ACR phantom was imaged alone, in an effort to improve the contrast within the image to account for the relatively low exposure level. Six comparison images were therefore acquired, and the flat panel image detection system was utilized to retrieve the images. The conventional and phase contrast images corresponding to the shortest

exposure time are provided in Figure 10 (a) and (b), respectively.[36] As in the CDMAM study, the qualitative comparison clearly demonstrates improved contrast in the phase contrast image. The remaining two sets of comparison images reveal similar results and will therefore be omitted. Next, an ACR observer study was performed to provide a quantitative comparison of the phase contrast and conventional images, following the procedure presented in Section 2.1.3. The images were randomly presented to eight independent observers for analysis according to the mammography quality control guidelines detailed previously. The results were then averaged to determine individual scores for fibers, specks and masses, as well as an overall combination score for each of the six comparison images. The results are provided in Table 1.[36] As demonstrated in the table, the phase contrast images exhibit dramatically improved image quality in each of the individual categories as well as the overall score.

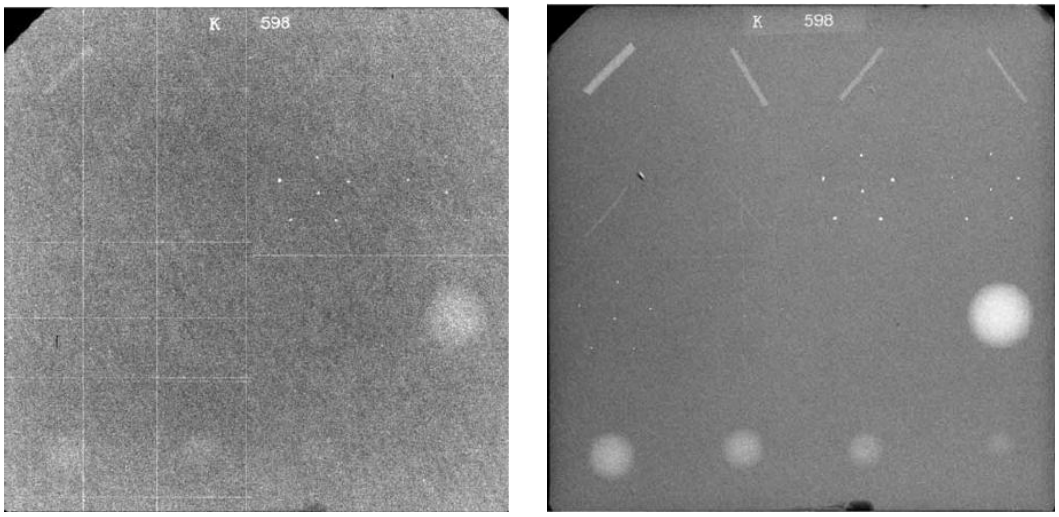

(a) (b)

Figure 10: Comparison of ACR images acquired at 40 kV, 250 µA and 30 s in (a) conventional mode, and (b) phase contrast mode.

The results of the qualitative comparison of the images and the quantitative comparison of the observer study results both demonstrate the superior image quality provided by phase contrast imaging at the same x-ray energy.

Conventional	40KV	50KV	60KV
Fibers	2.19	2.44	1.88
Specks	2.25	1.94	1.88
Masses	3.06	2.25	2.19
Reading	7.50	6.63	5.94
Phase contrast	40KV	50KV	60KV
Fibers	4.94	4.88	4.31
Specks	3.94	3.75	3.63
Masses	4.38	4.31	4.13
Reading	13.25	12.94	12.06

Table 1: Comparison of ACR observer study results for three sets of comparison images between phase contrast and conventional modes.

3.2.3 Tissue-equivalent Phantom Image Comparison

The final study in the comprehensive image quality investigation involved a clinical comparison method utilizing a tissue-equivalent material. Raw chicken breast tissue of varying sizes and thicknesses was utilized to represent actual clinical mammography procedures. Human breast biopsies typically yield samples with a thickness of around one mm, while lumpectomies are much thicker, depending on the breast and abnormality sizes. In an effort to replicate both types of mammography procedures, chicken breast samples of one mm and four mm were both utilized in this study. Phase contrast and conventional comparison images at 40 kV, 250 µA and 30 s were acquired for each of the chicken breast tissue thicknesses. The setting corresponds to an µAs value of 7.5. The flat panel image detection system was

utilized to retrieve the images. The conventional and phase contrast images acquired of the one mm thick chicken breast specimen are provided in Figure 11 (a) and (b), respectively.[36] As demonstrated in the figure, the structures within the chicken breast sample exhibit improved definition and sharper contrast in the phase contrast image than in the conventional image. An area that clearly illustrates the enhanced image quality has been highlighted with red rectangles in the images, and one can see how the structure is clearly defined in the phase contrast image but barely distinguishable in the conventional image.

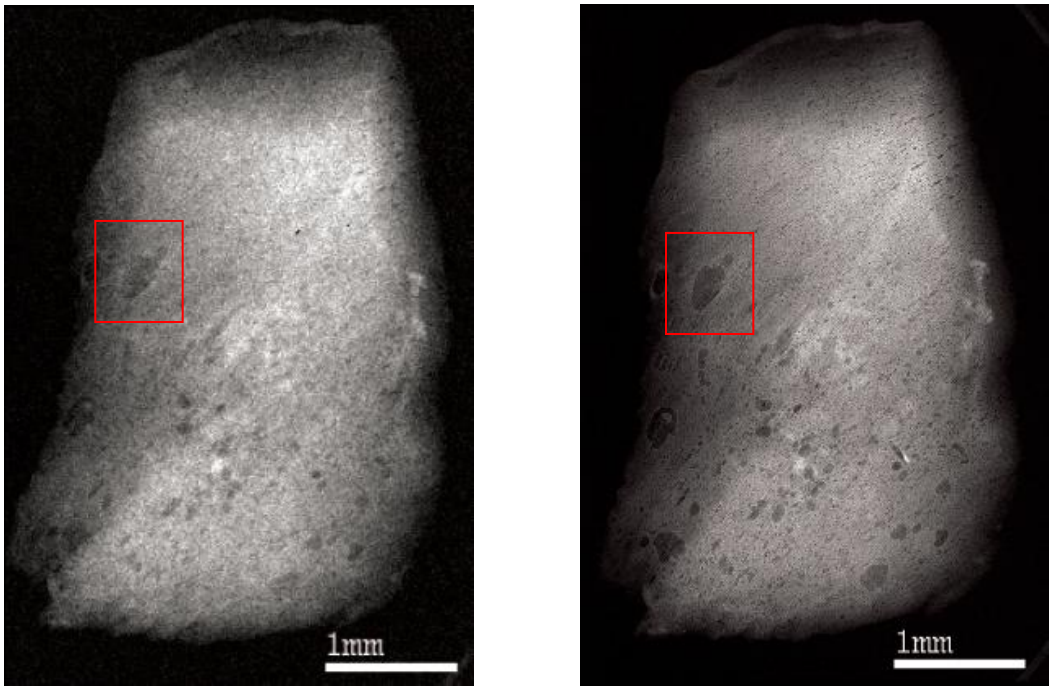

(a) (b)

Figure 11: Comparison of 1 mm thick chicken breast images acquired at 40 kV, 250 µA and 30 s in (a) conventional mode, and (b) phase contrast mode.

Next, Figure 12 (a) and (b) provide the images of the four mm thick chicken breast specimen in conventional and phase contrast mode, respectively.[36] As evident in the

thinner samples, the structures within the chicken breast are much more clearly distinguished in the phase contrast image. The dark area in the upper left corner of the chicken breast, which has also been highlighted with red rectangles, particularly demonstrates the edge enhancement provided by the phase contrast effect. Note the clear definition of the boundary of the structure in that image as compared to the conventional image.

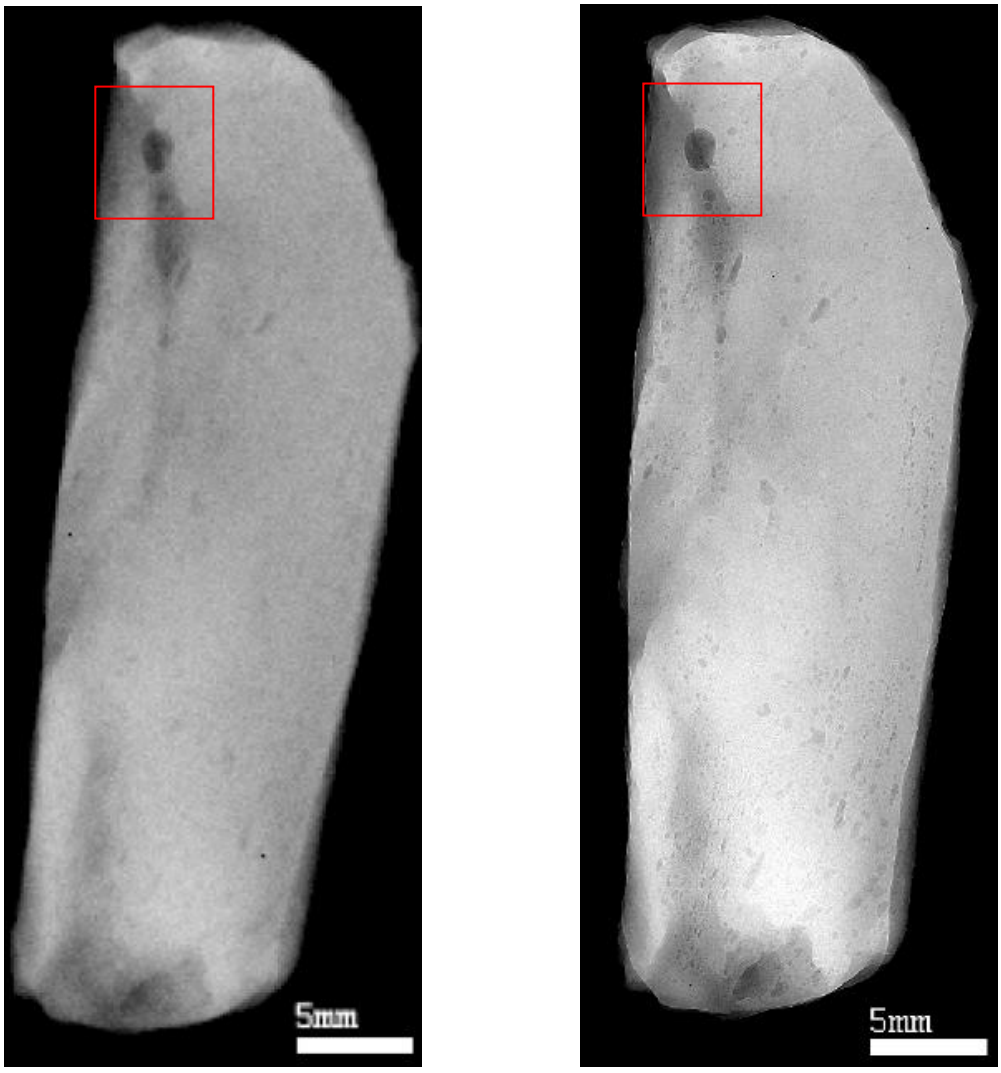

(a) (b)

Figure 12: Comparison of 4 mm thick chicken breast images acquired at 40 kV, 250 µA and 30 s in (a) conventional mode, and (b) phase contrast mode.

In summary, the comprehensive image quality comparison including a CDMAM observer study, an ACR observer study and a tissue-equivalent study demonstrated the capability of phase contrast imaging to significantly improve the image quality as compared to conventional imaging for the same x-ray energy and patient dose. These results are an encouraging indication of the potential of phase contrast imaging in a clinical environment.

4 Optimization of the MTF Edge Algorithm

4.1 Background

As detailed in Section 2.1.2, the modulation transfer function (MTF) provides a comprehensive description of the resolution properties of an imaging system, and is therefore an established evaluation of image quality. The MTF is frequently used in clinical environments for verification of existing systems, as well as in research environments for investigation of new systems. Due to its widespread utilization, the procedure for determining the MTF has received continual research focus since the early studies presenting the ability to calculate it through normalizing the absolute value of the Fourier transform of the LSF.[164-165] As detailed previously, the LSF can be determined directly from the response of the imaging system to a line stimulus, and numerous studies have presented the MTF calculation through this technique, which is referred to as the slit method.[54-58] However, the slit method requires the use of an expensive test device and faces several acquisition and processing challenges. A second method for efficient and accurate determination of the MTF has recently been investigated in an effort to alleviate these issues.[52-53, 59-64] The new method, which has been designated the edge method, involves determining the LSF through differentiating the ESF, which is the response of the imaging system to an edge stimulus. As detailed previously, the ESF is a simpler imaging system response procedure, due to the use of a sharp edge instead of a very narrow line. Thus the ESF is not as sensitive to physical imperfections, system misalignment or scattered radiation.[52-53] The performance of the edge method in providing accurate results in

direct comparison to the slit method has been verified.[52-53, 62] In addition, direct comparison of the low frequency response, which is critical due to its dependence on the tails of the LSF, has revealed that the edge method provides accurate results for low frequency values,[52-53, 62, 65] while obtaining adequate exposure to precisely estimate the tails has proven to be a difficult challenge for the slit method.[53]

The algorithm for calculation of the MTF using the edge method consists of several steps: determination of the ESF from the imaging system response, calculation of the LSF by differentiating the ESF, and evaluation of the MTF using the Fourier transform of the LSF. In addition, smoothing methods are typically applied to the ESF and LSF before proceeding to the next step. The consecutive application of each step to the results from the previous step heightens the importance of maintaining the integrity of the data and minimizing the addition of noise, as the negative effects introduced in one step could become amplified through propagation to the subsequent steps. Consequently, the accuracy of the calculation of the MTF depends significantly on the efficient and precise calculation of each algorithm step.

The significant research focus on the edge method, as well as the existence of numerous algorithm steps, has resulted in the development of several different methods for calculation of the MTF. The overall results provided by six different edge techniques were compared in a previous research study,[66] but separate comparisons of the results provided for the individual algorithm steps had not previously been presented, to the best of our knowledge. Therefore, the goal of this

research study[51] was to perform separate in-depth investigation of the methods available for each algorithm step, and optimize the algorithm by selecting the method providing superior results for each step. In addition, the study presented several new techniques or combinations of techniques that had also not previously been applied to the MTF algorithm, which delivered comparable or superior results to the established methods.

4.2 Experimental Design

The images analyzed in this study were acquired through the use of a charge-coupled device (CCD) x-ray imaging system (MX20, Faxitron X-Ray Corporation, Wheeling, Illinois USA), which utilizes a tungsten target with a beryllium output window and provides a focal spot of 20 µm and a pixel pitch of 48 µm. The detector system consists of two 1024 x 1024 CCD arrays coupled to a Min-R scintillating screen (Eastman-Kodak, New York, New York USA) through optical fiber taper. The test device was placed in the center of one of the arrays for image acquisition, in an effort to avoid discontinuities in the image due to the boundary between the arrays. The source-to-detector distance employed for all images was 57.2 cm, and the object was placed directly in contact with the detector to avoid magnification.

The edge test device was constructed of a copper-tungsten alloy with edge fabrication of 0.0025 mm precision and dimensions of 152.4 mm in length, 101.6 mm in width, and thickness of 1.6 mm. The application of the edge method on a digital radiographic imaging system requires careful consideration to avoid aliasing effects

caused by discrete sampling of the image.[58, 63] Several previous studies have slightly angulated the edge device with respect to the detector pixel array in an effort to obtain the non-aliased response through increasing the effective sampling rate.[52, 54, 56, 60-61, 64-65, 166-167] The resultant MTF is referred to as the presampling MTF, which is a more accurate representation of the image quality of the system due to the absence of aliasing effects. Thus the edge test device was slightly angled during image acquisition in this study to provide the presampling MTF. The experimental parameters utilized were as follows: x-ray energy of 26 kV, tube current of 300 μA and an exposure time of 3 s.

4.3 Development of the Optimal Algorithm

As detailed previously, the edge algorithm incorporates numerous steps in the determination of the MTF from the image of the system response to the edge stimulus. A flow chart of the algorithm steps is given in Figure 13.[51] The first and last steps will not be discussed in detail: the acquisition of the edge image was presented in Section 4.2 and provides the starting point for the investigation, and the calculation of the MTF from the LSF through Fourier Transform is the technique utilized by a majority of the existing methods. The remaining algorithm steps incorporate the focus of this study. The following sections detail the evaluation of the methods available for each step, as well as the results corresponding to each method.

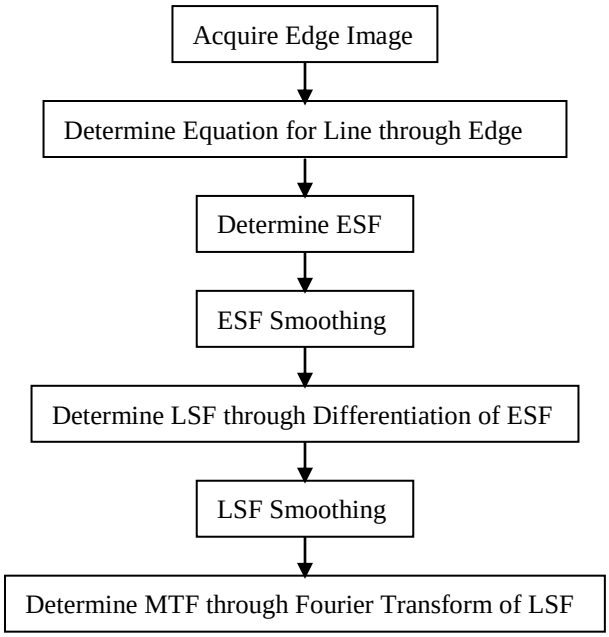

Figure 13: Flow Chart of Processing Steps in MTF Edge Algorithm

4.3.1 Edge Equation

The first edge algorithm step involves determining the equation of the line through the edge. As the first step in the edge method, it is critical to accurately locate the edge in the image and determine the corresponding line equation to provide accurate input for the remaining algorithm steps. Several methods have been utilized in previous studies for accomplishing this step, the first of which is the use of linear regression to determine the equation of the line.[60-61, 64, 102, 168-169] This is performed through estimating the edge location in each row according to the transition of intensity values across the edge, which is a three step process. First, the mean minimum and maximum intensity values in the image are determined through averaging the minimum and maximum values in each row. Next, the midpoint between the mean maximum and minimum intensity values is calculated. The edge

location within each row is then determined through averaging the values that are between an upper and lower cutoff from the calculated midpoint. Finally, linear regression using the edge locations is then performed to determine the equation of the line. Selection of the cutoff values is a significant factor in obtaining the optimal fit of the line. Previous studies have utilized 30% to 70%[60] or 25% to 75%[66] as cutoff values, and this study thus investigated a range of values to provide a thorough comparison. The values providing the line equation with closest correspondence to the edge were 10% to 90%, which were selected as the optimal cutoff values in this study.

The second method investigated in this comparison involved applying a Hough transformation[170] to the image to determine the equation of the line, which is a technique that has been extensively applied in image line and curve detection.[171-175] A previous MTF edge algorithm study[52] applied the Hough transformation to determine the line equation of the edge, which involves transforming the data points in the binary image to curves in polar coordinate space. The data points corresponding to lines in the image intersect at a point in polar space, which indicates the angle and position of the line with respect to a reference point in the image.

The last method compared in this study was the Canny method for edge detection,[176] which has been used extensively for edge and curve detection in many applications.[177-181] To the best of my knowledge, the method had not been applied to the MTF edge algorithm previously, but it was selected for the comparison due to the

wide utilization, from detecting cracks in bridges[177] to extracting small retinal vessels.[179] The Canny edge detection method utilizes a three-step process with parameters that allow optimization based on the application. First, the method applies a filter based on the first derivative of a Gaussian for smoothing purposes. Next, the image gradients are calculated and separated according to the edge direction: horizontal, vertical and both diagonals. The algorithm then utilizes a technique called non-maximum suppression to identify edges by searching for local maxima in the same direction as the image gradients. An adaptive thresholding process using hysteresis is then performed to increase the efficiency of the results.

The lines determined through applying the linear regression, Hough and Canny methods, which are superimposed on the edge image for indication of accuracy, are provided in Figure 14 (a) – (c), respectively.[51] As one can see in the side-by-side comparison, the results are comparable. However, the linear regression method provides the closest estimation of the edge, and was therefore selected as the optimal method for this step.

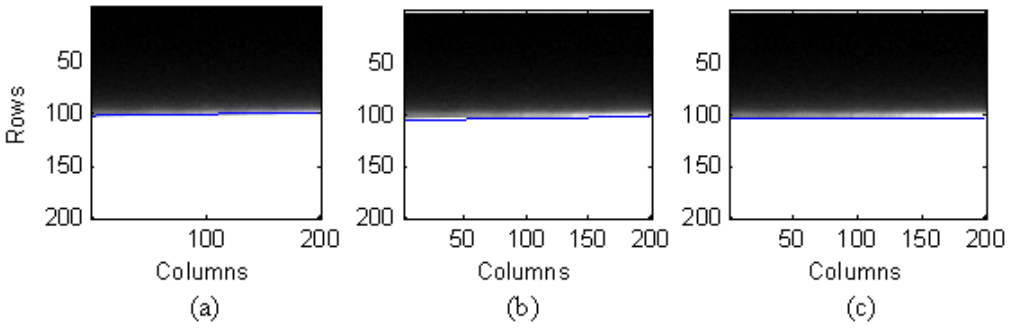

Figure 14: Comparison of edge equation lines determined through the following methods: (a) linear regression, (b) Hough transformation, and (c) Canny edge detection.

4.3.2 ESF Calculation

The second algorithm step involves determination of the edge spread function (ESF), which is a graphical representation of the intensities in the image as a function of the distance from the edge. The ESF is acquired through calculating the distances from pixels in the image to the line that was calculated in the previous step and graphing the corresponding intensities. The challenge in this step is selection of the pixels to utilize, as applying the calculation to the entire image would provide an excessive number of data points. Due to the Poisson nature of x-ray photons discussed previously, the pixels within the image exhibit random fluctuations among the intensity values, which would result in an image distorted by noise if too many pixels were utilized. Thus a region of interest (ROI) must be selected for processing, which contains a specified number of rows and columns on which to perform the ESF calculation. The selection of the size of the ROI is a critical step in the edge algorithm and involves a tradeoff, as it must contain enough rows and columns to adequately represent the ESF but avoid providing redundant points resulting in excessive noise. Previous studies have attempted to balance this tradeoff based on the angle of orientation of the edge α, through the use of the following formula:[54, 60]

$$N = \frac{1}{\tan\alpha}, \tag{29}$$

where N is the number of rows and columns to utilize, and the edge angle was determined in the previous step. The value of N was calculated to be 59.97 for this study, thus 60 was utilized as the starting point for this investigation. In order to determine whether this value was optimal, comparisons were made with a range of

values for N from $0.5N$ to $2N$. As can be seen in Figure 15 (a) through (c), the range exhibits the tradeoff detailed above, and the extreme values do not consist of an effective balance.

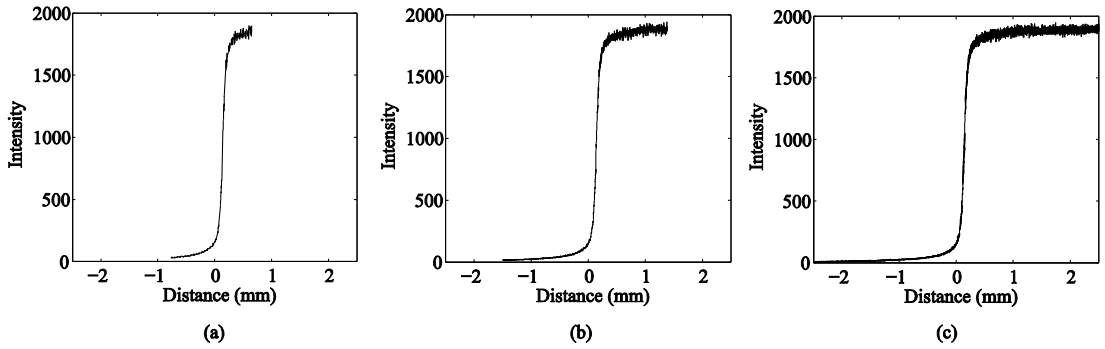

Figure 15: Illustration of ESF curves resulting from different ROI sizes of (a) 30, (b) 60 and (c) 120 rows and columns around the edge.

In addition to comparing results from different values of , this study also investigated a new approach to determining the ROI size by employing different numbers of rows and columns, in an effort to investigate their separate influence on the results. This was accomplished by utilizing a constant value for one while varying the other across the range from $0.5N$ to $2N$. First, the number of rows was altered while maintaining a constant column number, and following intuition, this increases the distance across the edge represented by the ESF, as illustrated in Figure 16.[51]

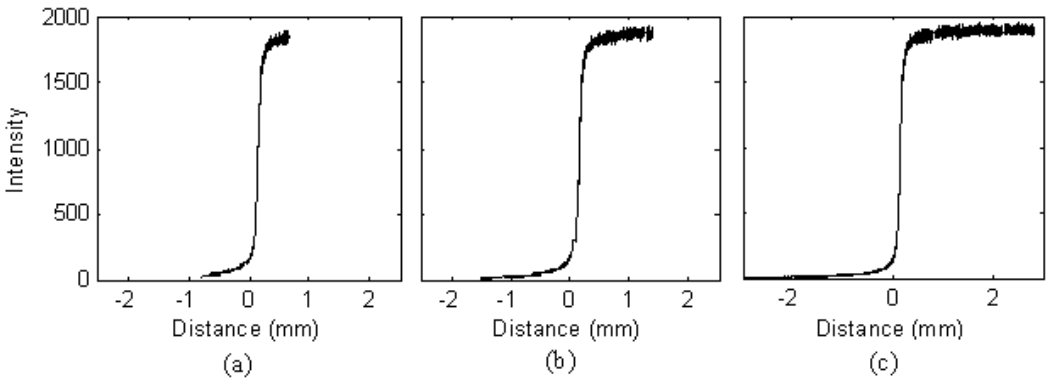

Figure 16: Illustration of ESF curves resulting from ROI sizes of 60 columns and (a) 30, (b) 60, and (c) 120 rows across the edge.

Secondly, the number of columns was varied with a constant number of rows, and the results in Figure 17[51] indicate that the number of columns utilized affects the amount of random fluctuation produced in the image. This is also expected, as increasing the number of columns increases the number of redundant data points. The significance of identifying the separate influence of the number of rows and columns involves the ability to solve the previous challenge of balancing the tradeoff to include an adequate distance across the edge without including an excessive amount of redundant data points. The ROI size can therefore be optimized easily by selecting separate values for the number of rows and columns. For example, the number of rows utilized can be increased to incorporate the desired distance across the edge, while the number of columns can be decreased to utilize the desired amount of data points. In this study, the use of 120 rows and 30 columns represents the optimal ROI size for data integrity without excessive noise. To the best of my knowledge, separate row and column sizes had not previously been utilized.

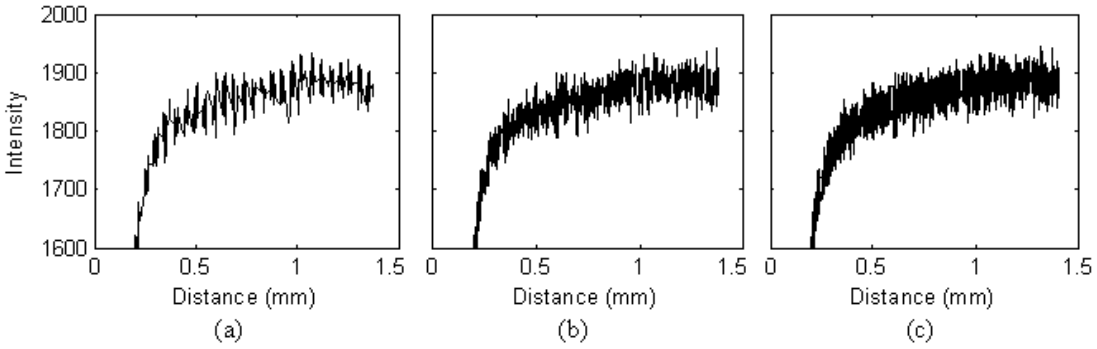

Figure 17: Illustration of ESF curves resulting from ROI sizes of 60 rows and (a) 30, (b) 60, and (c) 120 columns across the edge.

4.3.3 ESF Smoothing

The next edge algorithm step consists of smoothing the ESF determined in the previous step, in an effort to reduce the noise negatively contributing to the calculation while maintaining the data integrity. The selection of the smoothing method is critical, as it must provide an optimal balance between these goals. In this study, comparison of several methods utilized previously was conducted, along with thorough comparison of each method to the original data for verification of data accuracy. First, a data binning method has been used in numerous studies, which involves separating the data into bins with size relative to the pixel pitch and calculating the mean value of each bin.[52, 102, 168-169, 182-183] Many studies also applied a second smoothing step through various techniques, including an averaging filter[60-61] and a polynomial fit method,[52-53, 183] both of which were compared in this study. In an effort to provide a thorough comparison, the investigation also involved the use of a median filter, which had not been reported previously. The comparison of smoothing methods was applied through an iterative approach, due to the fact that previous

studies utilized both one-step and two-step smoothing processes. First, the results provided by each method were compared separately, followed by a comparison of combinations of methods applied in two-step processes. Although a three-step process had not previously been applied to the best of my knowledge, it was also investigated in this study to evaluate the possibility of improving the algorithm. Within each method, additional design considerations must be made in selecting the parameters with which to apply the method. These decisions must be made carefully to optimize the balance between the amount of smoothing and maintaining the data integrity. Therefore, the first step in this study of comparing the results provided by the individual methods must also consist of optimizing the design parameters for each method. First, the data binning method requires selection of the size of the bins into which to separate the data. Previous studies have utilized 10%,[52, 102, 183] 20%,[182] and 25%[168-169] of the pixel pitch size, all of which were evaluated in this study to provide a rigorous comparison. Next, the median and averaging filters require selection of a window size, which corresponds to the size of the squares into which the image is separated for determination of the median or average value, respectively. Studies have indicated use of a window size of 7[183] and 17[52] pixels, and a comprehensive comparison was provided in this study through the use of 7, 12, 17 and 20 pixels. The polynomial fit method did not require the selection of any design parameters.

The investigation of the ability of each method to reduce noise while maintaining the data integrity requires thorough comparison in two critical regions of the ESF: the upper tail and the edge transition. First, the upper tail consists of the maximum

intensity values, which experience the highest degree of random fluctuation inherent in x-ray images. Therefore, the upper tail exhibits the largest amount of noise within the image, which facilitates the most effective comparison of smoothing effects. Secondly, the edge transition represents the most essential region in which to maintain the data integrity, due to the fact that the distance of the edge transition corresponds to the image quality provided by the imaging system.[39] The data integrity verification in this study was therefore conducted through comparisons of the results within the edge transition region. First, the results of the data binning method in Figure 18[51] indicate a considerable amount of smoothing while maintaining the integrity of the data within 0.001 for all bin sizes. Note that the comparison in the upper tail does not include the original data, due to the fact that the amount of noise encompasses the entire range given in the figure. The bin size of 20% was selected for subsequent testing, as it provides an optimal balance between smoothing and data integrity. This is demonstrated through the small difference between the amount of smoothing provided by the 20% and 25% bins, combined with the large difference in data integrity between the two sizes.

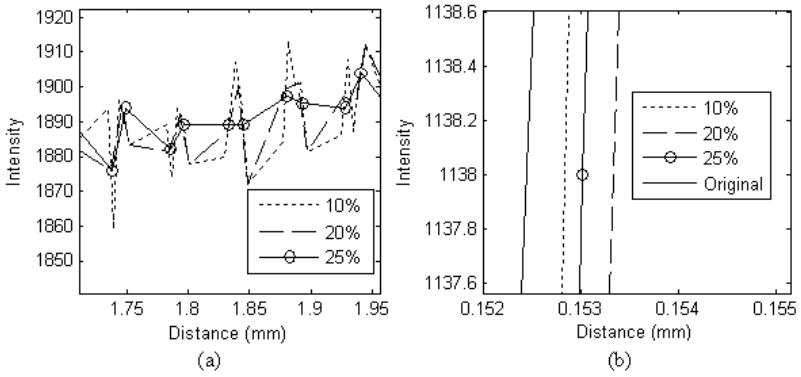

Figure 18: ESF smoothing with data binning method in (a) the upper tail and (b) the edge transition, using a range of percentages of pixel pitch for bin size.

Next, Figure 19[51] provides the smoothed ESF curves produced by the average filter, which also demonstrate smoothing in the upper tail. However, the data integrity verification in the edge transition indicates a correspondence of the smallest window size to the original data of only 0.01, while the largest window differs by almost 0.02. Note that this is a factor of 10 to 20 less accurate than the data integrity provided in the data binning method. For application of the average filter in the following comparison stages, the window size of 7 was selected, due to the large divergence of all window sizes from the original data.

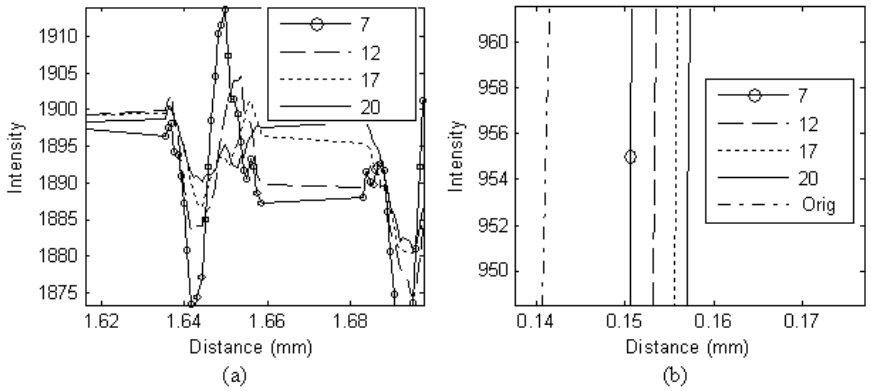

Figure 19: ESF smoothing with average filter method in (a) the upper tail and (b) the edge transition, using a range of window sizes.

The median filter performance is demonstrated in Figure 20.[51] The comparisons in the upper tail exhibit an acceptable amount of smoothing provided by all window sizes. In the edge transition, the results from all window sizes except the largest are completely superimposed on the original data, which indicates extremely high integrity of data. Even for the largest window size, the results differ from the original data by less than 0.0005. However, due to the large amount of both data integrity and smoothing, the window size of 17 was selected for further comparisons.

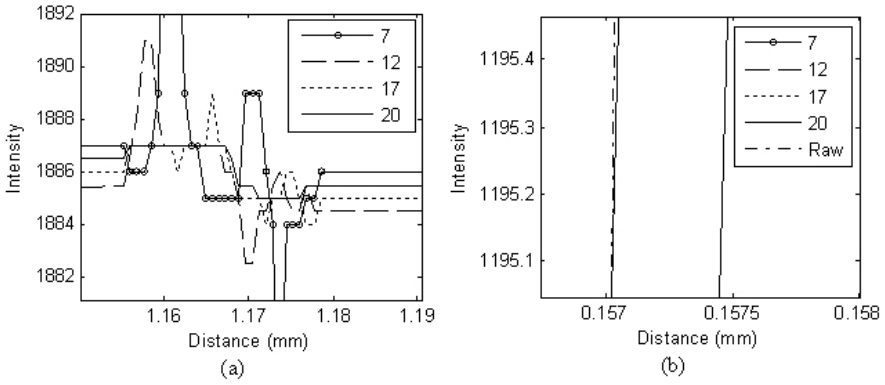

Figure 20: ESF smoothing with median filter method in (a) the upper tail and (b) the edge transition, using a range of window sizes.

Finally, the polynomial fit method results are given in Figure 21. Due to the absence of parameters, the results are included with the original data in both critical regions. Within the upper tail, one can see the considerable amount of smoothing provided, and the edge transition demonstrates data integrity within 0.005 of the original data.

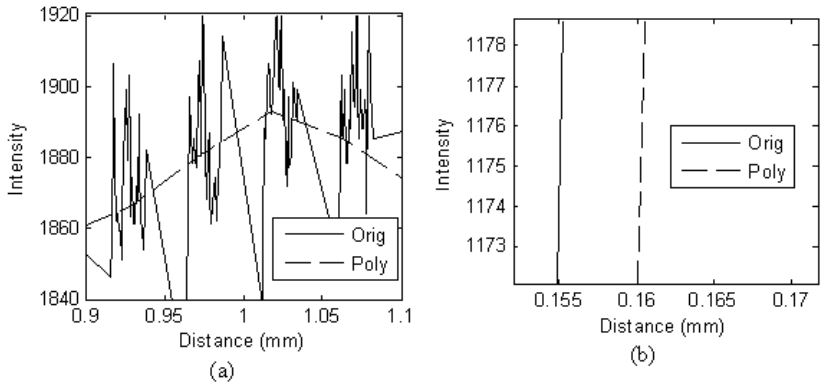

Figure 21: ESF smoothing with polynomial fit method in (a) the upper tail and (b) the edge transition.

The next step in the investigation of this algorithm step involved application of the four methods iteratively in all combinations of two- and three-step processes to determine the optimal balance between smoothing and data integrity. Due to the large number of combinations, the complete set of results will not be provided. The

process delivering the ideal amount of smoothing while maintaining the data integrity proved to be a three-step process, involving subsequent application of the data binning, polynomial fit and median methods. This result is significant, not only due to the fact that the median filter had not previously been applied to the edge algorithm for determination of the MTF, but also because a three-step process had not been previously utilized in the algorithm. The results from the three-step smoothing process are provided in Figure 22:[51] the resultant ESF curve is given in (a), while the comparison to the original data within the edge transition is provided in (b), which illustrates the data integrity within 0.001.

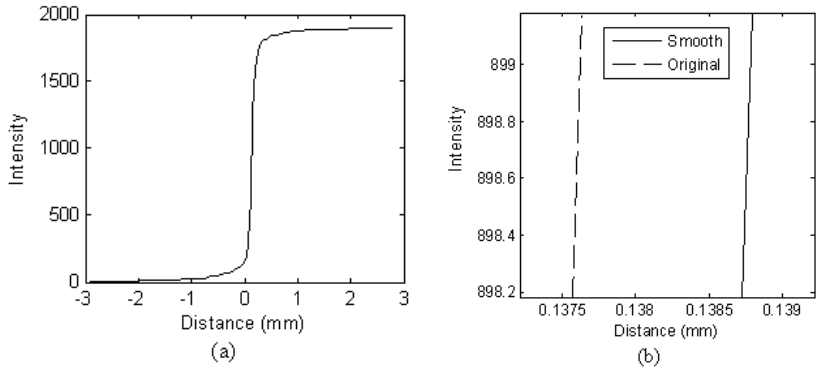

Figure 22: Results from ESF smoothing with a three-step iterative process of data binning, polynomial fitting and median filter smoothing. The entire ESF curve is given in (a) and the data integrity along the edge transition is illustrated in (b).

4.3.4 LSF Calculation

The next step in the MTF edge algorithm investigation consists of the calculation of the line spread function (LSF), which is accomplished through differentiation of the smoothed ESF determined in the previous step. Previous studies generally concur on the use of convolution methods to perform finite element differentiation,[60-61, 168-169] but the selection of kernel size has ranged considerably from two element approaches

with (-1, 1) or (1, -1) to three element methods using (-1/2, 0, 1/2) or (-1, 0, 1). Also, a few studies have applied a correction method to the results of the convolution, due to concerns that discrete sampling reduces the accuracy of the results.[60, 184] However, several studies[52, 62, 168, 183, 185] have demonstrated that careful application of the methods in the previous step can compensate for the finite-element differentiation, thereby making correction unnecessary by providing convolution results with little variation from the direct differentiation results. For example, the use of the slight angle of orientation of the edge to provide sub-pixel accuracy with the data binning algorithm,[52, 168] as well as thorough verification of the optimal balance between smoothing and data integrity, were both applied to increase the accuracy of the results to avoid the need for a correction. Therefore, the evaluation of this algorithm step consisted of a thorough comparison of the kernel sizes utilized in performing the convolution, as the number of kernels and their corresponding values encompass the primary variation between the previous studies.

The LSF was determined through convolution of the ESF, using the four kernel values given previously: (-1, 1), (1, -1), (-1/2, 0, 1/2) and (-1, 0, 1). The results were similar among the methods with the same number of elements; however, the results between the two and three element kernels exhibited a much higher degree of variation. The LSF values produced with two and three element convolution are provided in Figure 23 (a) and (b), respectively.[51] As demonstrated in the figure, convolution with the two element kernel produces more fluctuation within the tails, most notably in the right tail. However, the convolution with the three element kernel

resulted in a wider and less distinct peak that does not experience the maximum value at zero. The more accurate characteristics of the two element kernel in producing a narrow, symmetric peak with a maximum at zero overshadow the appearance of more fluctuation in the tails, and therefore the two element method is selected as the optimal convolution method for calculating the LSF from the ESF in this algorithm step.

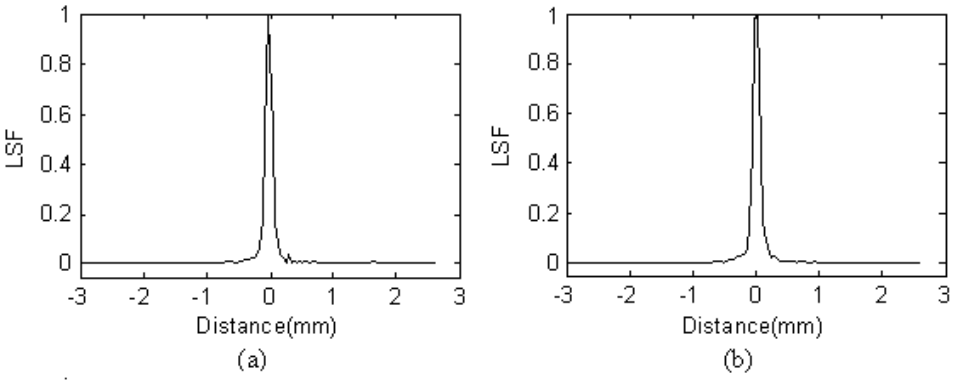

Figure 23: LSF curves calculated through finite element differentiation with (a) two element kernels, and (b) three element kernels.

4.3.5 LSF Smoothing

The next algorithm step involves smoothing of the LSF in preparation for calculation of the MTF by Fourier transform. Noise within the LSF, especially the tails, presents a significant challenge in accurate determination of the MTF; therefore, smoothing the LSF is a critical step in the algorithm. The presence of noise is exhibited by random fluctuations in the LSF values near the end of the tails, which does not provide valid LSF information. As described in detail previously, the theory of the LSF as a representation of the response of the imaging system to a line stimulus dictates that the location of the line corresponds to the maximum intensity values in

the image, and the intensity values gradually decrease to zero as the distance from the line increases. Thus random fluctuations back and forth only represent noise, and previous studies have performed smoothing through several methods: cropping the LSF tails,[60, 62, 182] smoothing the tails through filtering,[62, 182] and fitting the tails to a model.[52, 62] The investigation of this algorithm step involves separate analysis of each method, as well as an iterative approach involving all possible combinations of the methods.

First, the effectiveness of cropping the LSF tails relies on the ability to reduce the noise negatively contributing to the curve without removing the meaningful information. Studies have attempted to optimize this tradeoff through several approaches: removing the data points with values less than a percentage of the maximum intensity value, removing a percentage of the data points, and investigating the intensity values to estimate the location at which the noise overshadows the useful information. A combination of all methods was determined to be optimal in this study. First, the range of points with intensity values less than a threshold was determined as the candidate regions for cropping in each tail. The number of points included in the crop regions were compared to the total number of LSF data points, and if the percentage was larger than 7.5,[182] the size of the regions was decreased appropriately to ensure that the crop region was not excessively large. Finally, the crop regions were manually inspected to ensure that they contained only random fluctuation and not useful data. The resultant LSF curve is given in Figure 24 (a).[51]

Next, median and average filtering methods were both investigated in an effort to determine the method providing the optimal amount of LSF smoothing. As discussed previously, application of both filtering methods requires the selection of a window size. This presents a challenge in the LSF smoothing, due to the fact that the right tail exhibits more noise than the left as a result of the correlation to the upper tail of the ESF curve. As detailed previously, the ESF upper tail demonstrates a higher degree of noise due to the combination of the random nature of x-ray beams with the larger intensity values represented in that area. As a result, the balance between data integrity and smoothing is difficult to achieve in both regions with a single window size. Therefore a new approach was applied in this study, which consisted of applying separate window sizes in filtering of the left and right tails. This allowed the use of an aggressive filter on the noisy right tail and a modest filter on the left tail. The optimal values were determined through an iterative approach involving numerous combinations of window sizes. The results indicated that a window size of 9 for the right tail and a size of 4 for the left tail produced the optimal balance of smoothing and data integrity. The smoothed LSF curves produced by the median filter and the average filter are provided in Figure 24 (b) and (c), respectively.[51] Finally, the use of polynomial fitting to smooth the LSF tails was investigated, and the results are given in Figure 24 (d). Due to the absence of design parameters, the balance between smoothing and data integrity proved a difficult challenge for the method to overcome due to the difference in noise contribution within the left and right tails.

The last step in the LSF smoothing investigation involved an iterative approach of two-step combinations of the four smoothing methods illustrated in Figure 24. Due to the large number of curves represented by the combinations, the comparison of the complete set of results will not be provided. The evaluation determined that the optimal amount of smoothing resulted from LSF cropping through the iterative method presented above, followed by median filtering. The superior performance of the median filter in this smoothing step is significant, as not only had the method not been applied to the MTF algorithm previously, but the results of this study have now demonstrated the ability of the method to provide optimal smoothing in two of the algorithm steps.

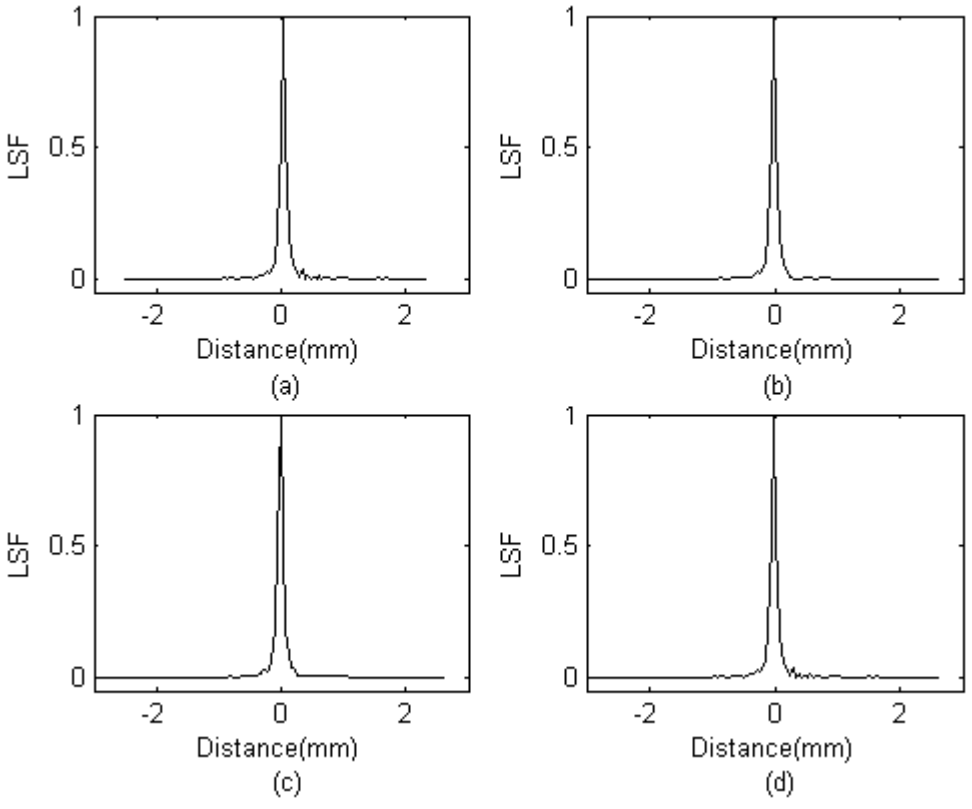

Figure 24: Comparisons of LSF smoothing methods: (a) cropping the tails, (b) median filtering, (c) average filtering, and (d) applying a polynomial fit method.

The MTF edge algorithm flowchart given in Figure 25[51] has been updated with the results of the step by step investigation detailed in the previous sections. As mentioned previously, the calculation of the MTF from the LSF through Fourier transform was consistent among the previous studies and was therefore not investigated in this study, which is indicated through the use of italic font on that step.

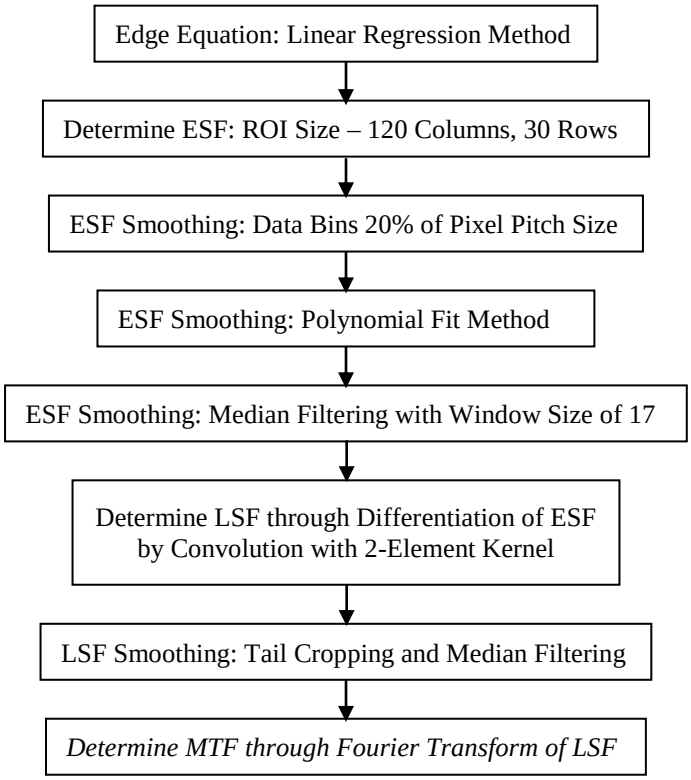

Figure 25: Updated flow chart of the MTF edge algorithm steps indicating the optimal method selected for each step.

The approach of this study in performing independent evaluations of the methods available for each step had not been presented previously, and the significance of separate comparisons has been demonstrated by the results. In addition, this study presented several new techniques or combinations of techniques that had not

previously been applied to the MTF algorithm, which provided comparable or superior results to the established methods. This includes the use of a rectangular region of interest (ROI) for determining the edge spread function (ESF), a new three-step approach to ESF filtering, the use of a median filter for smoothing both the ESF and line spread function (LSF), and the use of different window sizes in smoothing the left and right tails of the LSF. The combination of the use of new methods and the individual selection of the optimal method for each step both indicate the potential of these results to considerably improve the accuracy of the MTF edge algorithm.

5 Comprehensive Error Analysis of Photon Fluence Contribution to the DQE

5.1 Background

A quantitative error analysis method for measurements and calculations was presented in detail in Section 2.2.2. The method holds the potential to benefit a wide variety of applications, not only due to the ability to quantify the error in a measurement or calculation, but also to compare the different sources of error for relative contribution to the overall error. In addition, the method facilitates the calculation of the amount of error propagating from a single measurement or calculation to the final result, which allows the investigation of the significant sources of error in a measurement and evaluation of possible alternatives. As most clinical and research environments perform complicated and multi-faceted measurements and corresponding calculations, optimization of the individual measurements and calculations could greatly enhance the accuracy of the results. The applications of this method are therefore expansive.

The research presented in this chapter consists of applying the method to a single application pertaining to our research focus, in an effort to demonstrate the effectiveness and utility of the method. As detailed previously, the DQE is an established method for obtaining a comprehensive measurement of the image quality provided by an imaging system or technique. Thus the DQE is widely utilized for verification of the performance delivered by new and established systems, and one

can understand the significance of providing an accurate calculation. The challenge in ensuring the integrity of the DQE is revealed by the complexity of the calculation, which was given in Eq. (13). First, the formula consists of several components: large area signal *S(0)*, MTF, NPS and *q*, each of which contribute error to the DQE. With the exception of the large area signal, the quantities represent complicated measurements and corresponding calculations that must also be evaluated for determination of the individual error contributions. Extensive research effort has been focused on improving the accuracy of the NPS[69, 72, 74] and MTF[58, 61, 165] calculations that contribute to the DQE. However, to the best of my knowledge, thorough evaluation of the error contributed by the photon fluence through the x-ray exposure and spectra measurements had not been conducted previously. The goal of this study[103] was therefore to provide a method to determine the error contributing to the DQE calculation through the determination of the photon fluence.

The significant sources of error within the DQE measurement vary considerably according to the system configuration, experimental parameters, measurement methods and processing algorithms. The appropriate factors on which to apply the error analysis were selected according to the system and procedures utilized in our research environment, and therefore the individual error sources and amounts identified in this study may differ from calculations performed in other situations. However, the ability to quantify the error contributed by the measurement of the photon fluence holds great potential to improve the accuracy of the DQE in any environment. Another significant contribution in this study is the development of an

error analysis process that can be applied to any measurement or calculation for determination of error contribution. In addition, a new method for calculating the magnification factor in the exposure calculations was developed for this study, which demonstrates considerably reduced error in comparison to the established method. The following sections provide the details of the error analysis investigation that was conducted in the study.

5.2 Experimental Design

A prototype x-ray imaging system was utilized for the experiments in this study. The system employs an x-ray tube (UltraBright Microfocus Source, Oxford Instruments, Scotts Valley, California USA) with a molybdenum anode and beryllium output window. The tube provides an x-ray energy range from 20 to 60 kV and a tube power output range from 10 to 60 W. The focal spot diameter of the x-ray tube varies according to the power output. The measurements in this study were acquired at a tube potential of 40 kV, tube power of 20 W and exposure time of 20 s, which corresponds to a focal spot diameter of 20 μm.[186] The tube voltage, tube power and exposure time were controlled precisely by a software application interfacing directly with the source controller device. The source-to-image distance (SID) maintained in the study was 6 feet (1828.8 mm), and the object was placed in contact with the detector to avoid magnification effects. The images were acquired by the computed radiography detector system detailed in Section 3.1.2, which provides a pixel pitch of 43.75 μm. Mammography plates with dimensions of 18 by 24 cm were employed for this study. Linearization of the data was necessary to allow quantitative DQE

analysis, and was therefore performed according to a process presented previously.[70, 73, 76]

5.3 Error Analysis

The calculation of the photon fluence q involves multiplication of the radiation exposure X_d by the photon fluence per unit exposure $\frac{\Phi}{X}$, as defined below:[70, 73, 75, 102-103]

$$q = X_d \cdot \frac{\Phi}{X}. \tag{30}$$

As discussed in detail in Section 2.1.4, X_d is determined through direct measurements of the x-ray exposure, and $\frac{\Phi}{X}$ is calculated from direct acquisition of the x-ray spectrum. As an alternative to direct calculation, numerous studies[70, 76, 102, 182, 185, 187] have estimated the value of $\frac{\Phi}{X}$ according to the experimental settings, through the use of previously published methods.[106, 143, 145, 152, 154, 188-189] In addition, the International Electrotechnical Commission (IEC) published a standard method[99] for x-ray spectra estimation in determining the DQE, in an effort to facilitate the comparison of calculations performed at different laboratories. However, application of the estimations requires strict adherence to experimental settings, filtration and source-to-image distances (SID) defined in the standard, which presents a difficult challenge for evaluation of new techniques in a research environment. In addition, the use of an estimated value does not allow application of the error analysis process on which this study is based. The photon flux per unit exposure was therefore calculated

directly to allow comprehensive error analysis of the photon fluence. The total variance in the photon fluence calculation can be estimated by applying Eq. (19) to the formula for q from Eq. (30) as follows:

$$\sigma_q^2 = \sigma_{X_d}^2 \cdot \left(\frac{\partial q}{\partial X_d} \right)^2 + \sigma_{\frac{\Phi}{X}}^2 \cdot \left(\frac{\partial q}{\partial \frac{\Phi}{X}} \right)^2$$

$$= \left(\sigma_{\varepsilon X_d}^2 + \sigma_{\beta X_d}^2 \right) \cdot \left(\frac{\Phi}{X} \right)^2 + \left(\sigma_{\varepsilon \frac{\Phi}{X}}^2 + \sigma_{\beta \frac{\Phi}{X}}^2 \right) \cdot X_d^2, \qquad (31)$$

where the values for X_d and $\frac{\Phi}{X}$ represent the mean values of the exposure and photon fluence per unit exposure calculations, respectively, and the variance values $\sigma_{X_d}^2$ and $\sigma_{\frac{\Phi}{X}}^2$ represent the total error introduced by the corresponding measurements. As demonstrated in Eq. (16), the total error for each measurement includes both random and systematic error components, which are represented in the second half of the equation by the values of σ_ε^2 and σ_β^2, respectively. The error analysis of q must therefore consist of a thorough investigation of the separate random and systematic errors introduced by both the exposure and spectrum measurements. To the best of my knowledge, an in-depth error analysis of both measurements for determination of the error contribution to the DQE from q had not been presented previously.

5.3.1 Exposure Measurements

The entrance exposure level was measured with a calibrated ionization chamber (Radcal 10X9-180 ionization chamber, Radcal Corporation, Monrovia, California). The chamber must be placed directly in the center of the x-ray beam, in the absence of additional measurement or acquisition devices, in order to eliminate errors caused by x-ray backscatter. The specifications from the manufacturer[190] indicate that the chamber delivers exposure measurements with a four percent error rate. The chamber must be placed precisely in the same location at which the image acquisition is performed; however, achieving the exact detector location with the ion chamber presents a challenge due to the 22 mm chamber thickness.[190] Previous studies[70, 73, 76, 102] have therefore calibrated the exposure measurement to account for the difference in distances through the use of the inverse square law, which allows calculation of the actual exposure value X_d from the measured exposure value X_i, using the magnification factor M observed between the detector and the ion chamber:

$$X_d = \frac{X_i}{M^2}. \tag{32}$$

The total variance in the exposure calculation can be estimated through applying Eq. (19) to the equation for X_d as follows:

$$\sigma_{X_d}^2 = \sigma_{X_i}^2 \cdot \left(\frac{\partial X_d}{\partial X_i}\right)^2 + \sigma_M^2 \cdot \left(\frac{\partial X_d}{\partial M}\right)^2$$

$$= \left(\sigma_{\varepsilon X_i}^2 + \sigma_{\beta X_i}^2\right)\left(\frac{1}{M^2}\right)^2 + \left(\sigma_{\varepsilon M}^2 + \sigma_{\beta M}^2\right)\left(\frac{-2 \cdot X_i}{M^3}\right)^2 , \tag{33}$$

where the values for X_i and M represent the mean values of the exposure and magnification factor calculations, respectively, and the variance values $\sigma_{X_i}^2$ and σ_M^2 represent the total error introduced by the measurements. In addition, the total variance values have again been expanded in the second half of the equation to include the separate contributions for the random and systematic error components, σ_ε^2 and σ_β^2, respectively. The relative error in the exposure calculations can then be determined to facilitate direct comparison with the other error contributions. This is accomplished as demonstrated in Eq. (20):

$$S_{X_d} = \frac{\sigma_{X_d}}{\mu_{X_d}}, \tag{34}$$

where σ_{X_d} is the square root of the value calculated in Eq. (33), and μ_{X_d} is the mean value of numerous calculations of X_d using Eq. (32). The details of the measurements and corresponding calculations are provided below.

First, the measured exposure X_i was calculated as the mean of 40 ion chamber measurements at the specified experimental settings. The random error in X_i was estimated as the variance among the measurements, while the systematic error calculation was based on the accuracy specifications provided by the manufacturer. Due to the fact that the accuracy was expressed as a percentage, the standard deviation and thus the variance can be calculated through multiplication of the

accuracy by the mean value of the measurements,[126] as given in the following equation:

$$\sigma^2_{\beta_{X_i}} = \left(0.04 \cdot \mu_{X_i} \right)^2 . \quad (35)$$

The results of the measurements are provided in Table 2,[103] which includes the following values calculated for X_i: mean, random error, systematic error and relative error.

Value	μ_{X_i}	$\sigma^2_{\varepsilon_{X_i}}$	$\sigma^2_{\beta_{X_i}}$	S_{X_i}
X_i *(mR)*	19.80625	0.00131	0.62766	0.040041759

Table 2: Results of calculations of the measured exposure X_i.

Investigation of the error sources in the table reveals that the systematic error is responsible for 99.79% of the error, which is reinforced by the fact that the relative error is approximately equal to the precision of the ion chamber. Thus the majority of the error was introduced by the measurement device, and the use of a more accurate exposure measurement system could reduce the error within the measurements.

A secondary investigation in the exposure measurements involves determining the relationship between the number of exposure measurements and the random error, in an effort to provide a method for future studies to utilize in selecting the number of measurements to achieve a desired precision. This was accomplished through a graphical representation of the random error corresponding to a range of measurement counts, which is given in Figure 26.[103] The relationship demonstrated in

the figure follows intuition, as one would expect the random error to decrease as the number of measurements is increased. However, one might not have expected the difference in random error between a few measurements and 20 or more measurements. Comparison of these results to the literature strongly indicates the potential for error reduction, as the previous studies that acquired more than a single measurement calculated the mean of only 3,[68] 5,[191] or 10[73, 102] measurements. As demonstrated in the figure, the values used previously correspond to a large amount of error in the result. The relationship in Figure 26 thus provides the ability to select an appropriate number of measurements for a particular experiment, in an effort to balance the amount of time required to conduct the experiment with an acceptable amount of random error.

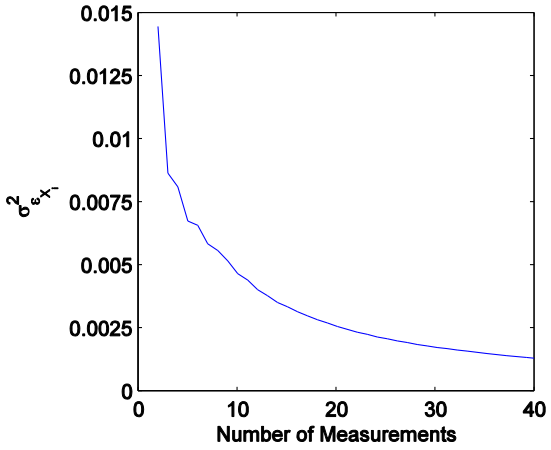

Figure 26: Illustration of the relationship between the number of exposure measurements acquired and the random error within the measurements.

The traditional method for calculation of *M* involves the measurement of the distances between the x-ray source and the ion chamber and between the x-ray source and the detector with a standard ruler. However, the lack of precision in standard

distance measurement devices can produce considerable error in the result. A new method was therefore developed in this study in an effort to minimize the error, which involves calculating the magnification factor from an x-ray image of the ion chamber. In this study, the magnification factor was calculated with both methods, and the amount of error corresponding to each calculation, as well as the error propagated into the exposure calculations, was determined for comparison purposes. The following sections detail the traditional method and the new method, which will hereafter be referred to as the ruler method and the image method, respectively.

Ruler Method

The x-ray configuration utilized in the ruler method is provided in Figure 27,[103] where *R1* is the distance between the x-ray source and the ion chamber and *R2* is the distance between the x-ray source and the detector. As detailed previously, *R2* is also known as the source-to-image distance (SID).

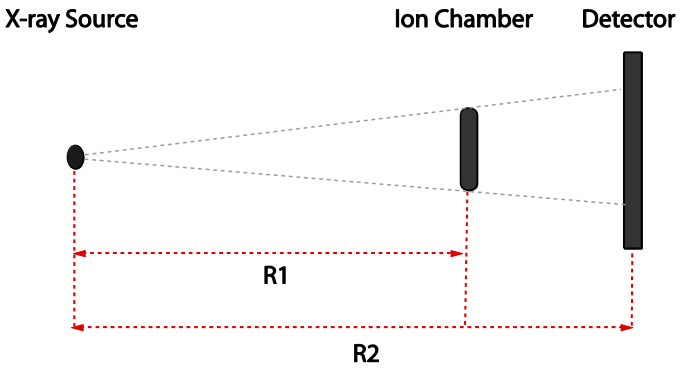

Figure 27: Illustration of the x-ray configuration utilized for calculation of the magnification factor by the ruler method.

The magnification factor in the ruler method, which will hereafter be denoted M_r, is then calculated through the use of similar triangles as follows:

$$M_r = \frac{R2}{R1}. \tag{36}$$

The distances of *R1* and *R2* were both calculated as the mean of five measurements with a standard ruler. The random error in each value was calculated as the variance among the measurements, and the systematic error was estimated as the precision of the ruler, which represents the standard deviation. The precision of the ruler was 1/16 of an inch (1.5875 mm). The results from the measurements are provided in Table 3.[103]

Value	μ	σ_ε^2	σ_β^2	*S*
R1(mm)	1645.60250	3.27620	2.52016	0.001463
R2(mm)	1825.62500	1.26008	2.52016	0.001065

Table 3: The results of the measurements of *R1* and *R2* with a standard ruler.

The variance formula for the calculation of M_r with the ruler method was calculated as follows:

$$\sigma_{M_r}^2 = \left(\sigma_{\varepsilon_{R1}}^2 + \sigma_{\beta_{R1}}^2\right)\left(\frac{-R2}{R1^2}\right)^2 + \left(\sigma_{\varepsilon_{R2}}^2 + \sigma_{\beta_{R2}}^2\right)\left(\frac{1}{R1}\right)^2. \tag{37}$$

The relative error was then calculated with the following equation:

$$S_{M_r} = \frac{\sigma_{M_r}}{\mu_{M_r}}. \tag{38}$$

The results of the magnification measurements with the ruler method are presented in Table 4.[103] For comparison purposes, the table also provides the results of the image method detailed in the next section, which is denoted M_i. The table provides the mean, total error and relative error calculated for both methods.

Value	μ	σ_M^2	S
M_r	1.10940	4.03033×10^{-6}	0.00181
M_i	1.10313	4.73792×10^{-7}	0.00062

Table 4: Comparison of the calculation of the magnification factors M_r and M_i determined by the ruler and image methods, respectively.

Image Method

The image method is a new method based on the calculation of the magnification factor from an x-ray image of the ion chamber, which was developed in this study in an effort to reduce the error contributed by the ruler method. Instead of performing measurements with a ruler, the new method calculates the magnification factor as the ratio of the magnified diameter of the ion chamber D_i, which is determined from an x-ray image of the chamber, to the actual diameter of the chamber D_a measured with a caliper. The resulting magnification factor is given in the following formula:

$$M_i = \frac{D_i}{D_a} = \frac{\Delta x \cdot L_i}{D_a}, \tag{39}$$

where Δx is the pixel pitch of the detector and L_i is the number of pixels representing the diameter of the chamber on the image. In this study, five images of the ion chamber were acquired at the specified experimental settings. The ion chamber and the detector were both located precisely in the same positions utilized for acquisition of the exposure measurements and images, respectively. Assuming the pixel pitch of the detection system is fixed, the random and systematic error contributed by Δx is negligible. The pixel pitch was therefore treated as a constant value in the calculations. It should also be noted that this method is facilitated by the shape of the

ion chamber, which does not have a constant diameter for the entire chamber thickness, but instead increases from a minimum diameter on the outer edges to a maximum in the middle of the chamber, coinciding with the location of the measuring mechanism. Thus the measurement of the diameter at the maximum value precisely correlates to the location at which the exposure measurement was acquired. However, if the ion chamber had consisted of a uniform diameter size, the method would be difficult to apply due to the difference in magnification values that would be produced by the diameters representing the front and back of the chamber.

For the calculation of L_i, the number of pixels representing the diameter in each image was precisely determined through the use of a software application, which provides an accuracy of one thousandth of a pixel. The mean of the five L_i values was calculated, and the random error was determined as the variance among the measurements. The systematic error was estimated as the precision provided by the software application, which represents the standard deviation as detailed previously. The mean value determined for L_i is provided in Table 5,[103] which also includes the random, systematic and relative errors. Next, D_a was determined as the mean value of five measurements of the ion chamber diameter obtained by the same person with a caliper (Digimatic Calipers 500-164-20, Mitutoyo America Corporation, Aurora, Illinois). The random error was calculated as the variance among the measurements, and the systematic error was estimated based on the precision of the caliper, which is 0.0254 mm. The results of the actual chamber diameter measurements are also provided in Table 5.

Value	μ	σ_{ε}^2	σ_{β}^2	S
L_i *(pixels)*	2972.97980	0.88548	1.91×10^{-15}	0.000317
D_a *(mm)*	117.90800	0.00337	0.00065	0.000537

Table 5: Results of the following image method calculations: the number of pixels representing the magnified ion chamber in the image (L_i), and the actual diameter of the chamber measured by a caliper (D_a).

The total variance in the calculation of the magnification factor with the image method is then determined as follows:

$$\sigma_{M_i}^2 = \left(\sigma_{\varepsilon_{L_i}}^2 + \sigma_{\beta_{L_i}}^2 \right) \left(\frac{\Delta x}{D_a} \right)^2 + \left(\sigma_{\varepsilon_{D_a}}^2 + \sigma_{\beta_{D_a}}^2 \right) \left(\frac{-\Delta x \cdot L_i}{D_a^2} \right)^2 , \tag{40}$$

where the mean, random error and systematic error values for L_i and D_a presented in Table 5 were utilized. Finally, the relative error within the calculation of M_i is determined through the following formula:

$$S_{M_i} = \frac{\sigma_{M_i}}{\mu_{M_i}} . \tag{41}$$

As detailed in the previous section, the results of the magnification measurements with the image method are presented in Table 3,[103] which also provides the results of the ruler method for comparison purposes.

Comparison of Magnification Methods

Investigation of the results in Table 3 reveals that the image method reduces the error by approximately 50% as compared to the ruler method, although the relative errors of the image and ruler method are both less than 1%. This can probably be attributed

to the large source-to-image distance (SID) of 1828.88 mm utilized in this study, which was almost double the typical clinical SID of approximately one meter.

The mean, variance and relative error propagated into the exposure calculations by the ruler and image methods were next calculated for comparison, and the results are provided in Table 6.[103] Once again, the small difference in error contributed by the methods is probably the result of the large SID. In addition, error differences between the methods are overshadowed by the fact that the X_i measurements accounted for 99.99% of the error in the calculations. As discussed in the previous section, the majority of the error was contributed by the ion chamber. Thus the use of a more accurate exposure system could more closely demonstrate the differences in error between the methods.

Method	X_i	$\sigma^2_{X_d}$	S_{X_d}
Ruler	16.09270258	0.41861	0.040205
Image	16.27604083	0.42515	0.040061

Table 6: Comparison of the exposure calculation results determined by the ruler and image methods.

To further investigate the effect of the SID on the error contributed by the magnification calculation, the relationship between the two values was next evaluated. A constant distance *d* between the ion chamber and detector was assumed, due to the relatively small separation between them. In addition, constant random and systematic errors were also assumed, regardless of the *R1* and *R2* values. The error

formula for the ruler method given in Eq. (37) was then solved to obtain the following formula dependent only on SID (*R2*):

$$\sigma^2_{M_r} = [(\sigma^2_{\varepsilon_{R1}} + \sigma^2_{\beta_{R1}}) \cdot R2^2] / (R2^2 - 2R2 \cdot d + d^2)^2$$

$$+ (\sigma^2_{\varepsilon_{R2}} + \sigma^2_{\beta_{R2}}) / (R2^2 - 2R2 \cdot d + d^2). \quad (42)$$

The total variance in the magnification calculation was then determined for a range of *R2* values from 500 to 2000 mm, which was selected to incorporate both clinical and research environments. The result was a graphical representation of the error in the magnification calculation based on the SID, which is given in Figure 28.[103]

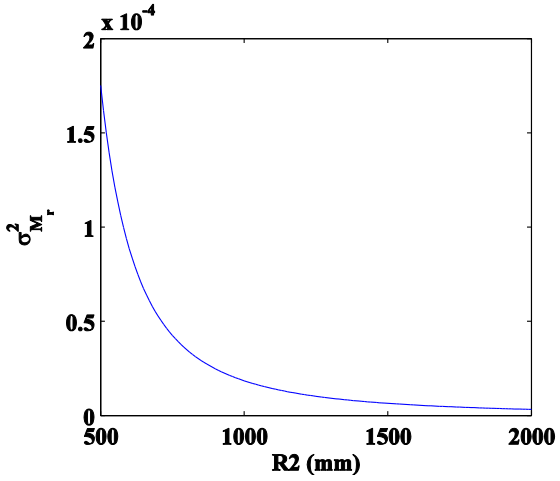

Figure 28: Illustration of the relationship between *R2*, which represents the SID, and the resulting variance in the magnification calculation by the ruler method.

As illustrated in the figure, the maximum error contributed by the ruler method corresponds to clinical *R2* values, decreasing to a minimal error contribution for the SID value utilized in this study. Therefore, if the study had been conducted with an *R2* value more closely representing a clinical environment, the corresponding error

amount would have more accurately indicated the amount of error contributed by the ruler method.

Investigation of the error formula for the image method in Eq. (40) reveals that the calculation is dependent only on the number of pixels and the diameter of the ion chamber, which are both constant. Thus the small error calculated by the image method in this study would remain constant regardless of the SID, and comparison of that error value to the error produced by the ruler method at a clinical SID value reveals a much larger difference between the two methods. These results are significant, not only because a new method was presented for calculation of the magnification factor with a greatly reduced error contribution, but also because the method is independent of the SID. The application of the new method therefore holds the potential to improve the accuracy of the calculations performed in a wide variety of applications.

5.3.2 Spectrum Measurements

For the photon fluence per unit exposure calculation and corresponding error estimation, the x-ray spectrum was directly measured through the use of an x-ray spectrometer with a 3 x 3 x 1 mm^3 Cadmium Telluride (CdTe) detector (Amptek Incorporated, Bedford, Massachusetts), using a pair of tungsten collimators provided by the manufacturer.[163] As detailed previously, the use of collimators limits the photon fluence to an acceptable level for the small surface area of the detector. The collimators, spectrometer and x-ray source were aligned through the procedure

developed for our research, which was detailed in Section 3.1.4. For the measurements, only the collimators and spectrometer were placed in the path of the x-ray beam to avoid errors introduced by x-ray backscatter. In this study, 40 spectrum measurements were acquired at the specified experimental settings. The spectrometer characterizes the x-ray spectrum by separating the detected x-ray photons into channels that are related linearly to the energy levels of the photons.[192] During acquisition, the spectrometer records the number of photons detected for each channel, and the output from the measurement consists of channel number and photon count pairs. Therefore, a process referred to as energy calibration must be performed on the raw data, in an effort to determine the linear relationship between the channel numbers and the x-ray energy values they represent. The calibration process typically involves the use of at least two pairs of known channel number/energy value relationships, which are determined through identifying the channel numbers corresponding to characteristic peaks within the x-ray beam, such as the material of the x-ray anode. Linear regression is then applied to determine the channel number/x-ray energy relationship based on the pairs. The error analysis detailed in this chapter does not include the errors introduced by the linear regression algorithm, as the corresponding theoretical error analysis is being derived as part of an ongoing study.[107]

Following the energy calibration process, the photon fluence per unit exposure must be calculated from the calibrated spectrum, which now consists of x-ray energy and

photon count pairs. The formula for this calculation was derived for our research,[107] and had not previously been reported to the best of my knowledge:

$$\frac{\Phi}{X} = \frac{5.4825\times10^{5}}{\sum_{E}\left(\frac{\mu_{en}}{\rho}\cdot\Phi_{N}(E)\cdot E\right)}\left[\,1\!\!\diagup\!\!(mm^{2}\cdot mR)\right], \tag{43}$$

where $\frac{\mu_{en}}{\rho}(cm^{2}/g)$ is the mass energy absorption coefficient of air, and Φ_N is the x-ray spectrum as a function of each energy *E(kV)* represented, which is normalized by the total photon count.

The photon fluence per unit exposure for each spectrum acquired was calculated with Eq. (43), and the mean among the measurements was determined. The random error was calculated as the variance among the measurements, and the systematic error was estimated as the precision of the spectrometer, which is specified by the manufacturer[163] as 0.77% for the tube potential utilized. The total error contributed by the photon fluence per unit exposure calculation is thus determined as follows:

$$\sigma^{2}_{\frac{\Phi}{X}} = \sigma^{2}_{\varepsilon_{\frac{\Phi}{X}}} + \left(0.0077\cdot\mu_{\frac{\Phi}{X}}\right)^{2}, \tag{44}$$

and the relative error can then be determined with the following formula:

$$S_{\frac{\Phi}{X}} = \frac{\sigma_{\frac{\Phi}{X}}}{\mu_{\frac{\Phi}{X}}}. \tag{45}$$

The results of the calculations for the photon fluence per unit exposure are provided in Table 7, which includes the mean, along with the random, systematic, total and relative error values.

Value	$\mu_{\frac{\Phi}{X}}$	$\sigma^2_{\varepsilon_{\frac{\Phi}{X}}}$	$\sigma^2_{\beta_{\frac{\Phi}{X}}}$	$S_{\frac{\Phi}{X}}$	$\sigma^2_{\frac{\Phi}{X}}$
$\frac{\Phi}{X}$	39391.825	30447.772	92001.234	0.009	122449.007

Table 7: Results of the calculations of the mean and variance values for the photon fluence per unit exposure.

The final investigation within the spectrum measurements involves determining the relationship between the number of measurements and the random error contributed to the result. The evaluation was applied similarly to the investigation of the exposure measurements in Section 5.3.1, and the goal was again to provide the ability for future studies to estimate the number of measurements required in order to achieve a desired error amount. The graphical illustration of the relationship between the number of spectrum measurements and the random error in the measurements is given in Figure 29.[103]

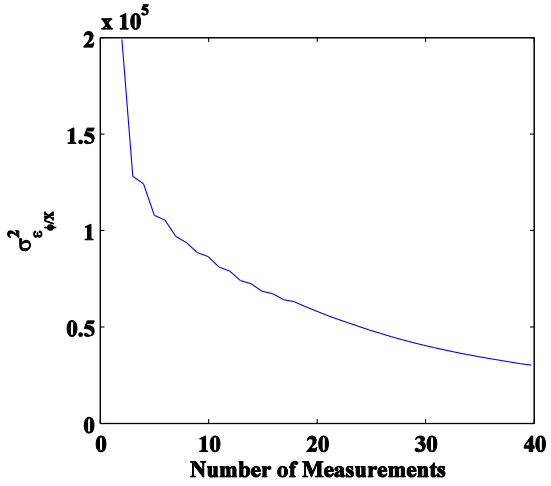

Figure 29: Illustration of the relationship between the number of spectrum measurements acquired and the random error within the measurements.

As expected, the error decreases as the number of measurements increases. However, similar to the results of the exposure measurements, the significance elucidated in the relationship is in the large difference in error between a few measurements and 20 or more measurements. This figure can therefore provide a helpful guide for future studies in selecting an appropriate number of measurements to attain an acceptable level of error. As a final demonstration of the amount of error reduction through increasing the number of measurements acquired, Figure 30[103] provides a comparison of an individual spectrum measurement with a mean spectrum from 40 measurements. The individual spectrum exhibits large fluctuations throughout the range, while the mean spectrum reveals the smoothing effects of averaging numerous measurements.

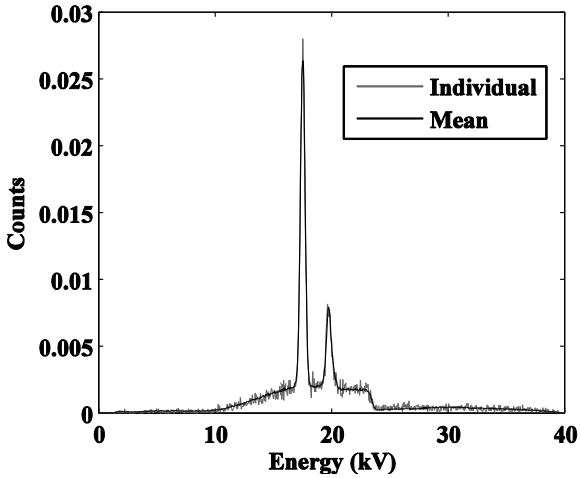

Figure 30: Comparison of an individual spectrum measurement (gray) with a mean spectrum from 40 measurements (black).

5.3.3 Photon Fluence

The next step in the investigation is determining the amount of error propagated into the calculation of the photon fluence from the exposure and spectrum measurements, which will be accomplished with the formula given in Eq. (31). The mean and variance values calculated in the previous two sections will be utilized, which are presented in Tables 6 and 7. Due to the similarity between the errors provided by the ruler and image methods, which was a result of the SID utilized in the experiments as discussed previously, the photon fluence was calculated with only the exposure value resulting from the image method. The relative error will also be calculated as follows:

$$S_q = \frac{\sigma_q}{\mu_q}. \tag{46}$$

The mean, total variance and relative error determined for the photon fluence are given in Table 8.[103]

Value	μ_q	σ_q^2	S_q
q(1/mm^2)	641142.9519	6.92150E+08	0.0410

Table 8: Photon fluence calculation results, including mean, total error and relative error, which were calculated with the exposure and spectrum measurement results.

Once again, the relative error in the photon fluence calculations is approximately 4%, which indicates the prevailing influence of the systematic error in the exposure measurements on the overall error. In addition, the relative error in the photon fluence calculation is deceptively low, which can probably be attributed to the precisely controlled experimental conditions enforced in this study. This includes the system alignment process, magnification factor calculation, and spectrum collimation procedure, all of which are difficult to apply in clinical environments. Thus the error amounts calculated on a clinical system with this procedure could provide much more insight into the principal error sources in the system. Also, as detailed previously, the significance in these results is not merely in the error amounts, but the ability to quantify and compare the amount of error contributed to a result by the individual factors in the calculation.

5.3.4 DQE

The final step in the error investigation is determining the error propagated into the DQE through the photon fluence calculation. The average value for *q* given in Table 8 will be utilized for the DQE calculation, along with calculations of the MTF, NPS and *S(0)* as detailed in Sections 2.1.2 and 2.1.4. The average value of several

calculations was utilized in an effort to minimize the error contribution. The resultant DQE is provided in Figure 31.[103]

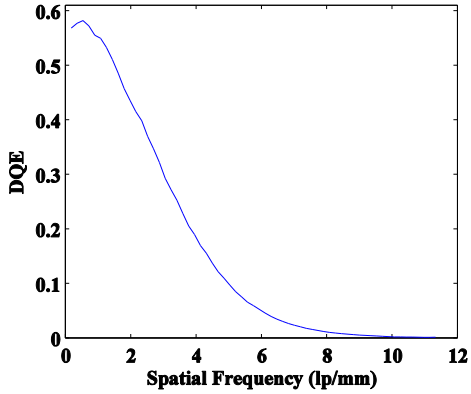

Figure 31: Detective quantum efficiency (DQE) determined with the mean photon fluence value calculated in this study.

Applying the error analysis method to the DQE formula given in Eq. (13) gives the following equation for calculation of the total error in the DQE:

$$\sigma^2_{DQE(f)} = \sigma^2_{S(0)} \cdot ((4 \cdot [DQE(f)]^2) / [S(0)]^2) + \sigma^2_{MTF(f)} \cdot ((4 \cdot [DQE(f)]^2) / [MTF(f)]^2) + \sigma^2_{NPS(f)} \cdot ([DQE(f)]^2 / [NPS(f)]^2) + \sigma^2_q \cdot ([DQE(f)]^2 / q^2). \quad (47)$$

The total error $\sigma^2_{DQE(f)}$ in the resultant DQE was not calculated for this study, as the goal of this study is primarily to investigate the photon fluence. The factor in Eq. (47) corresponding to the error contributed by the photon fluence can therefore be evaluated individually as follows:

$$\{\sigma^2_{DQE(f)}\}_q = \sigma^2_q \cdot ([DQE(f)]^2 / q^2). \quad (48)$$

The values for σ_q^2 and q from Table 8 were utilized for the calculation, as well as the DQE curve given in Figure 31. It should be noted that since the DQE is a function of spatial frequency, the error contributed to the DQE is also a function of spatial frequency. Thus the resulting curve in Figure 32[103] demonstrates the error contributed to the DQE by the photon fluence calculation for each frequency represented in the DQE.

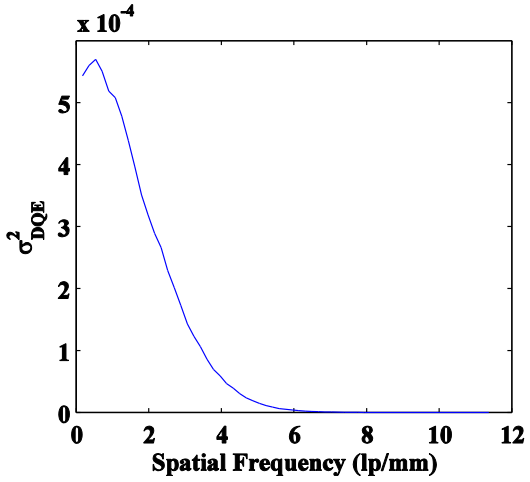

Figure 32: Illustration of the error contributed to the DQE by the photon fluence calculation for each frequency represented in the DQE.

In conclusion, this chapter has presented a quantitative method to determine the error contributing to a result by each of the components represented in the calculation. The effectiveness and usefulness of the method was demonstrated through determining the error contributed to the DQE by the photon fluence calculation. The factors on which to apply the error analysis were selected according to the prototype system and measurement devices, but different factors could be utilized in future calculations. In addition, the diminutive error calculated in this study is most likely a result of the

procedures implemented in the study to minimize the error, which are difficult to enforce in clinical environments. The application of this method to a study in the absence of those procedures would produce an error amount more representative of clinical systems. In that situation, the method would provide the ability to identify the principal error sources and offer important insight into error reduction. Thus the significant contribution in this study is the ability to calculate and compare the relative errors introduced by the individual factors contributing to a result.

In addition, a new magnification method was developed for this study in an effort to reduce the error introduced by the traditional use of rulers in the calculation. Although the error differences between the image and ruler methods were not significant in this study, the investigation revealed that this was due to the large SID utilized. The relationship between the SID and the random error was explored to reinforce this claim. For the ruler method, Figure 28 demonstrates the minimal error in the ruler method for the large SID value used in this study, as well as the large error for small SIDs such as clinical systems. However, the image method was determined to be independent of SID, indicating that the minimal value calculated in this study would be constant for smaller SID values. Therefore, the application of this method in clinical environments instead of the ruler method holds the potential to greatly reduce the error.

Finally, the relationship between the number of measurements and the random error within the measurements was investigated for both the exposure and spectrum

measurements. The results are illustrated in Figures 26 and 29, respectively, both of which indicate large error amounts resulting from averaging a few measurements, which has been done extensively in previous studies. The results also reveal that averaging 20 or more measurements can drastically reduce the error in the results. The relationships provided in the figures can be utilized as guidelines for future studies in selecting an adequate number of measurements to balance the measurement time and error produced in the results.

6 Effects of X-ray Beam Hardening on the DQE and Radiation Dose

6.1 Introduction

As detailed previously, the foundation of this dissertation research involves the difficult challenge faced by mammography in balancing the risk of harmful radiation dose to the patient and the benefit of disease detection provided by improved image quality. The focus of the study presented in this chapter was therefore to evaluate the feasibility of using a technique known as x-ray beam hardening to further optimize this tradeoff, which would greatly benefit mammography and other radiography fields. The investigation compared measurements of the DQE and the radiation dose corresponding to varying degrees of beam hardening, in an effort to evaluate the potential of beam hardening to reduce the radiation dose without negatively affecting the performance of the system. The technique of beam hardening will be presented in the following section. Radiation dose, as measured by calculation of the average glandular dose, was presented in Section 2.4. The theory, calculation and error analysis of the DQE has also been detailed thoroughly in previous chapters.

6.1.1 Beam Hardening

Beam hardening is the removal of low energy photons from the x-ray beam, through the use of filtration or other objects placed in the path of the beam.[20] As detailed previously, these photons are absorbed more readily due to the decreased ability to penetrate tissues. During an x-ray exposure, low energy photons are deposited within the patient. This not only increases the radiation dose, but also renders the photons

unable to reach the detector to contribute to the image quality. Therefore, removal of these photons prior to patient x-ray exposure holds the potential to reduce the dose without considerably decreasing the image quality. Clinical mammography systems currently utilize a small amount of beam hardening through filtration in an effort to remove low energy photons.[1, 20, 24] Due to the low characteristic peak values, the most common filter materials are Molybdenum (Mo) and Rhodium (Rh).[1, 20, 24] However, the use of additional beam hardening for further dose reduction has not been investigated previously, to the best of my knowledge. The potential of reducing the dose below current mammography levels without negatively affecting the detection ability is of clinical significance and thus the goal of the research presented in this chapter. The beam hardening investigation was a multi-faceted study consisting of a preliminary feasibility study as well as a comprehensive investigation, which are presented in the next two respective sections.

6.2 Preliminary Feasibility Study

The first stage of this investigation consisted of a preliminary feasibility investigation,[193] which involved separate comparisons of the DQE and the average glandular dose for a range of three beam hardening levels. The focus of this study was to evaluate the separate quantities to determine the relative effects of beam hardening, in an effort to determine the feasibility of maintaining the system performance and reducing the dose through the use of beam hardening.

6.2.1 Experimental Design

Beam Hardening

The beam hardening in the preliminary study was provided through the use of BR12 phantoms with three thicknesses: 0.5 cm, 1.0 cm and 2 cm. As detailed previously, BR12 phantoms were developed to simulate a 50% glandular, 50% adipose tissue composition,[194] and thus are used extensively for human tissue simulation and dose estimation purposes in clinical and research applications.[111]

System and Measurement Components

The prototype system detailed in Section 5.2 was utilized for this study, and the alignment procedure presented in Section 3.1.4 was also applied. Illustrations of the system configurations that were utilized in this study are provided in Figure 33(a) and (b).[193]

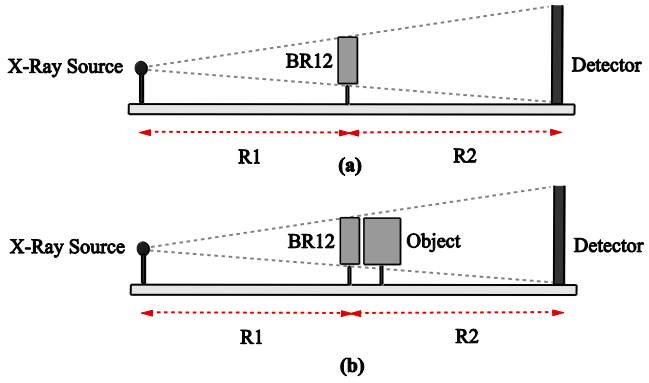

Figure 33: Illustrations of the x-ray configurations utilized in this study for: (a) measurement of the detective quantum efficiency, and (b) measurement of the average glandular dose.

In both configurations, the source-to-detector distance (SID or R1+R2) was 182.88 cm (6 feet), and the source-to-object distance (R1) was 91.44 cm (3 feet). An x-ray

energy of 40 kV was utilized for all measurements, and a typical clinical amount of filtration was provided by a 25 μm Rh filter.[20] The purpose of the object in the average glandular dose measurements in Figure 33 (b) was to simulate the human breast in a clinical mammography environment, in an effort to facilitate accurate dose estimation. This was accomplished by another BR12 phantom with a thickness of 5 cm.

DQE Measurements

The x-ray configuration given in Figure 33 (a) was utilized for four modes of measurements: the absence of added beam hardening, in which no BR12 filter was utilized, and beam hardening with the range of three BR12 filter thicknesses. The images and measurements were acquired at 40 kV and 20 W with an exposure time of 60 seconds. The DQE calculation was detailed thoroughly in Section 2.1.4 and Chapter 5. The formula was given in Eq. (13), but is repeated as follows for reference purposes:

$$DQE(f) = \frac{S(0)^2 \cdot MTF(f)^2}{NPS(f) \cdot q} = \frac{NEQ}{q}. \tag{49}$$

First, the MTF was calculated through acquiring one image for each mode of a 10 μm wide slit camera (Nuclear Associates, Carle Place, NY), placed directly in contact with the detector. The slit camera was placed approximately 2 degrees with respect to the detector pixel array, in order to obtain the non-aliased response by increasing the effective sampling rate.[52, 54, 56, 58] The MTF was then determined according to previous methods[54-58] by normalizing the absolute value of the LSF.[20] The NPS was

measured through acquisition of 20 noise-only images for each mode. The process detailed in Section 2.1.4 was then utilized to obtain the one-dimensional NPS. The large area signal *S(0)* was determined through calculating the mean pixel intensity of the 20 noise-only images within the region of interest utilized for calculation of the noise power spectrum. As detailed previously, the photon fluence *q* is determined through multiplication of the detector entrance exposure and the photon fluence per unit exposure, which can be calculated from a measured x-ray spectrum.

The measurements of detector entrance exposure level were obtained with a calibrated ionization chamber (10X9-180 ionization chamber, Model 9095 measurement system, Radcal Corporation, Monrovia, California). Results from the study presented in Chapter 5[103] indicated that utilizing the mean of numerous measurements reduces the error; therefore, 20 measurements at each mode were acquired. For these measurements, the ion chamber was placed in the corresponding location in Figure 33 (a) instead of the detector.

The x-ray spectrum was measured through the use of an x-ray spectrometer with a 3 x 3 x 1 mm^3 CdTe detector (Amptek Incorporated, Bedford, Massachusetts), using a pair of tungsten collimators provided by the manufacturer.[163] Twenty spectrum measurements at each mode were also acquired to reduce the error. A process presented previously[75-76, 106-107] and detailed in Chapter 5 was utilized to calculate the mean photon fluence per unit exposure from the spectrum measurements. The individual DQE curves corresponding to each of the beam hardening levels will be

compared in the results section, in order to investigate the effects of added beam hardening on the DQE.

Average Glandular Dose Measurements

The x-ray configuration given in Figure 33 (b) was utilized for average glandular dose calculations corresponding to each of the four modes of measurements. As detailed in Section 2.4.2, the calculation for D_g requires multiplication of the conversion factor D_{gN} and the entrance exposure X_{ESE} at the surface of the object.

The images and measurements were also acquired at 40 kV and 20 W. However, the exposure time was selected individually for each mode to provide a constant detector entrance exposure of 10 mR, in order to facilitate a comparison based on similar radiation exposure for image acquisition. The resulting exposure times were 162, 187, 208 and 247 seconds for BR12 filter thicknesses of 0, 0.5, 1 and 2 cm, respectively. Following the determination of the exposure times, the corresponding object entrance exposure X_{ESE} was then measured for each mode through the use of an ion chamber, as detailed in the previous section. For these measurements, the ion chamber was placed in the corresponding location in Figure 33 (b) instead of the object, and the detector was also removed to avoid errors introduced by x-ray backscatter. The mean value from five measurements for each mode was utilized. The D_{gN} values for each mode were estimated with Monte Carlo simulations through a process detailed in previous studies,[152-154] utilizing the x-ray spectrum corresponding to each of the modes and assuming 50% adipose and 50% glandular tissue composition.

6.2.2 Results

DQE

A comparison of the x-ray spectra without added beam hardening and with beam hardening by the range of BR12 filter thicknesses is provided in Figure 34,[193] which illustrates the result of the beam hardening in removing low energy photons from the x-ray beam. The MTF values calculated by each of the four modes are provided in Figure 35[193] for comparison. The similarity between the curves indicates the ability to maintain the frequency response of the system with increasing BR12 thickness.

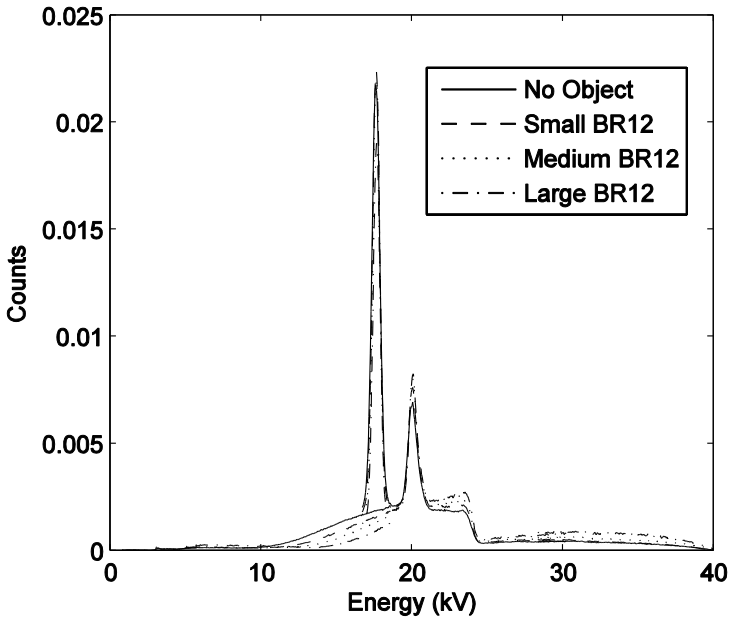

Figure 34: Comparison of the x-ray spectra for the four levels of beam hardening: no object, small BR12 (0.5 cm), medium BR12 (1 cm), and large BR12 (2 cm).

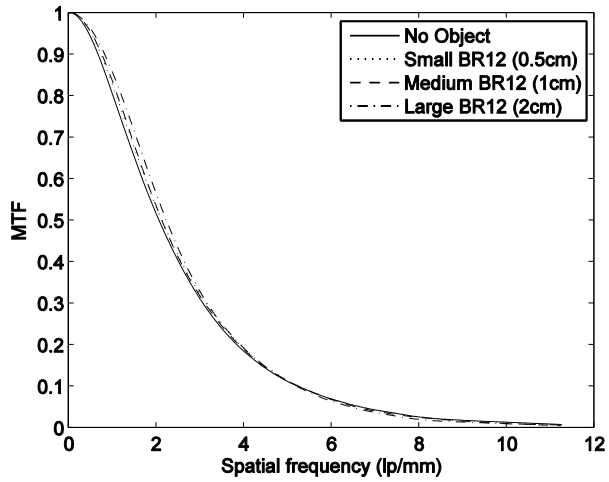

Figure 35: Comparison of the MTF values corresponding to the levels of beam hardening.

A comparison of the NPS curves calculated for each mode is provided in Figure 36,[193] which reveals differences among the curves for the range of beam hardening levels. As detailed previously, the noise in x-ray imaging is dependent on the amount of exposure; thus the variations in the NPS indicates the effect of detector entrance exposure variation on the noise processed by the system. This is evidenced further by the decrease in the *S(0)* values: 194.76, 134.60, 95.77 and 52.11, for BR12 filter thicknesses of 0, 0.5, 1 and 2 cm, respectively.

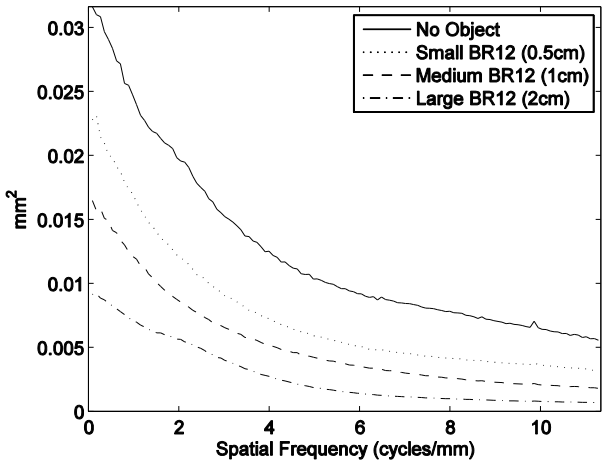

Figure 36: Comparison of the NPS values corresponding to the levels of beam hardening.

Finally, the comparison of the DQE values is given in Figure 37.[193] The four modes exhibit close correlation throughout the range, which is a preliminary indication that the performance of the imaging system may not be negatively affected by beam hardening.

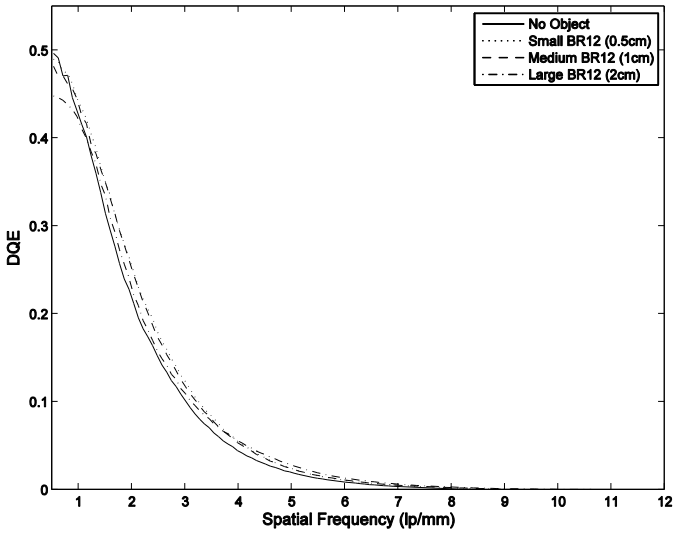

Figure 37: Comparison of the DQE values corresponding to the levels of beam hardening.

Average Glandular Dose

A comparison of the average glandular dose value calculated for each mode is provided in Table 9,[193] which provides the measured object entrance exposure and the corresponding range of D_{gN} values calculated from the Monte Carlo estimations. The two values were multiplied together as defined by Eq. (28) to obtain the average glandular dose value (D_g). The last column presents the percentage of dose reduction for each BR12 thickness, as compared to the dose value obtained without beam hardening. The table clearly demonstrates the potential of beam hardening to reduce the dose while maintaining the same detector entrance exposure. In fact, the D_g value

corresponding to the largest BR12 thickness demonstrates a dose reduction by more than half as compared to the value calculated without added beam hardening.

Beam Hardening (cm)	Object Exposure (R)	D_{gN} (mrad/R)	D_g (mrad)	Dose Reduction (%)
0	0.513	213.2	109.457	
0.5	0.391	232.2	90.855	16.99
1	0.299	245.2	73.320	33.01
2	0.179	263.6	47.274	56.81

Table 9: Comparison of the average glandular dose (D_g) measurements corresponding to the four levels of beam hardening in the preliminary study.

6.2.3 Discussion

The results provide a preliminary evaluation of the effects of beam hardening on the DQE and the average glandular dose. First, the dose reduction provided by the range of beam hardening levels was clearly indicated in Table 9. Secondly, the comparison of the DQE curves corresponding to the range of beam hardening levels demonstrated only small differences among them. Inspection of the quantities comprising the DQE indicates that these differences can largely be attributed to the differences among the NPS curves, which indicates the effect of detector entrance exposure variation on the noise processed by the system. The comprehensive study detailed in the following section will perform the DQE calculations corresponding to similar detector entrance exposures, which will not only alleviate this difference, but also provide the ability to correlate the DQE and dose calculations for determination of the corresponding effects of beam hardening.

6.3 Comprehensive Investigation

The next stage of the beam hardening investigation involved a comprehensive comparison of the effects of beam hardening on the DQE and average glandular dose. The focus of this investigation[195] was to investigate the potential of beam hardening to provide a dose reduction without negatively affecting the performance of the system in terms of quantum efficiency. In this study, the calculations for both quantities were acquired under the same experimental conditions to allow direct correlation of the results.

6.3.1 Experimental Design

Beam Hardening

The comprehensive study utilized the clinical beam hardening methods of Mo and Rh filtration instead of the BR12 phantoms, in an effort to more closely simulate the clinical environment. A range of five beam hardening levels was investigated, including two thicknesses each of Mo and Rh, along with a baseline level without adding beam hardening. The smaller thicknesses utilized for the filter types were the standard clinical system values of 25 µm Rh and 30 µm Mo.[20] These values were doubled to obtain the larger thicknesses for the filter types (50 µm Rh and 60 µm Mo), in an effort to investigate additional dose benefits as well as the ability to maintain the imaging performance with added beam hardening.

System and Measurement Components

The prototype system detailed in Section 5.2 was also utilized for this study, and the alignment procedure presented in Section 3.1.4 was again applied. The system configuration utilized for calculation of both the DQE and the average glandular dose is provided in Figure 38.

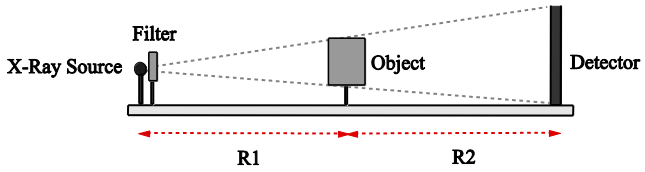

Figure 38: Illustration of the x-ray configuration utilized for the DQE and average glandular dose calculations in this study.

The values of R1 and R2 were both 91.44 cm (3 feet), which facilitates a source-to-detector distance (SID) of 182.88 cm (6 feet). An x-ray energy of 60 kV was utilized for all measurements. The purpose of the object was to simulate the human breast in a clinical mammography environment, in an effort to facilitate accurate measurements of the dose and system performance. This was again accomplished by a BR12 phantom with a thickness of 5 cm. For comparison purposes, a second set of measurements were performed without the object, in an effort to evaluate the effect of the object on the measurements. Therefore, a set of ten measurements were performed, which incorporated five levels of beam hardening in both the presence and the absence of the object. The exposure time for each filter/object combination was selected to provide a constant detector entrance exposure of 10 mR, in an effort to facilitate a comparison based on similar radiation exposure for image acquisition.

The exposure times corresponding to the range of filter and object combinations are provided in Table 10.

Object	Filtration	Exposure Time (s)
None	None	9
None	25 um Rh	13
None	50 um Rh	20
None	30 um Mo	12
None	60 um Mo	17
5 cm BR12	None	42
5 cm BR12	25 um Rh	91
5 cm BR12	50 um Rh	169
5 cm BR12	30 um Mo	89
5 cm BR12	60 um Mo	156

Table 10: Exposure times for the range of object/ filter combinations investigated in this study, which were selected individually to provide a constant detector entrance exposure of 10 mR.

Once the exposure time was determined for each filter/object combination, the corresponding object entrance exposure was measured for calculation of the average glandular dose. Due to the constant detector entrance exposure for all combinations, the differences among the DQE and dose values were a result of only the factors controlled by this study.

DQE Measurements

The calculations of the DQE were performed through the use of the same methods as in the preliminary study. However, measurements were acquired for the range of ten filter/object combinations detailed in the previous section. The x-ray energy of 60 kV and 20 W was utilized for all modes, and the exposure time for each mode is given in

Table 10. As detailed previously, the exposure times were selected for each filter/object combination in order to maintain a constant detector entrance exposure.

Average Glandular Dose Measurements

The calculations of D_g were also performed through the use of the same methods as in the preliminary study, although the measurements were acquired under the new experimental conditions, which were consistent with the DQE measurements in order to facilitate correlation of the results. As detailed previously, the D_{gN} simulations assume the presence of an object with 50% adipose and 50% glandular tissue composition in the path of the x-ray beam; thus the D_{gN} values were only calculated for the spectra acquired when the object was utilized. Therefore, the average glandular dose results consist of a comparison of the dose values corresponding to the five beam hardening levels in the presence of the BR12 object.

6.3.2 Results

DQE

Comparisons of the x-ray spectra acquired for each beam hardening level are given in Figure 39 (a) and (b), which correspond to the images acquired without an object and with the 5 cm BR12, respectively. The comparison without the object demonstrates the effects of beam hardening in removing low energy photons from the x-ray beam, while the comparison with the object illustrates the further hardening effects of the object on the x-ray beam.

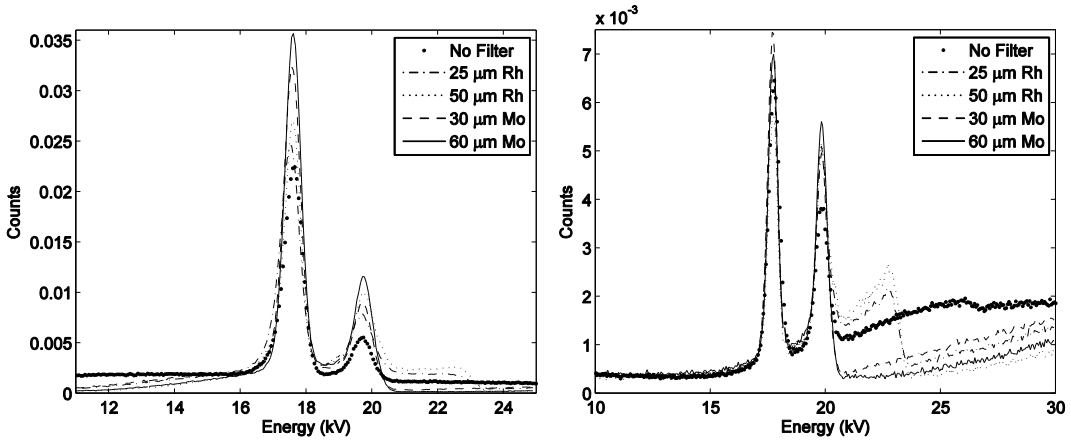

(a) **(b)**

Figure 39: Comparison of the x-ray spectra for the range of beam hardening levels. The spectra were acquired at 60 kV, 20 W (a) without an object in the path of the x-ray beam, and (b) with the 5 cm BR12 object in the path.

Comparisons of the MTF values calculated for each beam hardening level are given in Figure 40 (a) and (b), which correspond to the images acquired without an object and with the 5 cm BR12, respectively.

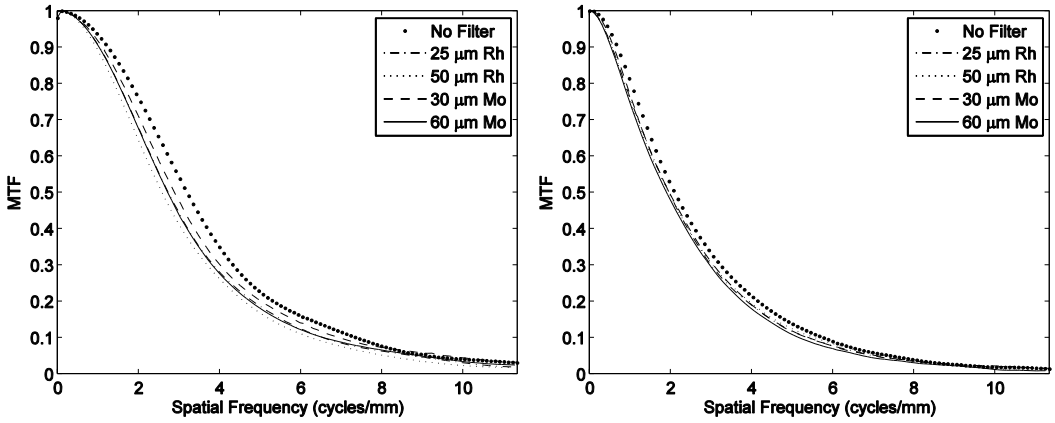

(a) **(b)**

Figure 40: Comparison of the MTF for the range of beam hardening levels (a) without an object in the path of the x-ray beam, and (b) with the 5 cm BR12 object in the path.

Next, comparisons of the NPS curves calculated for each beam hardening level are given in Figure 41 (a) and (b), which correspond to the images acquired without an

object and with the 5 cm BR12, respectively. Comparison to the differences among the NPS curves in the preliminary study reveals much higher correlation in this study, which is a result of the similar detector entrance exposure among the range of beam hardening levels.

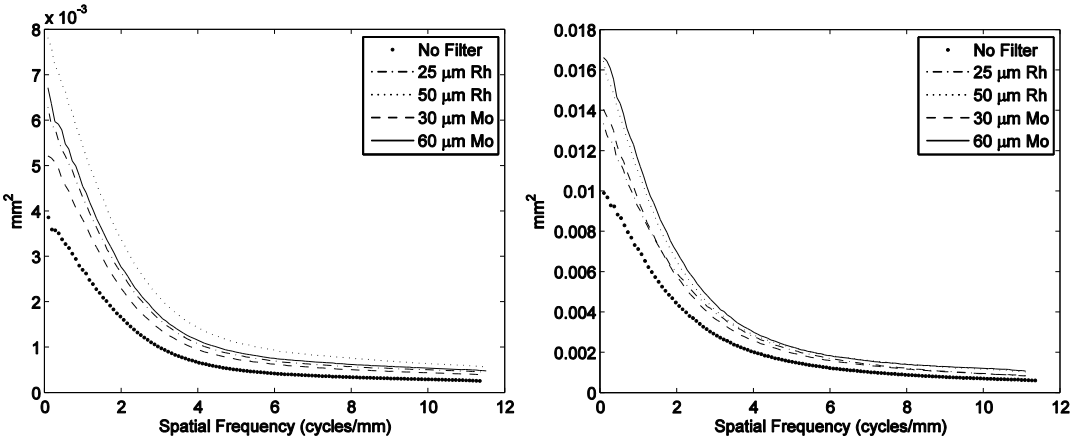

Figure 41: Comparison of the NPS for the range of beam hardening levels (a) without an object in the path of the x-ray beam, and (b) with the 5 cm BR12 object in the path.

Combining the MTF, NPS and *S(0)*, the NEQ comparisons of the beam hardening levels without an object and with the 5 cm BR12 are provided in Figure 42 (a) and (b), respectively.

In the MTF, NPS and NEQ comparisons without the object, the curve calculated without added beam hardening is noticeably different from the curves corresponding to the filters. However, when the 5 cm BR12 is utilized to simulate the human breast in mammography, the separation among the curves is much smaller, which is an encouraging indication that the use of filtration in a clinical environment may not negatively affect the imaging response of the system.

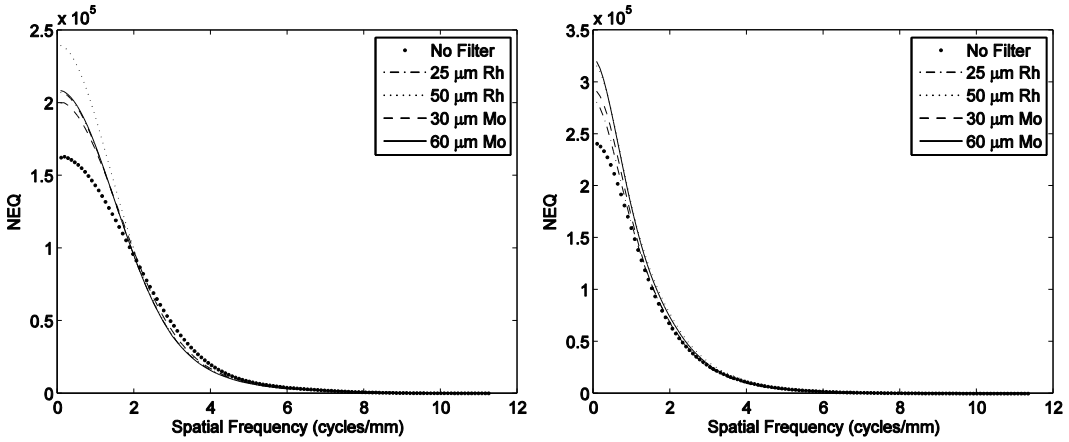

Figure 42: Comparison of the NEQ for the range of beam hardening levels (a) without an object in the path of the x-ray beam, and (b) with the 5 cm BR12 object in the path.

Next, comparisons of the *q* values corresponding to the ten object/filter combinations are given in Table 11.

Object	Filtration	Photon Fluence (1/mm2)
None	None	3.134×10^5
None	25 µm Rh	4.314×10^5
None	50 µm Rh	5.089×10^5
None	30 µm Mo	4.024×10^5
None	60 µm Mo	4.498×10^5
5cm BR12	None	7.087×10^5
5cm BR12	25 µm Rh	7.636×10^5
5cm BR12	50 µm Rh	8.288×10^5
5cm BR12	30 µm Mo	7.618×10^5
5cm BR12	60 µm Mo	8.243×10^5

Table 11: Comparison of the photon fluence (*q*) values for the ten object/filter combinations investigated in this study.

The results exhibit an increasing trend from the minimum value without added beam hardening to the maximum value with the 50 µm Rh filter. This follows intuition, as

the largest q value indicates the highest concentration of photons in the same surface area. Finally, comparisons of the DQE values for the beam hardening levels without an object and with the 5 cm BR12 are provided in Figure 43 (a) and (b), respectively. The results also exhibit much closer correlation between the curves acquired with the 5 cm BR12 than the curves generated without the object. Furthermore, the DQE curves corresponding to the object exhibit only a slight divergence, if any, among the results corresponding to the range of beam hardening levels.

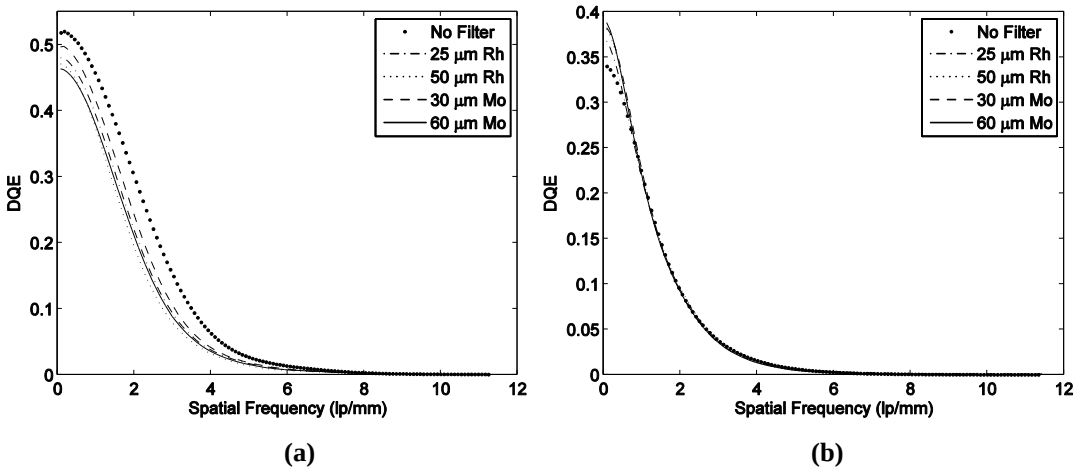

Figure 43: Comparison of the DQE for the range of beam hardening levels (a) without an object in the path of the x-ray beam, and (b) with the 5 cm BR12 object in the path.

Average Glandular Dose

Comparisons of the average glandular dose calculated for each filter with the 5 cm BR12 object are given in Table 13, which provides the measured object entrance exposure and the corresponding range of D_{gN} values calculated from the Monte Carlo estimations. Inspection of the D_{gN} coefficients reveals that the results correlate with the q values presented in the previous section, through demonstrating an increasing trend from the minimum value without added beam hardening to the maximum value

with the 50 µm Rh filter, which also produced the largest q value. Again, this follows intuition, as the largest q and dose coefficients both indicate the highest concentration of photons in the same surface area. The two values were multiplied together as defined by Eq. (28) to obtain the average glandular dose value (D_g). The last column presents the percentage of dose reduction for each filter, as compared to the dose value obtained without filtration. The results demonstrate a notable dose reduction of approximately 15% to 24% for the range of beam hardening levels. The filter corresponding to the maximum dose reduction was the 50 µm Rh filter. It is also interesting to note that the filter providing the second largest dose reduction was the 25 µm Rh filter, which provided a lower dose than both Mo filters.

Filtration	**Object Exposure (R)**	**D_{gN} (mrad/R)**	**D_g (mrad)**	**Dose Reduction (%)**
None	0.81	333.4	268.69	
25 µm Rh	0.61	343.8	210.02	21.84
50 µm Rh	0.56	366.6	203.82	24.14
30 µm Mo	0.68	337.0	229.17	14.71
60 µm Mo	0.63	356.0	222.86	17.06

Table 12: Comparison of the average glandular dose (D_g) measurements corresponding to the five levels of beam hardening in the comprehensive study.

6.3.3 Conclusion

In this comprehensive study, the results of the dose and DQE comparisons indicate that the use of beam hardening holds the potential to reduce the dose without decreasing the performance of the system in terms of quantum efficiency, which would benefit the fields of diagnostic x-ray imaging, especially mammography.

First, the results of the average glandular dose calculations demonstrated a reduction of 15% to 24% for the range of beam hardening levels utilized, as compared to the dose calculated without added beam hardening. Next, the DQE results exhibited almost complete correlation between the results obtained without added beam hardening to the results corresponding to the range of beam hardening levels. A comparison of the quantities comprising the DQE was also provided, which included the MTF, NPS, NEQ and q. The comparisons of all quantities demonstrate that the performance of the system was not significantly affected by the use of beam hardening. In addition, the measurements acquired with an object in the path of the x-ray beam exhibit much smaller differences than the measurements acquired without an object. Therefore, applications such as clinical environments where an object is utilized could obtain system performance comparable to current levels with the use of added beam hardening.

Subsequent studies will further evaluate the feasibility of beam hardening through comparisons encompassing a range of diagnostic energies, including current clinical mammography values. In addition, a comprehensive image quality evaluation will be performed, in an effort to investigate the potential of beam hardening to balance the tradeoff between dose and image quality.

7 Preliminary Feasibility of a High Energy Phase Contrast System Prototype

7.1 Introduction

The focus of the research presented in the remaining two chapters comprises a thorough investigation of the potential of applying higher x-ray energies to the field of mammography through the use of phase contrast imaging, which holds the potential not only to improve the image quality for earlier detection of disease, but also to reduce the risk of harmful radiation to the patient. In addition to the dose benefits of increasing the x-ray energy, this research also has the potential to overcome the existing challenge in phase contrast imaging involving the decreased number of output quanta generated with the x-ray source, which was detailed in Section 2.3.3. As described in that section, the exposure time must be increased in low energy phase contrast imaging to compensate for the lower output fluence, which hinders the clinical feasibility due to prolonged exposure times. Instead, the research in this dissertation proposes raising the x-ray energy, which maintains a clinically acceptable exposure time.

The primary goal of the research study[196] presented in this chapter was to evaluate the feasibility of high energy phase contrast imaging to provide adequate image quality for detection and diagnosis. Secondly, the study was also focused on evaluating the high energy operation of the phase contrast imaging system for a range of x-ray energies and magnification factors. These goals were accomplished through an image

quality evaluation incorporating numerous phantoms. The design and implementation of the research are presented in the following sections.

7.2 Experimental Design

7.2.1 Joint Parameter Optimization

The x-ray energies of 100, 120 and 140 kV were investigated in an attempt to determine the x-ray energy providing the optimal image quality within a range of high energies. The magnification factor (*M*) must also be optimized, as it represents a tradeoff between the phase contrast effect and the image quality. The value must be large enough for the phase contrast effect to provide a noticeable improvement to the image quality, but if it is too large, the spatial coherence can no longer be maintained and the phase contrast effect spreads across the entire image instead of only enhancing the edges.[21, 34] Numerous studies[29, 31, 34, 38, 45] have indicated approximately 2 as an optimal value for low energy phase contrast imaging. Therefore, 2 was utilized as the starting point, and the investigation evaluated the magnification factors of 2, 2.5 and 3, in an effort to determine the optimal factor for high energy phase contrast imaging. The study performed a joint optimization of the x-ray energy and magnification factor through a detailed comparison of the image quality provided by the resulting range of nine x-ray energies and magnification factor combinations. The object entrance exposure was held constant for all combinations, in order to provide an estimation of similar dose among the images for comparison purposes.

7.2.2 System and Measurement Components

Prototype System

The prototype system detailed in Section 3.1.1 was utilized for this study, and the alignment procedure presented in Section 3.1.4 was applied. An illustration of the system configuration that was utilized in this study is provided in Figure 44.

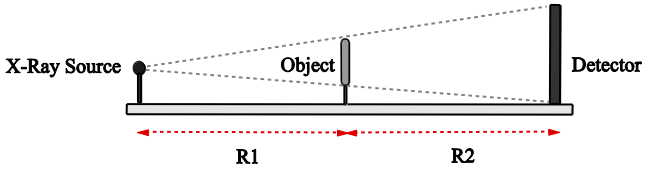

Figure 44: The high energy phase contrast x-ray imaging system configuration utilized in this study.

The source-to-detector distance (*R1*+*R2*) was held constant at 182.88 cm for all configurations, and the source-to-object distance (*R1*) was adjusted to provide magnification factors of 2 (91.44 cm), 2.5 (73.15 cm) and 3 (60.96 cm), according to the formula for *M* given in Eq. (26).

Image Detection System

The images were acquired by the computed radiography detector system detailed in Section 3.1.2, which provides a pixel pitch of 43.75 μm. Mammography plates with dimensions of 24 by 30 cm were employed for all images. A challenge in this study involves the utilization of mammography plates for much higher energies than designed, which lowers the quantum efficiency. However, the use of general radiography (GR) plates would result in lower spatial resolution, as the system only provides a pixel pitch of 87.5 μm for GR plates. The resulting tradeoff in the type of plate utilized will be an interesting topic evaluated in a future study.

Exposure Measurements

The measurements of object entrance exposure were obtained with a calibrated ionization chamber (10X9-180 ionization chamber, Model 9095 measurement system, Radcal Corporation, Monrovia, California). Five measurements at each mode were acquired in an effort to reduce the error in the measurements. The entrance exposure at exactly the same location as the object were measured for the nine kV/*M* combinations corresponding to the three x-ray energies and three magnification factors. Due to the differences in x-ray energies and *R1* distances for each kV/*M* combination, the exposure times were determined individually in order to provide similar object entrance exposures. To accomplish this, a target exposure amount of 1 R was utilized, and the exposure time resulting in the closest value was selected for each combination. The exposure times corresponding to the range of kV/*M* combinations are provided in Table 13.

X-ray Energy (kV)	Magnification	Exposure Time (s)
100	2	167
100	2.5	109
100	3	80
120	2	172
120	2.5	114
120	3	82
140	2	180
140	2.5	119
140	3	88

Table 13: Exposure times for the range of kV and *M* combinations investigated, which were selected individually to maintain a constant object entrance exposure of 1 R.

7.2.3 Phantoms

Several phantoms were utilized in this study to provide a comprehensive image quality evaluation. First, as detailed previously, the evaluation of system performance based on standard mammography quality control procedures, including the Academic College of Radiology (ACR) phantom, has been established as a widely-accepted quantitative comparison method.[21, 34, 36, 38] Thus, a standard 4.4 cm thick ACR phantom (Model K-598, Nuclear Associates, Carle Place, New York, USA) was employed in this study. Images were acquired of the 7 mm wax insert alone, as well as the full ACR phantom, for a few reasons. The primary reasoning was to investigate the performance of the high energy phase contrast system for images acquired under two conditions: high scatter level resulting from the full ACR phantom, and low scatter level from only the wax insert. Another motivation for imaging the wax insert alone involved providing increased subject contrast for comparison purposes. To analyze both sets of images, observer studies consisting of 10 independent observers were conducted. Each image was scored according to the number of distinguishable test objects, as outlined in the mammography quality control manual,[91] which separates the ACR test objects into groups of fibers, specks and masses, due to the corresponding application of each group to mammography detailed previously. Following these guidelines, separate scores were determined for each of the groups, and the scores were added together to achieve the overall image score, which provides a quantitative comparison of the relative image quality provided by the kV/*M* combinations.

Next, a contrast-detail (CD) phantom was utilized to provide an additional level of comparison among the kV/*M* combinations. Also detailed previously, contrast-detail analysis has been widely accepted as a simple and effective method for comparison of medical imaging systems or techniques.[44, 77-81] Contrast-detail phantoms typically consist of a matrix of circles with varying diameters along one axis to represent object size, and varying thicknesses along the other axis to produce contrast within the image.[20, 39] The 1 cm thick CD phantom used in this study (Model 083, CIRS, Norfolk, Virginia, USA) consists of seven rows ranging in diameter from 1.5 to 4.5 mm, and seven columns ranging in thickness from 0.25 to 4.5 mm. The analysis involves an observer identifying the minimum perceptible thickness in the image for each diameter. The results are compiled into a contrast-detail curve indicating the contrast required to distinguish an object as a function of the object size, which illustrates the resolving power of the system or technique. Thus curves for different systems or techniques can easily be compared, as a system exhibiting higher performance produces a contrast-detail curve located closer to the x-y axis.

A 1.5 mm thick acrylic edge phantom was also employed to illustrate the overshooting effects provided as the result of the edge enhancement in phase-contrast images.[21, 23, 25-26, 31, 38] Acrylic edge phantom images not only provide a visual indication of the edge enhancement, but they can also be utilized to determine edge profiles that serve as a graphical indication of the edge enhancement.[21, 28, 38] An edge profile illustrates the intensity values along a line perpendicular to the edge, which indicates the edge enhancement in the phase contrast images through an overshooting

effect along the edge transition. The edge profiles for the range of kV/*M* combinations will be compared for determination of the optimal phase contrast effect.

Finally, significant research focus has also been dedicated to the image quality provided by phase contrast with breast specimens[22, 30, 35-36] for qualitative investigation of the clinical potential of a system or technique. However, due to the difficulty of utilizing human specimens in research environments, phantoms are typically utilized to simulate human tissue. In this study, a new phantom providing tissue-equivalent x-ray images was utilized. The Mammography BR3D phantom (Model 020, CIRS, Norfolk, Virginia, USA) was fabricated from materials simulating 100% adipose and glandular tissues blended together in an approximate 50/50 ratio by weight, which produces a tissue-equivalent heterogeneous background on an x-ray image.[197] The phantom consists of a set of five pieces of the same shape, each having a thickness of 10 mm and a different blend of the materials. The combination of the five layers was designed to produce realistic tissue-equivalent x-ray images, and the 5 cm thickness provides an additional level of comparison involving the object thickness, the importance of which to mammography has been detailed previously. In addition, one of the layers also facilitates a quantitative test through incorporating ACR test objects. The phantom was designed for conventional mode imaging at mammography energies, thus the structures may not be distinguishable on the high energy phase contrast image. However, the ability to provide both a qualitative and quantitative comparison through the use of the tissue-equivalent phantom is extremely beneficial for research and clinical purposes.

7.3 Results

The principal goals of this study involved the investigation of the feasibility of high energy phase contrast images to provide adequate image quality for detection and diagnosis, and the optimization of both the x-ray energy and the magnification factor of the high energy phase contrast system. Five different phantoms were utilized to provide a thorough evaluation of the nine kV/*M* combinations for phase contrast imaging. Therefore, the study resulted in the acquisition of a large number of images that, for the purposes of brevity, will not all be provided. Two types of comparisons among the kV/*M* combinations exist: the range of x-ray energies for a specific magnification factor, and the range of magnification factors for a specific x-ray energy. However, only one of the comparisons will be provided for each phantom. To facilitate a comprehensive analysis, the comparison will be varied for each phantom in an effort to include the full range of magnification factors and x-ray energies.

7.3.1 Wax Insert of ACR Phantom

The ACR wax insert comparison, which is provided in Figure 45, demonstrates the images acquired with a magnification factor of 2.5 and x-ray energies of (a) 100 kV, (b) 120 kV, and (c) 140 kV. The images clearly demonstrate the feasibility of high energy phase contrast imaging to provide adequate image quality under low scatter level conditions, as only a few test objects are not clearly distinguished across the range of x-ray energies. A slight difference among the images can be determined in the comparison, as the images in (a) and (b) demonstrate very similar image quality, while the image in (c) provides slightly lower quality.

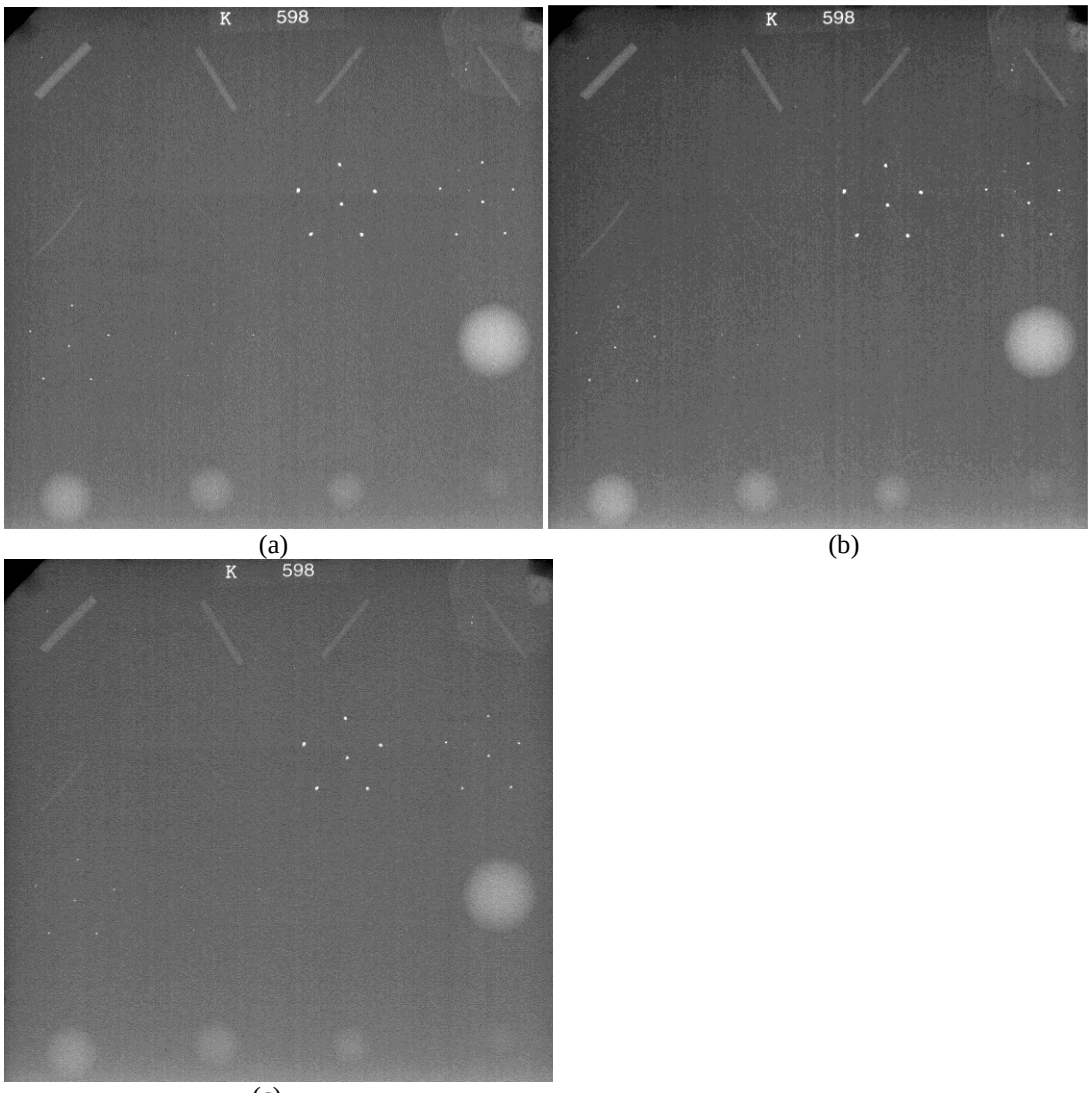

(a) (b)

(c)

Figure 45: Comparison of ACR wax insert phantom images, which were acquired at a magnification factor of 2.5 and an x-ray energy of (a) 100 kV, (b) 120 kV, and (c) 140 kV.

The results of the wax insert ACR observer study are provided in Table 14. The highest scores are demonstrated by the x-ray energies of 100 and 120 kV and the magnification factors of 2 and 2.5, although the lower scores corresponding to the x-ray energy of 140 kV and the magnification factor of 3 also provide adequate image quality. The variance among the scores is relatively low, but the highest scores correspond to the 100 kV, $M = 2$ and 120 kV, $M = 2$ combinations.

X-ray Energy (kV)	Magnification	Fibers	Specks	Masses	Total
100	2	6	4.35	4.4	14.75
100	2.5	4.95	3.7	3.95	12.6
100	3	5.6	4.2	3.9	13.7
120	2	5.8	4	4.35	14.15
120	2.5	5.7	4.2	4	13.9
120	3	5.55	3.95	3.9	13.4
140	2	5.7	3.9	3.75	13.35
140	2.5	4.8	3.6	3.7	12.1
140	3	5.6	4.2	3.8	13.6

Table 14: Comparison of wax insert ACR scores from the observer study of the images corresponding to the range of x-ray energy/magnification factor combinations investigated.

7.3.2 Full ACR Phantom

The full ACR phantom images are presented in Figure 46, which compares images acquired at an x-ray energy of 100 kV with magnification factors of (a) 2.0, (b) 2.5, and (c) 3.0. The images clearly demonstrate the feasibility of high energy phase contrast to provide adequate image quality under high scatter level conditions, due to the ability to distinguish several test objects for each type. In addition, only a slight difference among the images can be determined across the range of magnification factors.

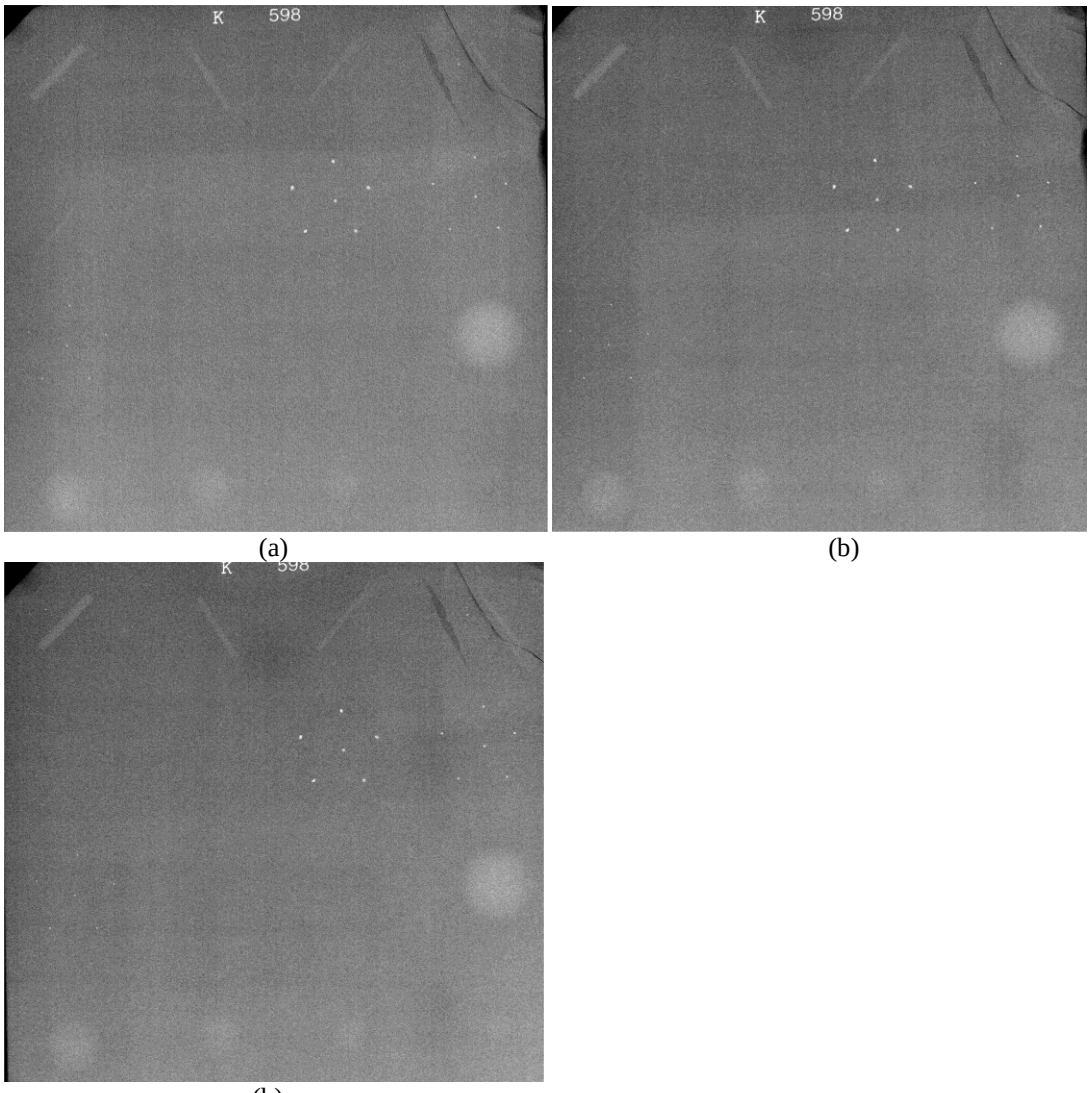

Figure 46: Comparison of full ACR phantom images, which were acquired at an x-ray energy of 100 kV and a magnification factor of (a) 2.0, (b) 2.5, and (c) 3.0.

This is reinforced by the results of the observer study in Table 15, which do not identify an optimal x-ray energy or magnification value, as the overall scores among the nine combinations differ by less than one point. As expected, the scores are lower than the wax insert only scores. However, the scores remain well within the acceptable image quality range. The ability to deliver high scores for the full clinical mammography phantom images corresponding to the range of kV and *M*

combinations, along with the small divergence among them, are encouraging indications of the ability of high energy phase contrast imaging to maintain acceptable image quality for detection and diagnosis.

X-ray Energy (kV)	Magnification	Fibers	Specks	Masses	Total
100	2	5.25	3.75	4.17	**13.17**
100	2.5	5.25	3.83	4.25	**13.33**
100	3	5.20	3.75	4.25	**13.20**
120	2	5.50	4	4.5	**14.0**
120	2.5	5.25	4	4.25	**13.50**
120	3	5.25	4	4.25	**13.50**
140	2	5.25	3.83	4.25	**13.33**
140	2.5	5.25	3.75	4.17	**13.17**
140	3	5.33	4	4.33	**13.66**

Table 15: Comparison of full ACR scores from the observer study of the images corresponding to the range of x-ray energy/magnification factor combinations investigated.

7.3.3 Contrast-Detail Phantom

The phase contrast comparisons of the contrast-detail phantom in Figure 47 provide images acquired at an x-ray energy of 120 kV with magnification factors of (a) 2.0, (b) 2.5, and (c) 3.0. The ability to distinguish numerous test objects in each image indicates the potential of high energy phase contrast imaging to provide acceptable image quality. In addition, the edge enhancement delivered by phase contrast imaging is clearly demonstrated through the white circles highlighting the edges of the test objects. The contrast-detail curves were generated according to the procedures detailed previously, and Figure 48 provides a comparison of the complete range of magnification factors and x-ray energies. As evidenced by the superposition of most

of the curves in the figure, the range of kV/*M* combinations exhibits similar image quality, with the curve corresponding to the 120 kV, *M* = 2.0 combination demonstrating slightly improved quality.

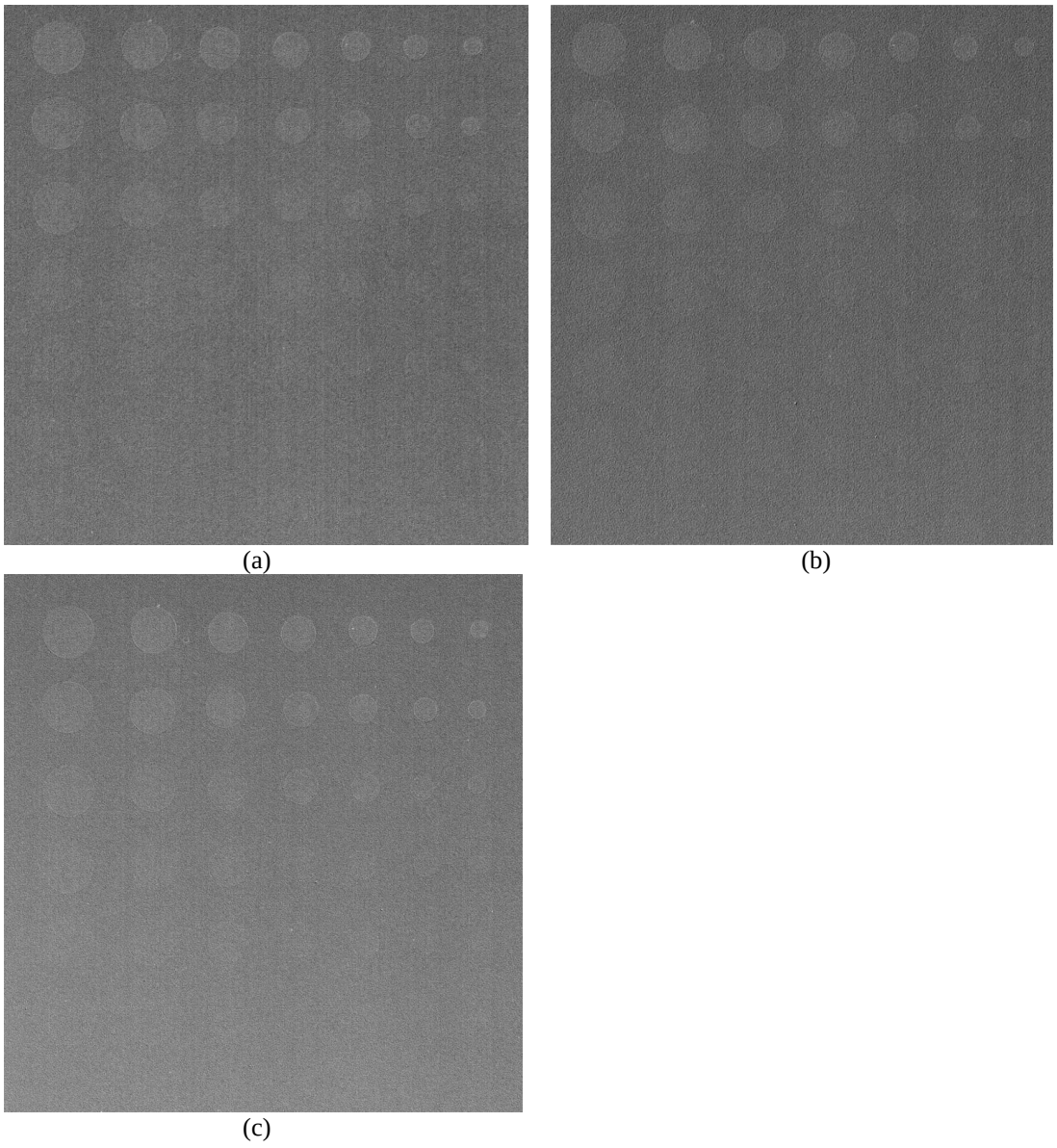

Figure 47: Comparison of contrast-detail phantom images, which were acquired at an x-ray energy of 120 kV and a magnification factor of (a) 2.0, (b) 2.5, and (c) 3.0.

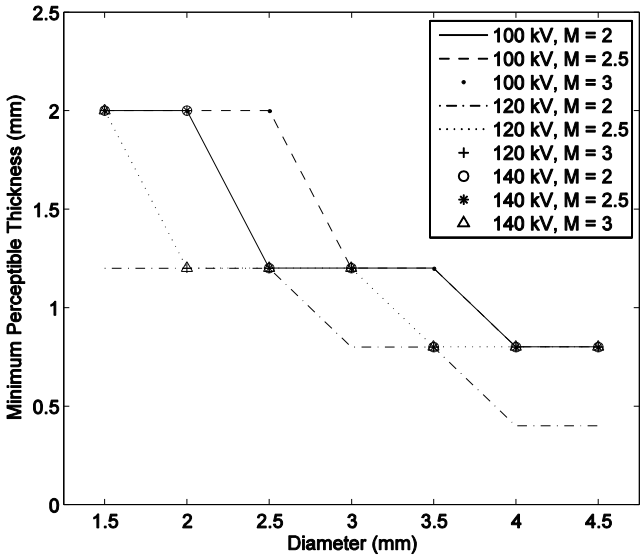

Figure 48: Comparison of contrast-detail curves generated from the phase contrast images corresponding to the range of x-ray energy/magnification factor combinations.

7.3.4 Acrylic Edge Phantom

The acrylic edge comparison in Figure 49 provides the phase contrast images acquired with a magnification factor of 3.0 and x-ray energies of (a) 100 kV, (b) 120 kV, and (c) 140 kV. The phase contrast edge effect is clearly demonstrated in the highlighting of the edge in all of the images. Note especially the combination of the dark highlighted line and the white line immediately below, which is an indication of the overshooting effect occurring as a result of phase contrast imaging.

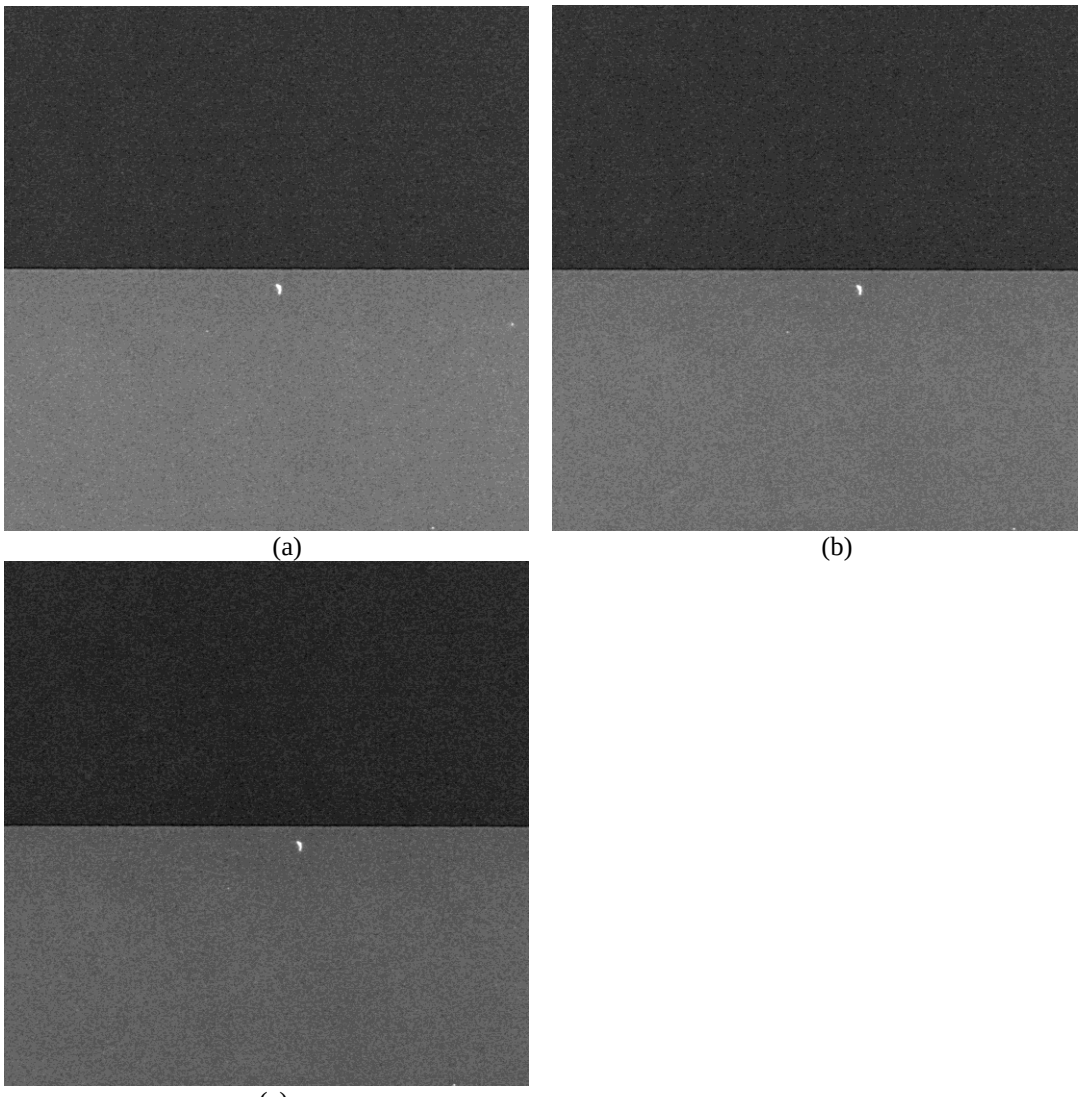

(a) (b)

(c)

Figure 49: Comparison of acrylic edge phantom images, which were acquired at a magnification factor of 3.0 and an x-ray energy of (a) 100 kV, (b) 120 kV, and (c) 140 kV.

To provide a point of reference, Figure 50[94] provides a comparison between a phase contrast and a conventional image of the acrylic edge phantom, which were presented in a preliminary study[94] comparing phase contrast images at 60 kV, 20 W, 10 s with conventional images at 20 kV, 20 W, 114 s. The difference between the ability to clearly distinguish the edges demonstrates the phase contrast effect in comparison to conventional imaging.

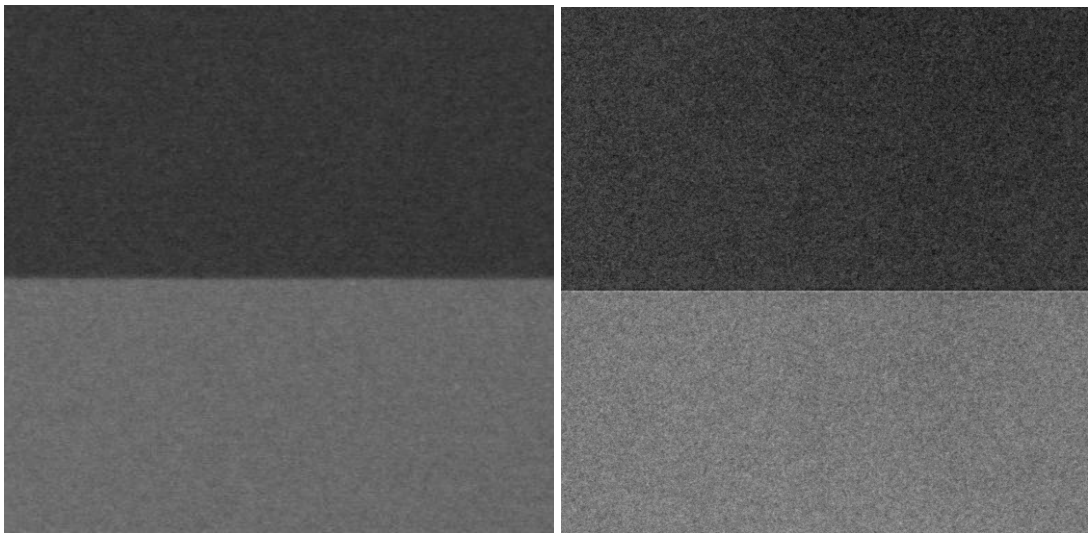

Figure 50: Comparison of acrylic edge images acquired at the following experimental settings providing similar entrance exposures: (left) conventional mode at 20 KV, 20W, 114s, and (right) phase contrast mode at 60 KV, 20 W, 10s.

As detailed previously, edge profiles are typically utilized to provide a second demonstration of phase contrast imaging, as they graphically exhibit the phase contrast effect in the amount of overshooting across the edge transition. Once again, a point of reference is provided in Figure 51,[94] which compares the edge profiles corresponding to the conventional and phase contrast images provided in Figure 50. The figure clearly indicates the overshooting resulting from the phase contrast effect, as well as the lack of overshooting in the conventional image. The difference between the edge profiles illustrates the effect that produced the substantial improvement in the quality of the phase contrast image in Figure 50, as compared to the conventional image.

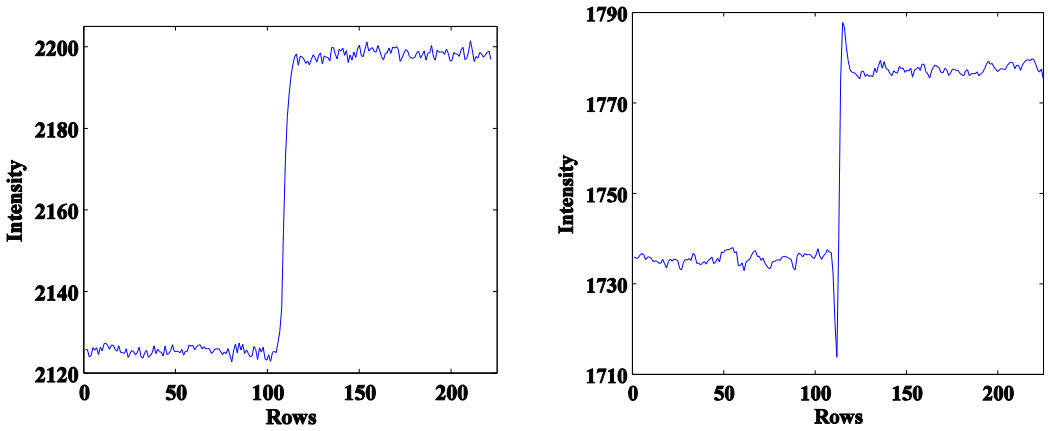

Figure 51: Edge profiles determined from the comparison images in the previous figure: (left) conventional mode at 20 KV, 20W, 114s, in which no overshooting is indicated, and (right) phase contrast mode at 60 KV, 20 W, 10s, which clearly demonstrates the overshooting resulting from the phase contrast effect.

The next comparison in this study involved the relative overshooting corresponding to the range of kV and *M* combinations investigated, in an effort to determine the optimal kV/*M* combination. Due to the differences in intensity values for the range of kV/*M* combinations, the edge profiles were normalized to facilitate effective comparison. Figure 52 presents a comparison of the range of magnification factors for an x-ray energy of 120 kV, which clearly demonstrates an increase in the amount of overshooting from the minimum at a magnification factor of 2 to the maximum at 3. This follows intuition, due to the fact that the phase contrast effect increases with magnification, as detailed previously.

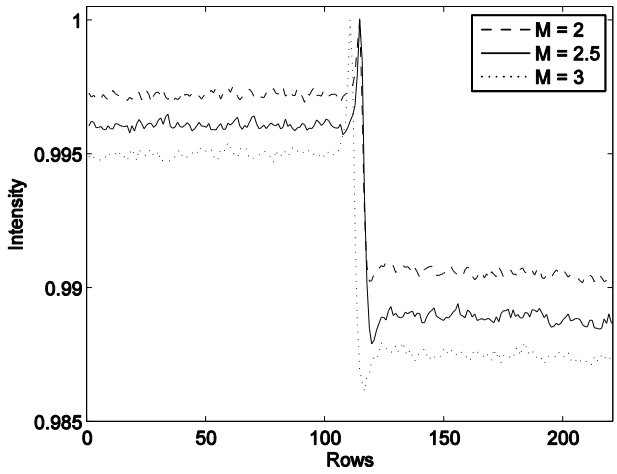

Figure 52: Comparison of edge profiles for an x-ray energy of 120 kV, which demonstrate the difference in the overshooting effect for the range of magnification factors.

Figure 53 provides a comparison of the range of x-ray energies for a magnification factor of 2.5. The differences among the curves are much less evident; however, the overshooting distinctly increases from the minimum for 140 kV to the maximum at 100 kV. This also follows intuition, due to the decrease of the phase contrast effect with x-ray energy discussed previously.

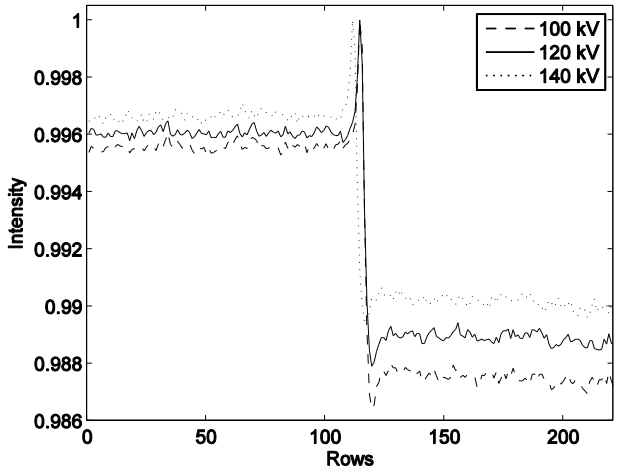

Figure 53: Comparison of edge profiles for a magnification factor of 2.5, which demonstrates the difference in the overshooting effect for the range of magnification factors.

The optimization of both parameters requires comparison of the entire range of kV/*M* combinations simultaneously, which is provided in Figure 54. One can distinguish the curves producing the largest amount of overshooting, which are the 100 kV, *M* = 3 curve, followed by the 120 kV, *M* = 3 curve and the 140 kV, *M* = 3 curve, respectively.

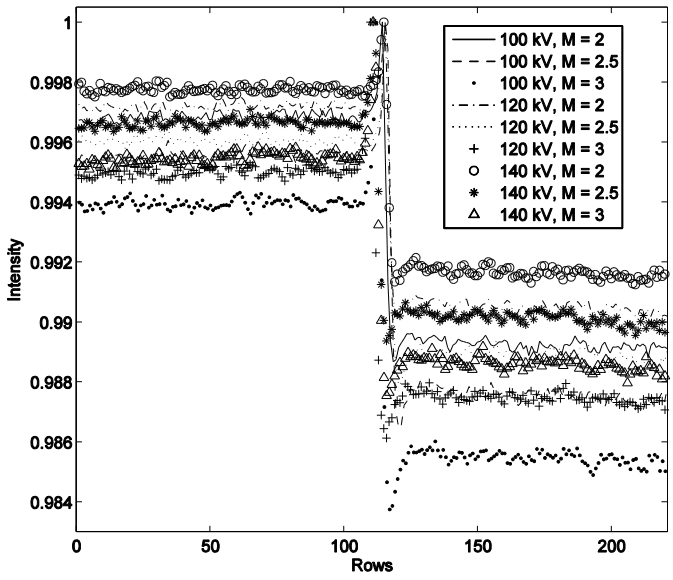

Figure 54: Comparison of edge profiles for the entire range of x-ray energies and magnification factors.

7.3.5 Tissue-Equivalent Phantom

Figure 55 provides the phase contrast images of the tissue-equivalent phantom, which were acquired at an x-ray energy of 140 kV with magnification factors of (a) 2.0, (b) 2.5, and (c) 3.0. As detailed previously, the tissue-equivalent phantom was designed to simulate a human breast, through not only the tissue composition but also the phantom thickness, the results of which are both of great importance in this study investigating the clinical feasibility of high energy phase contrast imaging for

mammography. Although the phantom images are an interesting simulation of a human breast, they clearly indicate the potential of the technology in both respects. The phase contrast effect is evident for the range of magnification factors, through not only the edge enhancement, but also the ability to distinguish fine features within the images. In particular, one can detect several of the ACR test objects within the phantom, through the dark masses located throughout the phantom, as well as the speck groups located at the bottom left of the image. Note that the brightest speck groups were not captured on the image, as the magnification produced an image larger than the detector. Since the phase contrast effect decreases with increasing x-ray energy, the image quality demonstrated in these images corresponding to the highest x-ray energy utilized in the study is encouraging.

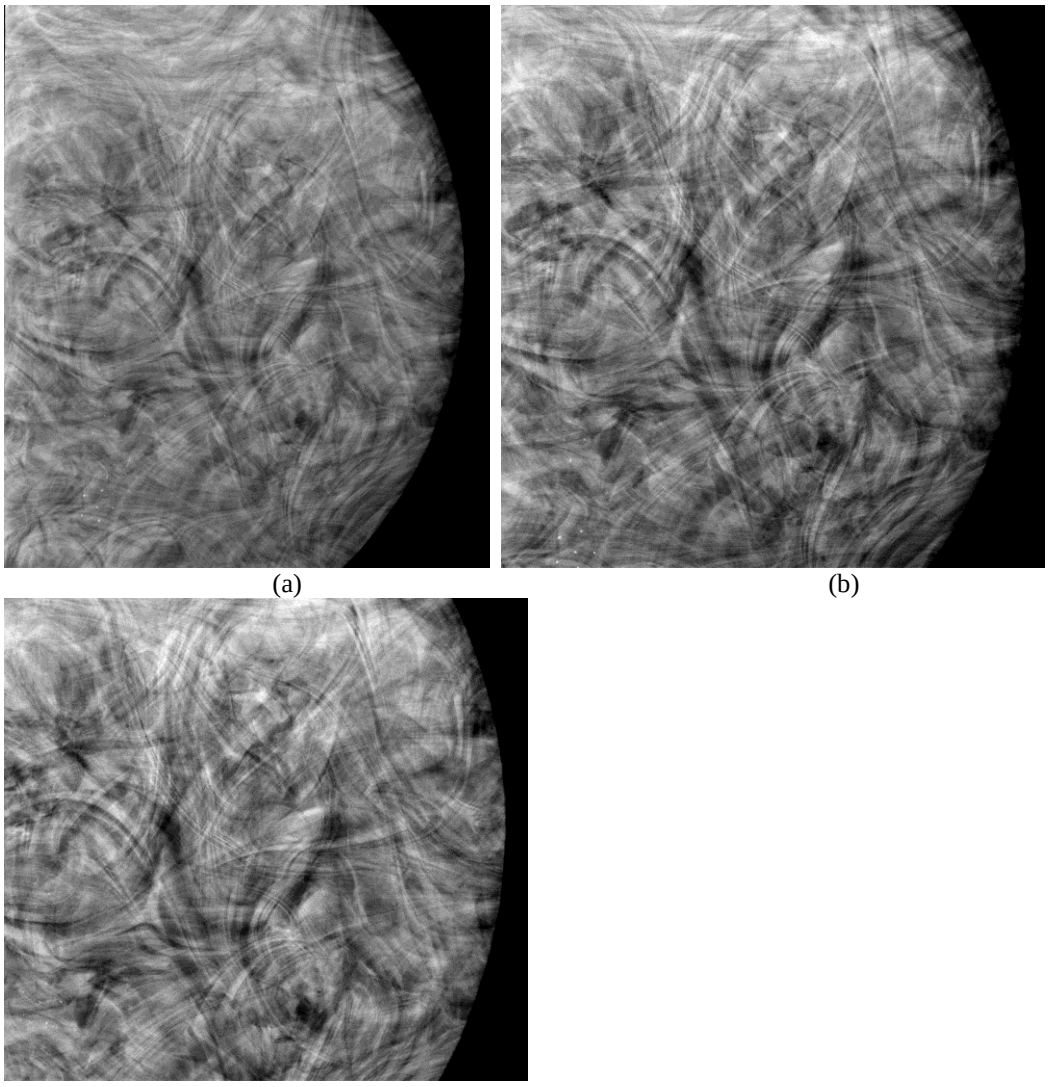

(a) (b)

(c)

Figure 55: Comparison of tissue-equivalent phantom images, which were acquired at an x-ray energy of 140 kV and a magnification factor of (a) 2.0, (b) 2.5, and (c) 3.0.

7.4 Discussion

The goal of this study was to evaluate and optimize the performance of a phase contrast x-ray imaging system at high energies, in an effort to determine the potential to provide adequate image quality for detection and diagnosis, as well as overcome existing low energy phase contrast challenges with clinical implementation. To accomplish this, an image quality evaluation consisting of the following phantoms

was performed: ACR (full phantom and wax insert only), contrast-detail, acrylic edge and tissue-equivalent. Phantom images corresponding to a range of three x-ray energies: 100, 120 and 140kV, as well as three magnification factors: 2, 2.5 and 3.0, were compared to investigate the relative image quality and attempt to determine the optimal x-ray energy and magnification factor. The results indicate acceptable image quality in the phase contrast images for the complete range of x-ray energies and magnification factors. The ACR observer studies for the wax insert only and the full phantom both produced high scores for all images, with scores within one point for the full phantom. Small divergence was also exhibited among the contrast-detail curves, along with favorable image quality in the c-d phantom images. The image quality among the kV and *M* combinations was comparable for all phantoms, which renders it difficult to select a single optimal combination. However, the results demonstrate the ability of phase contrast imaging to sustain the image quality improvement at high x-ray energies and for clinical thicknesses, both of which indicate the potential to benefit fields such as mammography.

8 Image Quality Comparison of High Energy Phase Contrast to High and Low Energy Conventional Images

8.1 Introduction

The research study[196] presented in this chapter comprises a continuation of the research detailed in Chapter 7, which involved investigating the feasibility of high energy phase contrast imaging to provide acceptable image quality for detection and diagnosis. This was accomplished through comparisons of phase contrast phantom images for a range of nine x-ray energy and magnification factor combinations, which demonstrated favorable image quality for all combinations. The next stage in the investigation of high energy phase contrast imaging consists of a comprehensive comparison of the phantom images acquired in the previous study to conventional images. This study involves a comparison with both high energy conventional and low energy conventional, in an effort to demonstrate the benefits of high energy phase contrast imaging in comparison to conventional imaging at the same energy as well as current clinical energies. The ability to deliver superior image quality in both situations will indicate the potential of high energy phase contrast imaging to improve the field of mammography. The images for both comparisons were acquired with experimental settings selected to deliver similar object entrance exposures.

8.2 High Energy Conventional

8.2.1 Experimental Design

The experimental design utilized for this study was identical to the details provided in Section 7.2, with the addition of a second set of comparison images in conventional imaging mode. Figure 56 demonstrates both configurations for comparison purposes: (a) the phase contrast configuration detailed thoroughly in Chapter 7, and (b) the configuration utilized in this study for acquisition of the conventional images, which requires the object to be placed directly in contact with the detector.

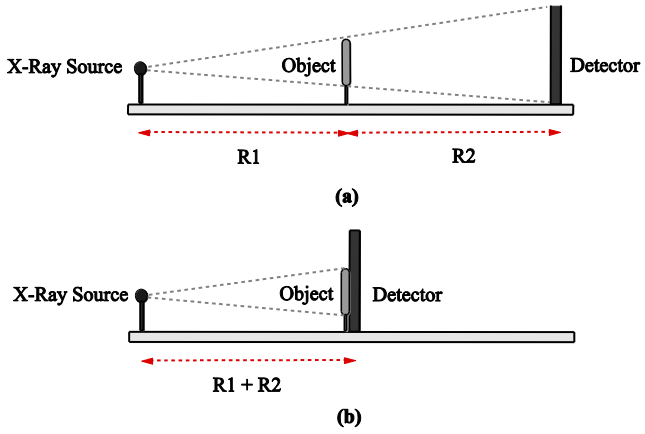

Figure 56: Comparison of system configurations for (a) phase contrast imaging mode and (b) conventional imaging mode. The same *R1* value was utilized to facilitate comparison of phase contrast and conventional images with similar object entrance exposures.

Once again, the x-ray energies of 100, 120 and 140 kV were investigated, along with the magnification factors of 2, 2.5 and 3. For each of the resulting nine combinations, high energy conventional images were obtained of the same phantoms: ACR (full and wax insert), contrast-detail, acrylic edge, and tissue-equivalent. Each set of conventional images was acquired with the same exposure time and *R1* value as the

phase contrast kV/*M* combination, in order to facilitate comparison of the phase contrast and conventional images with similar object entrance exposure.

8.2.2 Results

Undetectable Phantoms

The conventional images of the ACR wax insert, contrast-detail and acrylic edge phantoms were completely undetectable for the range of kV and *M* combinations, and therefore a comparison cannot be made to the phase contrast images. This can probably be attributed to the small thicknesses of the phantoms, which were specified previously as 7 mm, 1 cm, and 1.5 mm, respectively. Due to the lower attenuation of x-rays at high energies, the phantoms were not thick enough to attenuate an adequate amount of x-ray photons to produce contrast on the image. On the other hand, the phase contrast images of the three phantoms in Figures 45, 47 and 49 were not only detectable, but also demonstrated notable image quality. Although an explicit image comparison cannot be made, the ability of phase contrast imaging to overcome these challenges and produce a distinguishable image clearly demonstrates the benefits of phase contrast imaging in comparison to conventional imaging.

Full ACR Phantom

The full ACR phantom was detectable on the conventional images, and Figures 57 through 59 provide side-by-side comparisons to the phase contrast images. First, Figure 57 presents a phase contrast image in (a) and a conventional image in (b), which were both acquired at an x-ray energy of 100 kV and a magnification factor of

2.0. Similarly, Figure 58 compares images acquired at 100 kV and M = 2.5, and Figure 59 presents images acquired at 100 kV and M = 3.0. In all comparisons, the difference between the phase contrast and conventional images is demonstrated in the inability to distinguish any of the test objects in the conventional images with adequate contrast. Note that even the model number at the top of the image exhibits low contrast. This comparison clearly demonstrates the phase contrast effect, as the magnitude of the image quality improvement exhibited by the phase contrast images in comparison to the conventional images cannot be attributed solely to magnification.

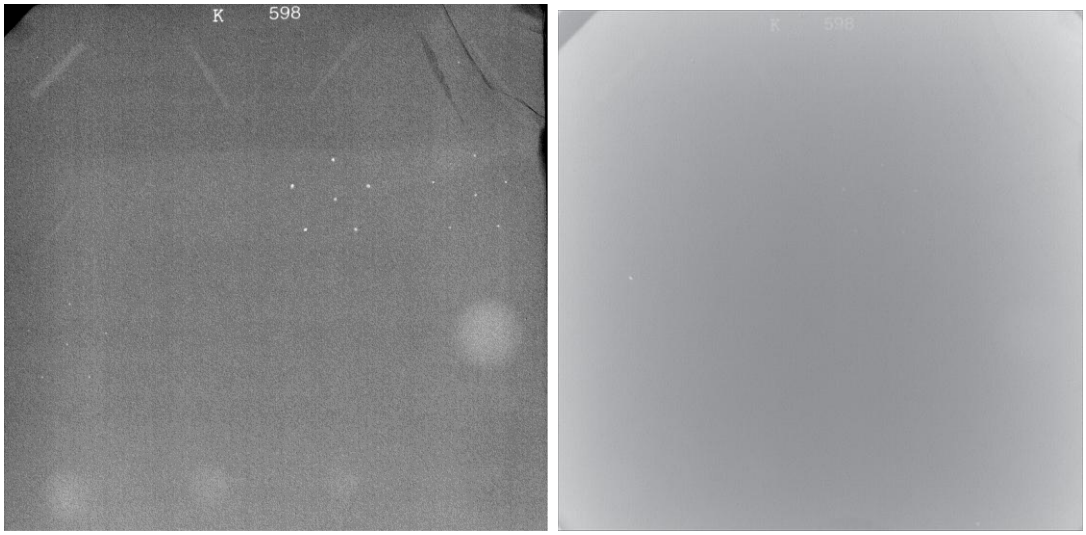

(a) (b)

Figure 57: Comparison of full ACR phantom images acquired at 100 kV and M = 2 in (a) phase contrast mode, and (b) conventional mode.

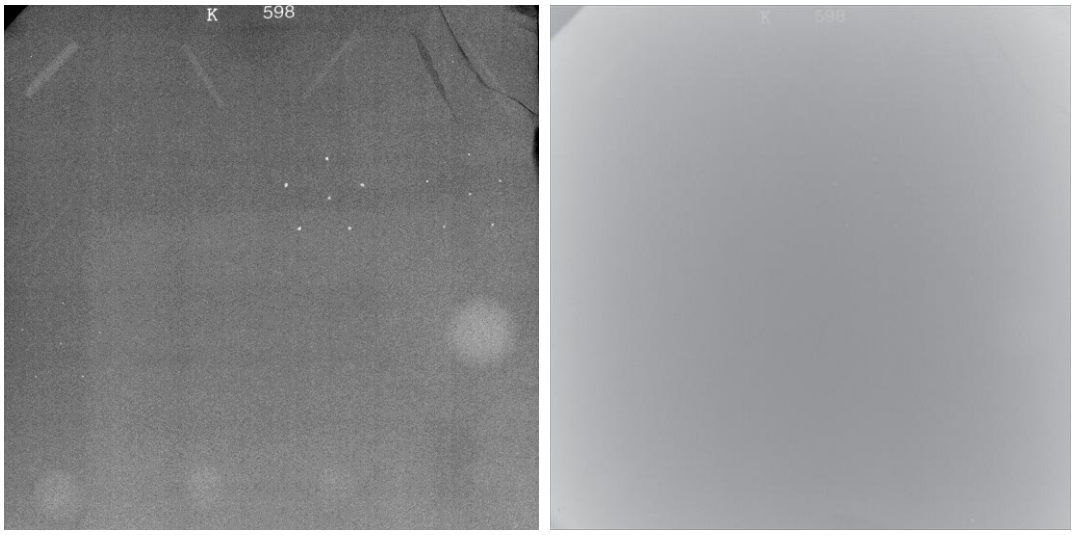

(a) (b)

Figure 58: Comparison of full ACR phantom images acquired at 100 kV and *M* = 2.5 in (a) phase contrast mode, and (b) conventional mode.

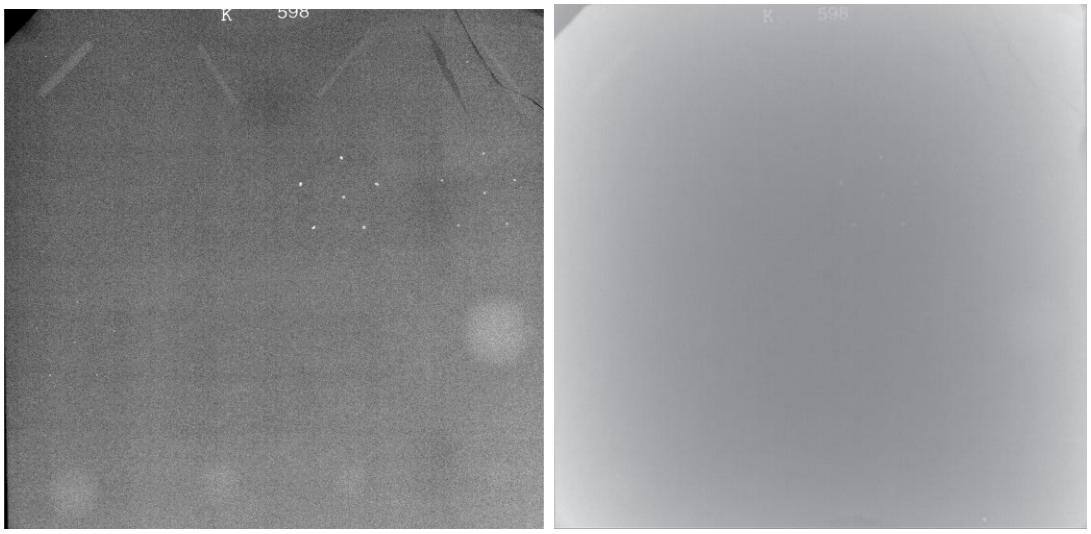

(a) (b)

Figure 59: Comparison of full ACR phantom images acquired at 100 kV and *M* = 3 in (a) phase contrast mode, and (b) conventional mode.

Tissue-Equivalent Phantom

The phase contrast and conventional comparisons of the tissue-equivalent phantom images are provided in Figures 60 through 62. First, Figure 60 presents a comparison of images acquired at an x-ray energy of 140 kV and a magnification factor of 2.0 in (a) phase contrast mode, and (b) conventional mode. Similarly, Figure 61 compares

images acquired at 140 kV and M = 2.5, and Figure 62 presents images acquired at 140 kV and M = 3.0.

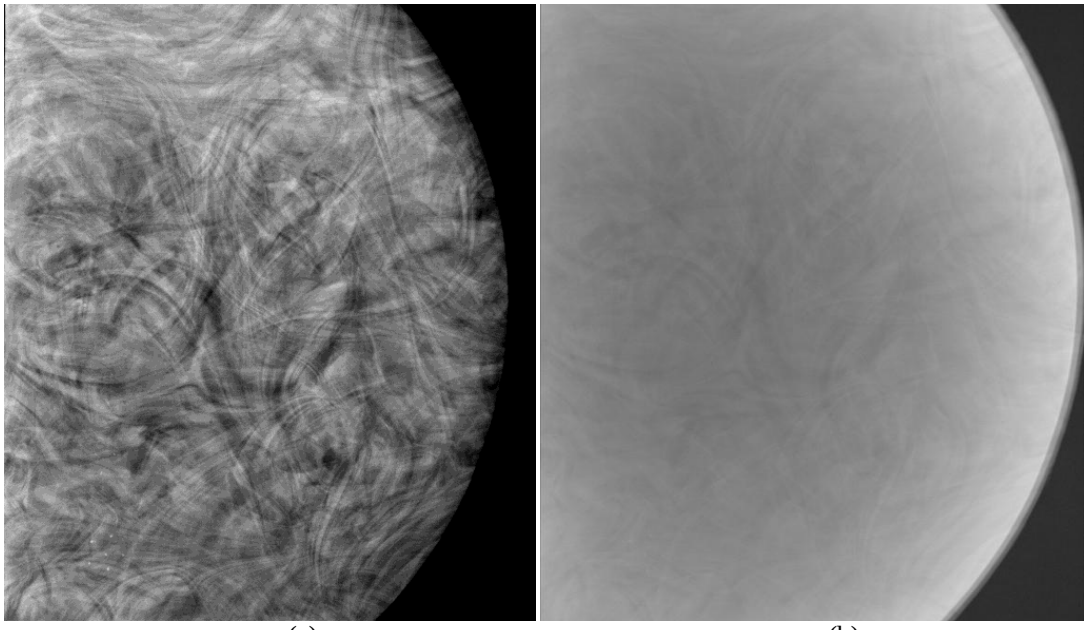

(a) (b)

Figure 60: Comparison of tissue-equivalent phantom images acquired at 140 kV and M = 2 in (a) phase contrast mode, and (b) conventional mode.

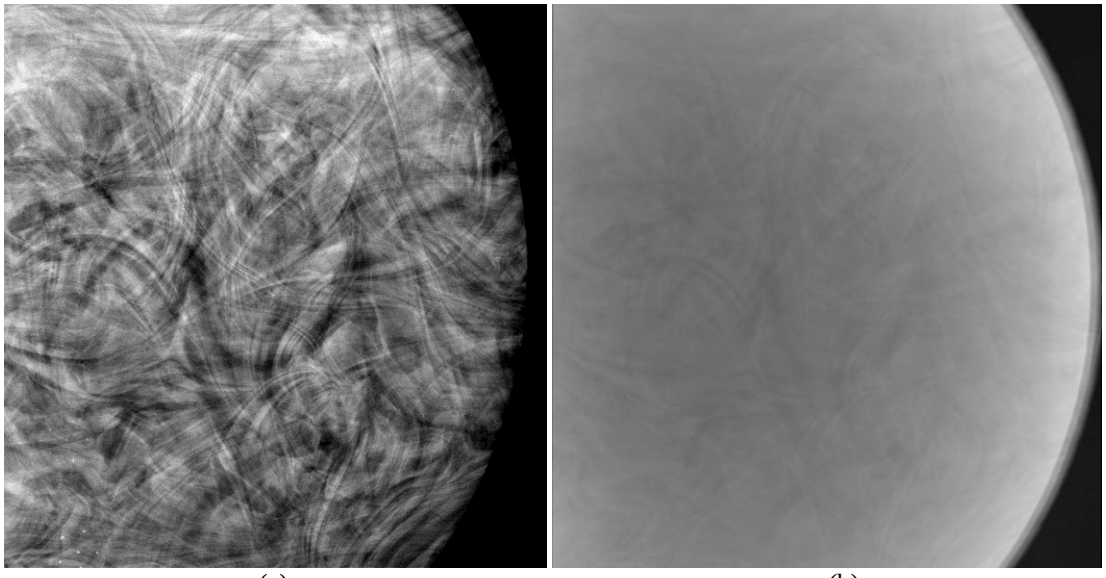

(a) (b)

Figure 61: Comparison of tissue-equivalent phantom images acquired at 140 kV and M = 2.5 in (a) phase contrast mode, and (b) conventional mode.

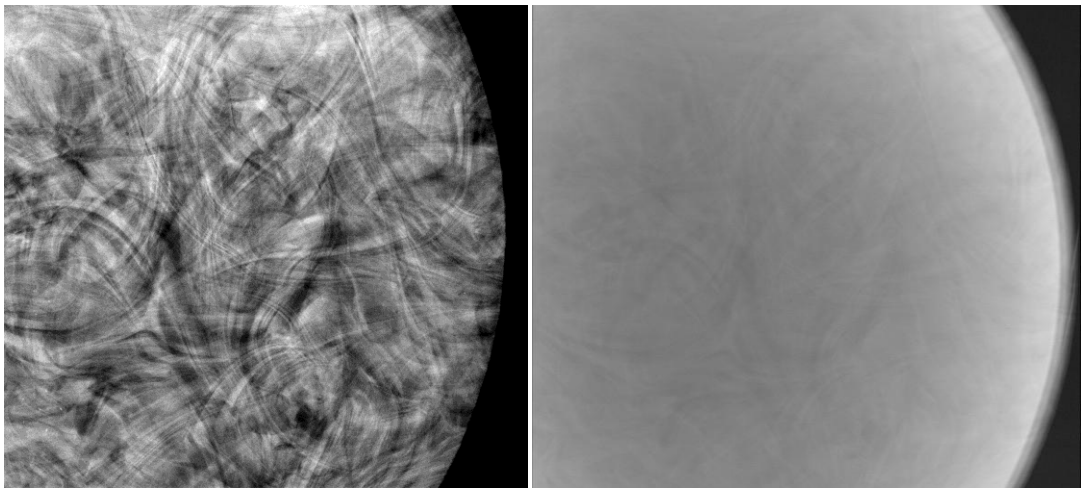

(a) (b)

Figure 62: Comparison of tissue-equivalent phantom images acquired at 140 kV and *M* = 3 in (a) phase contrast mode, and (b) conventional mode.

The difference between the high energy phase contrast and conventional images is clearly demonstrated in the significantly lower contrast of the structures within the phantom. The conventional images lack adequate contrast for distinguishing any of the ACR test objects, while one can easily detect several of the objects in the phase contrast images. Once again, this comparison indicates the image quality enhancement provided by phase contrast imaging in comparison to conventional imaging, as well as the ability to sustain the improvement at high energies and for clinical thicknesses.

8.3 Low Energy Conventional

8.3.1 Experimental Design

The experimental design utilized for the comparison of high energy phase contrast imaging with low energy conventional imaging is identical to the design detailed in

Section 8.2.1 and Chapter 7, with the exception of the selection of a specific x-ray energy and magnification factor combination for acquisition of the images. A single kV/*M* combination was utilized for efficiency purposes, due to the fact that the previous comparisons illustrated similar results for all kV/*M* combinations. Therefore, the images acquired for the comparison of high energy phase contrast imaging with low energy conventional imaging at similar entrance exposures was 100 kV, $M = 2.5$ (Phase Contrast mode) and 40 kV, $M = 1$ (Conventional mode). The source-to-object distance (*R1*) was 73.15 cm for both configurations. In conventional imaging mode, the detector was placed in contact with the image, while the source-to-detector distance (*R1+R2*) was 182.88 cm for phase contrast mode, which corresponds to a magnification factor of 2.5. Due to the difference in x-ray energies, different tube currents were utilized to maintain a consistent focal spot size of 7 µm, as detailed previously. Also, the exposure times for the modes were determined separately to maintain a constant object entrance exposure of 1 R. The experimental settings for both modes are provided in Table 16.

Magnification	X-ray Energy (kV)	Tube Current (µA)	Exposure Time (s)
1	40	250	122
2.5	100	100	109

Table 16: Experimental settings for the comparison of high energy phase contrast imaging and low energy conventional imaging, which were selected to maintain a constant object entrance exposure of 1 R and a constant focal spot size of 7 µm.

8.3.2 Results

Full ACR Phantom

The phase contrast and conventional images of the full ACR phantom are provided in Figure 63 (a) and (b), respectively. In the low energy conventional image, some of the test objects can be distinguished, which is an improvement from the high energy conventional images illustrated in the previous section. However, the phase contrast image clearly exhibits superior image quality in the number of objects distinguishable, as well as the contrast between the objects and the background.

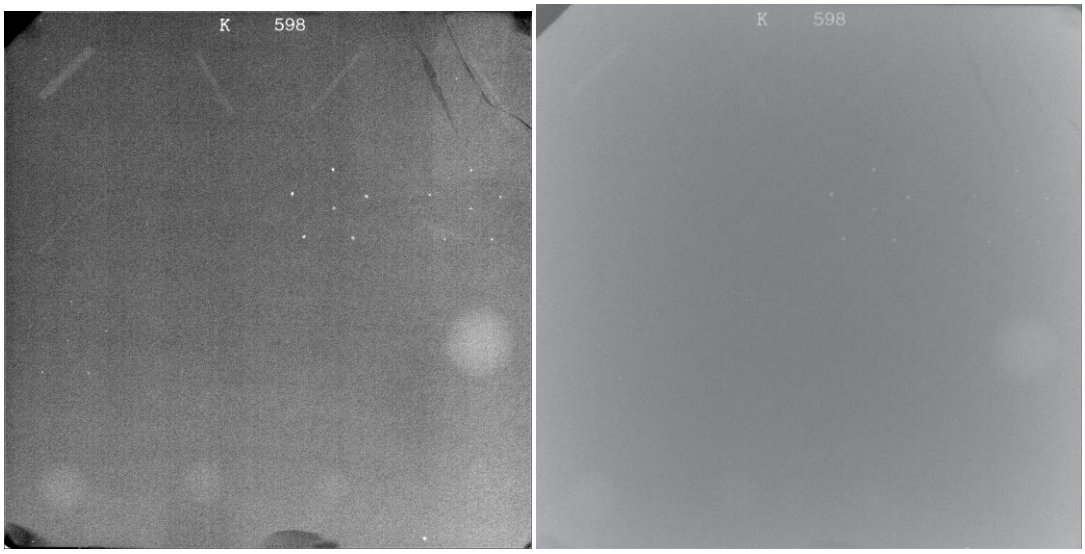

(a) (b)

Figure 63: Comparison of full ACR phantom images acquired at the following experimental settings: (a) 100 kV, 100 µA, 109s, *M* = 2.5 (phase contrast mode), and (b) 40 kV, 250 µA, 122s, *M* = 1 (conventional mode).

Contrast-Detail Phantom

The phase contrast and conventional images of the contrast-detail phantom are provided in Figure 64 (a) and (b), respectively. Only the top four rows of the phantom are shown to allow closer inspection of the relative image quality. Most of the test

objects can be distinguished in both images. However, the improved image quality in the phase contrast image is exhibited through the white lines highlighting the test objects, demonstrating the edge enhancement provided by the phase contrast effect. Contrastingly, the test objects reveal much lower contrast in the conventional image.

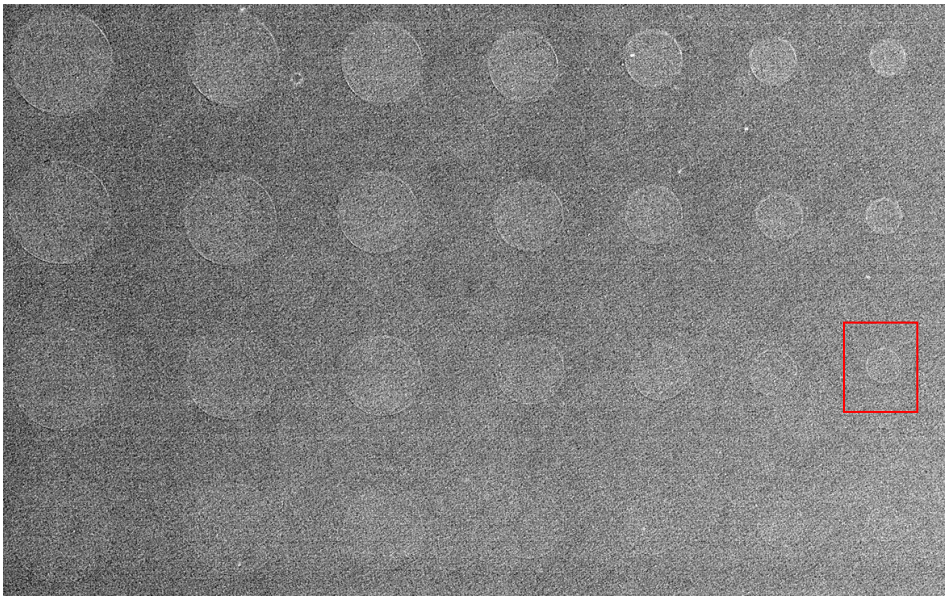

(a)

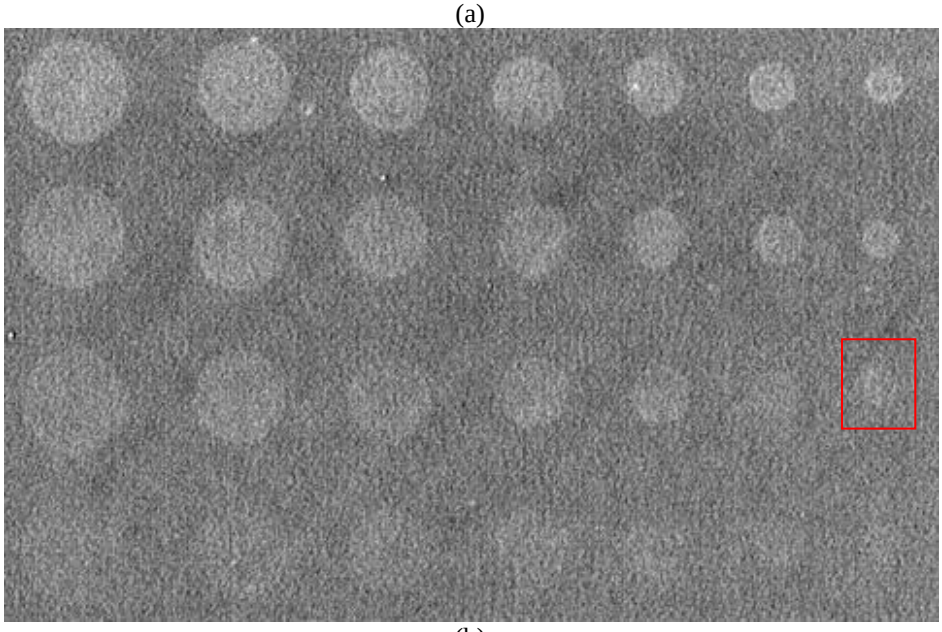

(b)

Figure 64: Comparison of contrast-detail phantom images acquired at the following experimental settings: (a) 100 kV, 100 µA, 109s, *M* = 2.5 (phase contrast mode), and (b) 40 kV, 250 µA, 122s, *M* = 1 (conventional mode).

For comparison purposes, one of the test objects has been outlined with a red box in both images in Figure 64. Note how the test object is clearly outlined by a white circle in the phase contrast image, while the same object is almost indistinguishable in the conventional image.

Acrylic Edge Phantom

The phase contrast and conventional acrylic edge phantom images are provided in Figure 65 (a) and (b), respectively. The difference in the relative contrast across the edge demonstrates the phase contrast effect in comparison to conventional imaging. In addition, the white line highlighting the edge in the phase contrast image is a clear indication of the overshooting effect, which produces the edge enhancement. As detailed previously, the overshooting is graphically demonstrated through comparison of the edge profiles, which is provided in Figure 66. The edge profiles have been normalized for comparison purposes. In the figure, the difference between the edge profiles illustrates the overshooting effect that produced the improvement in the quality of the phase contrast image in Figure 65, as compared to the conventional image.

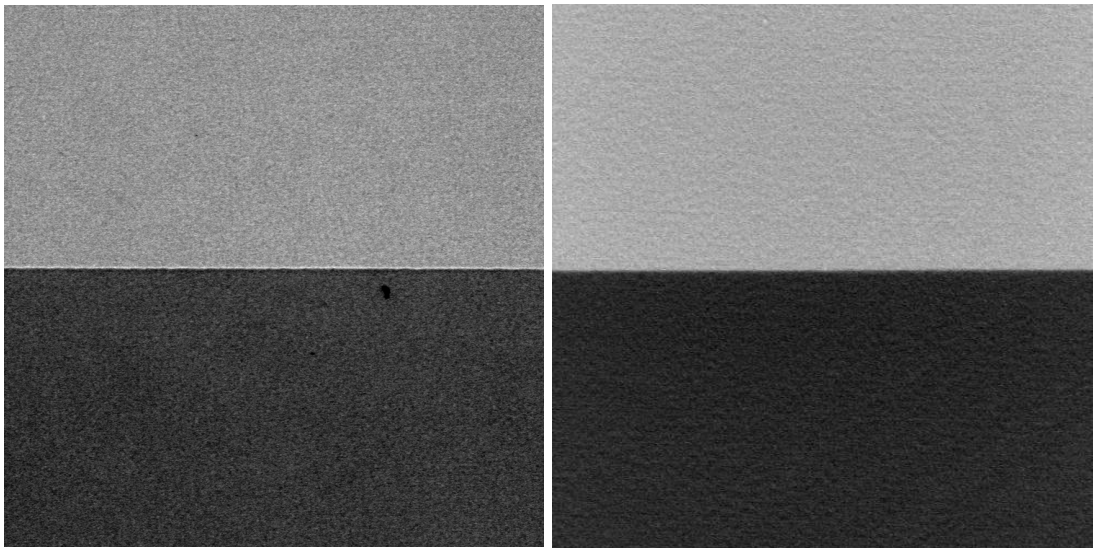

(a) (b)

Figure 65: Comparison of acrylic phantom images acquired at the following experimental settings: (a) 100 kV, 100 µA, 109s, *M* = 2.5 (phase contrast mode), and (b) 40 kV, 250 µA, 122s, *M* = 1 (conventional mode).

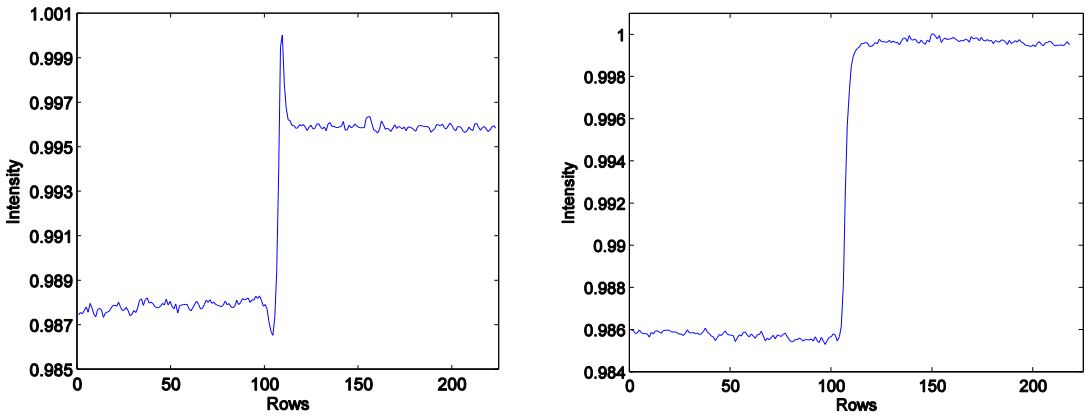

(a) (b)

Figure 66: Edge profiles determined from the acrylic edge comparison images: (a) 100 kV, 100 µA, 109s, *M* = 2.5 (phase contrast mode), which clearly demonstrates the overshooting resulting from the phase contrast effect, and (b) 40 kV, 250 µA, 122s, *M* = 1 (conventional mode), in which no overshooting is indicated.

Tissue-Equivalent Phantom

The phase contrast and conventional comparisons of the tissue-equivalent phantom images are provided in Figure 67 (a) and (b), respectively. Once again, the low energy conventional image demonstrates an improvement from the high energy

conventional image; however, the phase contrast maintains superior quality, which is revealed by the ability to distinguish the fine features within the phase contrast image with much higher contrast. In addition, several of the test objects can only be distinguished in the phase contrast image.

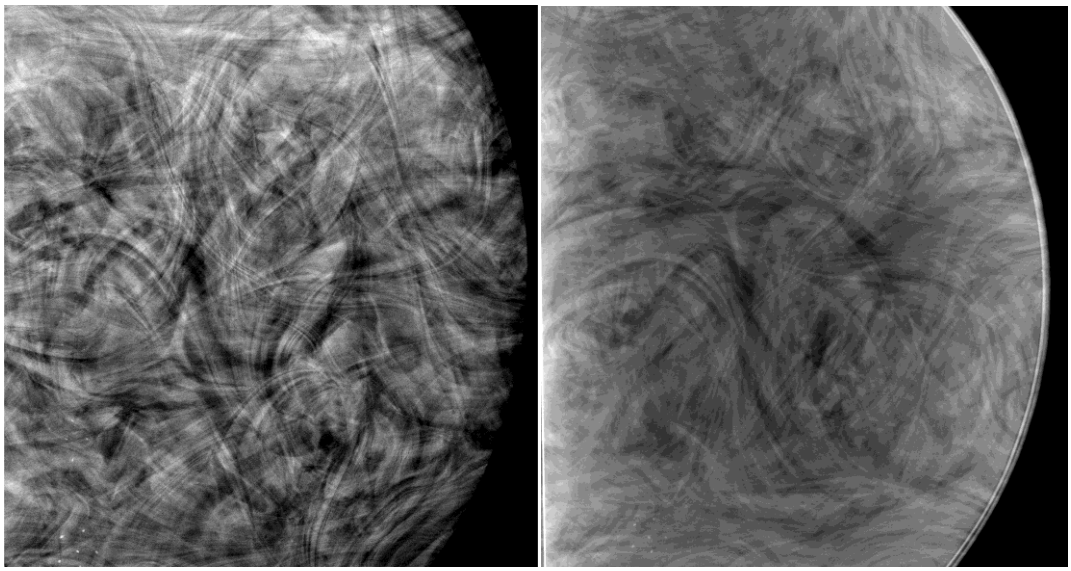

(a) (b)

Figure 67: Comparison of tissue-equivalent phantom images acquired at the following experimental settings: (a) 100 kV, 100 µA, 109s, *M* = 2.5 (phase contrast mode), and (b) 40 kV, 250 µA, 122s, *M* = 1 (conventional mode).

8.4 Discussion

The research presented in this chapter comprised separate investigations of the relative image quality provided by high energy phase contrast with high energy and low energy conventional images. In the high energy conventional comparison, the ACR wax insert, contrast-detail and acrylic edge phantoms were completely undetectable on the conventional images, while very fine features could easily be distinguished in the phase contrast images of the phantoms. The phase contrast full

ACR and tissue-equivalent images demonstrated a substantial improvement in image quality in comparison to the high energy conventional images. In both comparisons, the phase contrast images produced high contrast, allowing clear detection of objects within the images, while the conventional images produced little or no contrast, preventing detection of objects within the images. The results of this comparison clearly demonstrate the phase contrast effect, as the magnitude of the image quality improvement exhibited in the phase contrast images in comparison to the conventional images cannot be attributed solely to magnification. The low energy conventional images demonstrated an improvement as compared to the high energy conventional images, but the image quality was still inferior to the phase contrast images. The phase contrast image of all phantoms demonstrated much higher contrast than the conventional image. In addition, the overshooting effect producing the edge enhancement was clearly illustrated in the acrylic edge comparison, not only through the white line highlighting the edge, but also through the edge profile comparison.

The results of the comparisons presented in this chapter clearly demonstrate the capability of high energy phase contrast imaging to improve the image quality for the same entrance exposure in comparison with conventional imaging at high or low energies, as well as the ability to sustain the image quality improvement at high x-ray energies and for clinical thicknesses, all of which indicate the strong potential to benefit fields such as mammography.

9 Image Quality and Dose Comparison of High Energy Phase Contrast with Low Energy Conventional Imaging

9.1 Introduction

The research[198] presented in this chapter comprises a thorough investigation of the image quality of high energy phase contrast imaging in comparison with low energy conventional imaging at similar absorbed doses. This study was completed as an extension to the comparisons presented in Chapter 8, which were based on similar entrance exposures as an estimation of dose. This study involved a more accurate and significant comparison through directly calculating the average glandular dose coefficients for comparison of the relative image quality between high energy phase contrast and low energy conventional at similar doses. The combined image quality and dose comparison is a critical step in demonstrating the feasibility of the application of high energy phase contrast imaging in a clinical environment such as mammography to improve the detection and diagnosis capabilities without increasing the radiation dose.

9.2 Experimental Design

The investigation of high energy phase contrast imaging in comparison to low energy conventional imaging was accomplished through an image quality evaluation incorporating numerous phantoms: Academic College of Radiology (ACR), contrast-detail (CD), acrylic edge and tissue-equivalent. In this study, phase contrast images at 100 kV and a magnification factor of 2.5 were compared to conventional images at 40

kV with the same source-to-object distance. The D_{gN} values were determined for both settings, and the exposure time was selected accordingly for each to deliver an absorbed radiation dose of approximately 200 mRad.

System and Measurement Components

The phase contrast and conventional configurations were illustrated in Figure 57 in Section 8.2.1. The system and experimental design utilized in this study were identical to the high energy phase contrast comparison to low energy conventional at similar radiation doses, which was presented in Section 8.3.1. As detailed in that section, the high energy phase contrast images were acquired at 100 kV, 100 µA, M = 2.5, while the low energy conventional images were acquired at 40 kV, 250 µA, M = 1, and the source-to-object distance (*R1*) was 73.15 cm for both configurations. The difference in this study involved the separate selection of the exposure times for each mode to facilitate similar absorbed doses.

Dose Calculation

As detailed in several previous chapters, the average glandular dose D_g is based on the object entrance exposure (X_{ESE}) and the average glandular dose coefficient (D_{gN}). The measurements of object entrance exposure were obtained with a calibrated ionization chamber (10X9-180 ionization chamber, Model 9095 measurement system, Radcal Corporation, Monrovia, California). Five measurements at each mode were acquired in an effort to reduce the error in the measurements. The entrance exposure at exactly the same location as the object was measured for both phase contrast and conventional modes. The D_{gN} values for each mode were estimated with Monte Carlo

simulations through a process detailed in previous studies.[152-154] The simulations assumed the presence of an object with 50% adipose and 50% glandular tissue composition in the path of the x-ray beam. To deliver similar radiation doses for the phase contrast and conventional images, a target D_g amount of 200 mRad was selected, and the corresponding target object entrance exposure amount was determined for each mode based on the calculated D_{gN} value. The exposure time delivering the target object entrance exposure amount for each mode was then determined. Table 17 provides the D_{gN}, object entrance exposure, and exposure time values for each mode, both of which deliver a D_g value of approximately 200 mRad. Note that the calculated D_{gN} value for the phase contrast mode is larger than the value for the conventional mode by a factor of more than 2.5. Recalling the formula for the calculation of D_g, facilitating similar radiation doses between the modes therefore requires a difference by the same factor in the entrance exposure. Therefore, it is important to note the significance of performing the comparison based on similar radiation doses.

Magnification	X-ray Energy (kV)	Exposure Time (s)	Object Exposure (R)	D_{gN} (mrad/R)	D_g (mrad)
1	40	192	1.64	122.0	200.08
2.5	100	72	0.632	320.2	202.37

Table 17: Average glandular dose calculation values for the comparison of high energy phase contrast imaging and low energy conventional imaging. A target D_g value was selected, and the exposure times were determined separately for each mode in order to deliver the corresponding absorbed dose.

Phantoms

As detailed in Chapters 7 and 8, a thorough investigation was performed through the use of the following four phantoms: ACR, contrast-detail, acrylic edge and tissue-equivalent. The phantoms combine to provide three types of comparisons detailed previously: quantitative, qualitative and clinical. In addition, the acrylic edge phantom provides both a graphical and visual indication of the edge enhancement provided by phase contrast imaging in comparison to conventional imaging. The use of these four phantoms provides a comprehensive comparison, the goal of which is to demonstrate the clinical feasibility of high energy phase contrast imaging to improve the image quality without increasing the radiation dose.

9.3 Results

9.3.1 Full ACR Phantom

The full ACR phantom images acquired with high energy phase contrast imaging and low energy conventional imaging are provided in Figure 68 (a) and (b), respectively. The images exhibit very similar image quality, which indicates the capability of the technique of high energy phase contrast imaging to meet the existing image quality standards designed for attenuation contrast imaging. The number of test objects distinguishable between the images is comparable, although the phase contrast image exhibits higher contrast between the objects and the background.

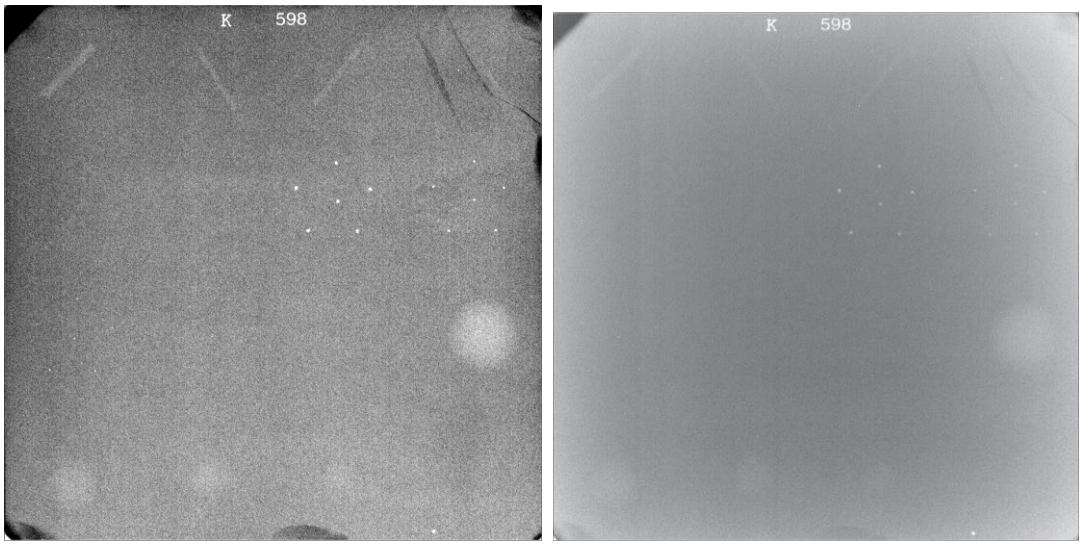

(a) (b)

Figure 68: Comparison of full ACR phantom images acquired at the following experimental settings: (a) 100 kV, 100 µA, 72s, *M* = 2.5 (phase contrast mode), and (b) 40 kV, 250 µA, 192s, *M* = 1 (conventional mode).

The ACR phantom image scores are provided in Table 18, which reinforces the visual indication of comparable image quality. It is also interesting to note the higher scores achieved by the phase contrast images in the specks category. The ability to distinguish the smallest test objects more clearly is an indication of the improvement in image quality provided by phase contrast imaging.

Mode	Fibers	Specks	Masses	Total
40 kV Conventional	4.5	3	4	**11.5**
100 kV Phase Contrast	4.5	4	4	**12.5**

Table 18: Comparison of ACR scores for the high energy phase contrast and low energy conventional images of the ACR phantom.

9.3.2 Contrast-Detail Phantom

The contrast-detail phantom images acquired with high energy phase contrast imaging and low energy conventional imaging are provided in Figure 69 (a) and (b), respectively. Only the top four rows of the phantom are shown to allow closer inspection of the relative image quality. The number of test objects distinguished is comparable between the images, once again an indication of the capability of phase contrast imaging to meet the existing image quality standards designed for attenuation contrast imaging. However, the improved image quality in the phase contrast image is exhibited through the white lines highlighting the test objects, demonstrating the edge enhancement provided by the phase contrast effect. Contrastingly, the test objects reveal much lower contrast in the conventional image.

Next, the contrast-detail curves were generated according to the procedures detailed previously, and Figure 70 provides a comparison of the c-d curves corresponding to high energy phase contrast and low energy conventional imaging. As detailed previously, superior image quality is demonstrated by a curve closer to the x-y axis, which is the phase contrast curve.

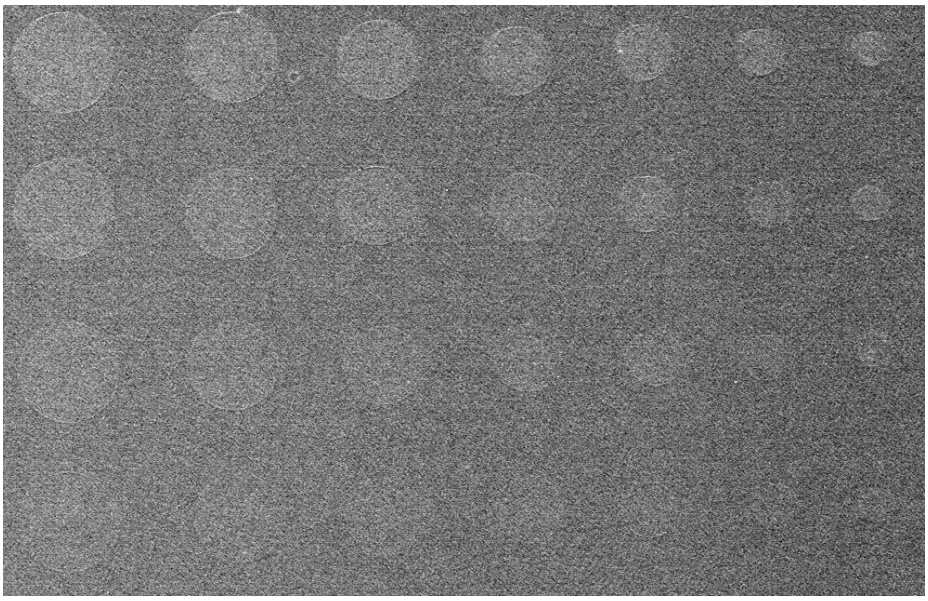

(a)

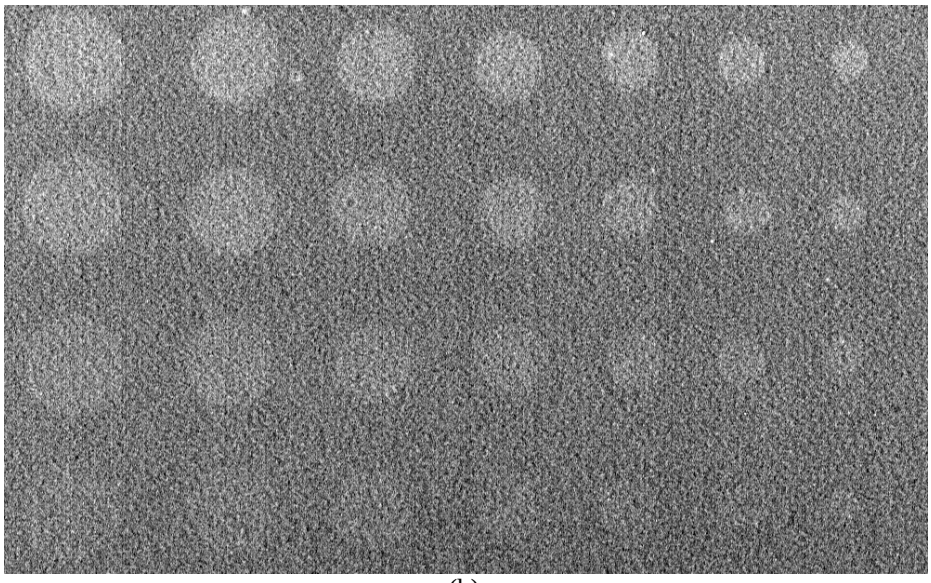

(b)

Figure 69: Comparison of contrast-detail phantom images acquired at the following experimental settings: (a) 100 kV, 100 µA, 72s, *M* = 2.5 (phase contrast mode), and (b) 40 kV, 250 µA, 192s, *M* = 1 (conventional mode).

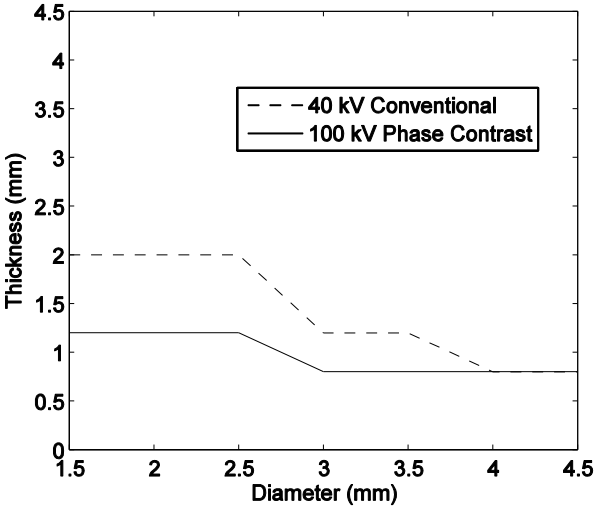

Figure 70: Comparison of contrast-detail curves generated from the high energy phase contrast and low energy conventional phantom images.

9.3.3 Acrylic Edge Phantom

The acrylic edge phantom images acquired by the high energy phase contrast and low energy conventional modes are provided in Figure 71 (a) and (b), respectively. Once again, the edge is much more clearly distinguished in the phase contrast image as compared to the conventional image, indicating the edge enhancement provided by phase contrast. In addition, the phase contrast overshooting effect is demonstrated through the white line highlighting the edge.

As a second demonstration of the phase contrast effect, edge profiles for the phase contrast and conventional modes are provided for comparison in Figure 72 (a) and (b), respectively. The edge profiles have been normalized to facilitate effective comparison. In contrast to the conventional image, the phase contrast image exhibits

overshooting along the edge transition, which is a graphical indication of the edge enhancement illustrated in Figure 71 (a).

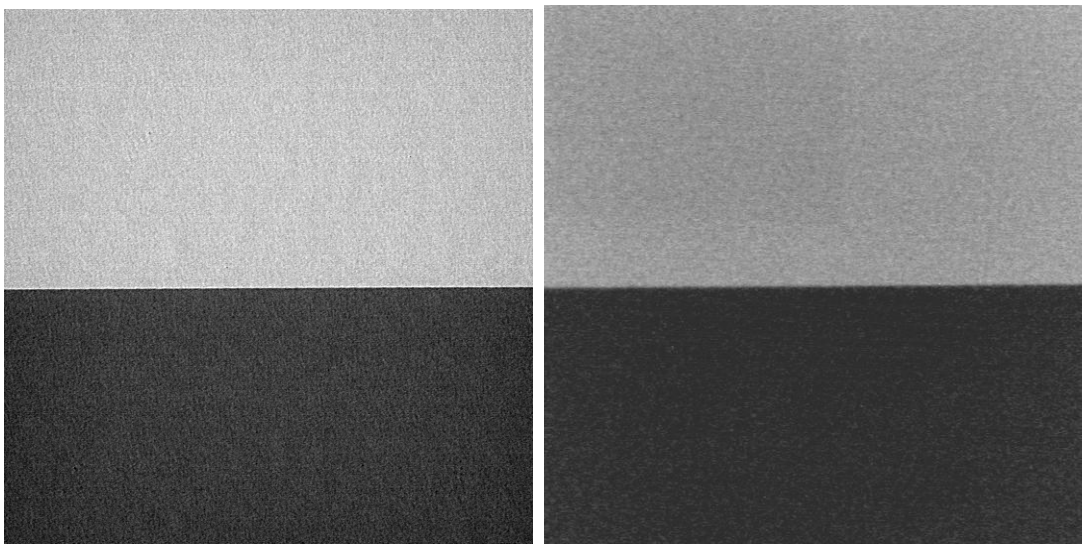

(a) (b)

Figure 71: Comparison of acrylic edge phantom images acquired at the following experimental settings: (a) 100 kV, 100 µA, 72s, *M* = 2.5 (phase contrast mode), and (b) 40 kV, 250 µA, 192s, *M* = 1 (conventional mode).

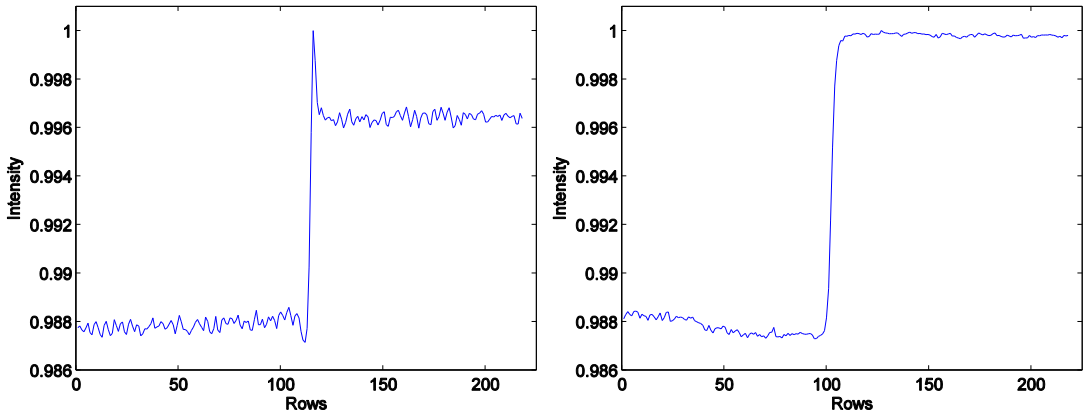

(a) (b)

Figure 72: Edge profiles determined from the acrylic edge comparison images: (a) 100 kV, 100 µA, 72s, *M* = 2.5 (phase contrast mode), which clearly demonstrates the overshooting resulting from the phase contrast effect, and (b) 40 kV, 250 µA, 192s, *M* = 1 (conventional mode), in which no overshooting is indicated.

9.3.4 Tissue-Equivalent Phantom

The tissue-equivalent phantom images acquired by the high energy phase contrast and low energy conventional modes are provided in Figure 73 (a) and (b), respectively. As detailed previously, the tissue-equivalent phantom was designed to simulate a human breast, through not only the tissue composition but also the phantom thickness, the results of which are both of great importance in this study investigating the clinical feasibility of high energy phase contrast imaging for mammography. The phase contrast image in Figure 73 (a) clearly indicates the potential of the technology in both respects. The phase contrast effect is evident in the image, through not only the edge enhancement, but also the ability to distinguish fine features within the images. The difference between the phase contrast and conventional images is clearly demonstrated in the lower contrast of the structures within the phantom. The comparison indicates the image quality enhancement provided by phase contrast imaging in comparison to conventional imaging, as well as the ability to sustain the improvement at high energies and for clinical thicknesses. In addition, several of the test objects can only be distinguished in the phase contrast image.

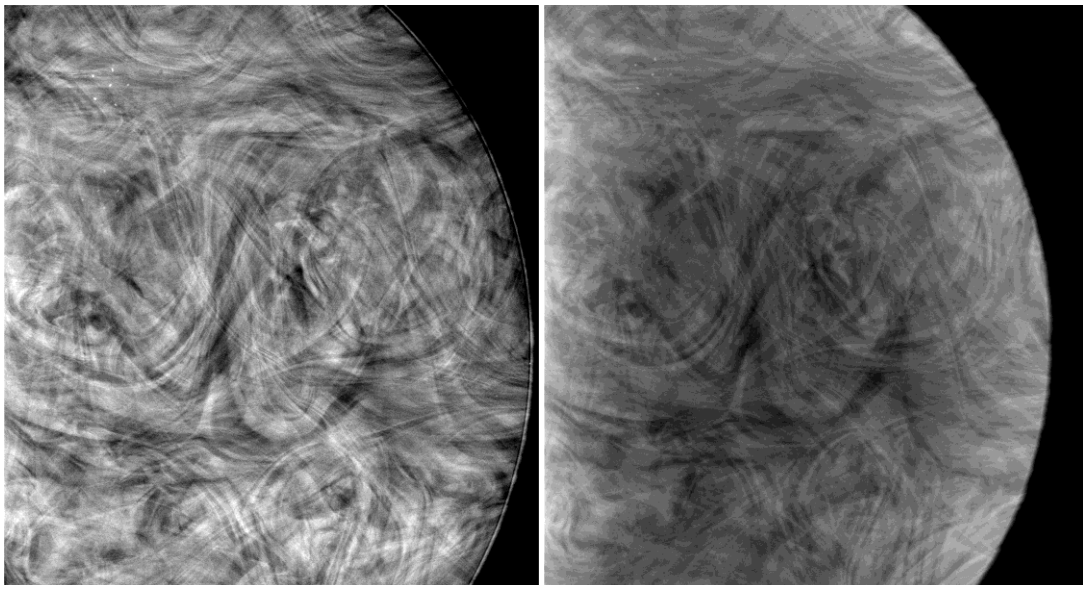

(a) (b)

Figure 73: Comparison of tissue-equivalent phantom images acquired at the following experimental settings: (a) 100 kV, 100 µA, 72s, *M* = 2.5 (phase contrast mode), and (b) 40 kV, 250 µA, 192s, *M* = 1 (conventional mode).

9.4 Conclusion

The primary goal of this study was to compare the image quality provided by high energy phase contrast images with conventional images at typical mammography energies, in an effort to determine the potential of high energy phase contrast imaging to increase the image quality at a similar radiation dose. To accomplish this, an image quality evaluation consisting of the following phantoms was performed: ACR, contrast-detail, acrylic edge and tissue-equivalent. High energy phase contrast and low energy conventional images of each phantom were acquired with similar absorbed radiation doses for investigation of the relative image quality. Visual comparison of the phantom images indicated comparable or improved image quality

for all phantoms. In addition, quantitative comparisons were performed through the ACR scores and contrast-detail curves, both of which indicated higher image quality in the phase contrast images. The results of this study clearly demonstrate the phase contrast effect through the edge enhancement, which is most notable in the contrast-detail and acrylic edge images. In addition, the results demonstrate the ability of phase contrast imaging to sustain the image quality improvement at high x-ray energies and for clinical thicknesses without a dose increase, which is a strong indication of the potential to benefit fields such as mammography.

10 Conclusion

10.1 Summary

The research presented in this dissertation encompasses numerous investigations directly applying the research methods detailed in Chapter 2, which required extensive knowledge of the theory and application of image quality, statistical methods, phase contrast imaging, and radiation dose. In addition, the investigations detailed in Chapters 3 through 9 clearly demonstrate the capability to identify research topics and design, implement and analyze independent research studies. Each chapter presented research involving original contributions, which were made in an effort to improve existing processes or present a new process to the research community.

First, Chapter 3 presented the development and characterization of a low energy phase contrast imaging system prototype, as well as the comprehensive comparison to low energy conventional imaging. This chapter not only demonstrated the feasibility of phase contrast imaging through numerous image quality evaluation and comparison methods, but also provided the development of numerous research methods to facilitate the investigation of a high energy phase contrast imaging system prototype for the dissertation research.

Next, Chapter 4 presented a method for optimization of the modulation transfer function (MTF) algorithm. The approach performed independent evaluations of the

methods available for each MTF step for the first time, and the significance of separate comparisons was demonstrated by the results. In addition, this study presented several new techniques or combinations of techniques that had not previously been applied to the MTF algorithm, which provided comparable or superior results to the established methods. The combination of the use of new methods and the individual selection of the optimal method for each step both indicate the potential of these results to considerably improve the accuracy of the MTF edge algorithm.

A comprehensive error analysis of the photon fluence contribution to the detective quantum efficiency (DQE) was detailed in Chapter 5, which presented a quantitative method to determine the error contributing to a result by each of the components represented in the calculation. Although this method could potentially be applied to an extensive range of applications, the effectiveness and usefulness of the method was demonstrated through determining the error contributed to the DQE by the photon fluence calculation. In addition, a new method for calculation of the magnification amount was developed for the study, in an effort to reduce the error introduced by the traditional use of rulers in the calculation. The new method was determined to be independent of SID, and the application of the method in a clinical environment holds the potential to greatly reduce the error. Finally, the relationship between the number of measurements and the random error within the measurements was investigated for both the exposure and spectrum measurements, which reveal that averaging 20 or more measurements can drastically reduce the error in the results.

The relationships reported had not been presented previously, and can be utilized as guidelines for future studies in selecting an adequate number of measurements to balance the measurement time and error produced in the results.

The beam hardening investigation presented in Chapter 6 comprised an evaluation on the correlated effects of a technique known as x-ray beam hardening on the DQE and radiation dose. Although moderate beam hardening is currently utilized in clinical environments, the use of added beam hardening had not been investigated previously, to the best of my knowledge. The results of the study indicate a notable dose reduction for the range of beam hardening levels investigated, while the comparisons of the MTF, NPS, NEQ and DQE revealed only slight differences for the range of beam hardening levels. The study therefore demonstrated the potential to significantly improve the field of mammography, through reducing the radiation dose without negatively affecting the detection capabilities.

The goal of the study presented in Chapter 7 was to evaluate and optimize the performance of a phase contrast x-ray imaging system at high energies, in an effort to determine the potential to provide adequate image quality for detection and diagnosis, as well as overcome existing low energy phase contrast challenges with clinical implementation. Phantom images corresponding to a range of three x-ray energies: 100, 120 and 140kV, as well as three magnification factors: 2, 2.5 and 3.0, were compared to investigate the relative image quality for the same entrance exposure and attempt to determine the optimal x-ray energy and magnification factor. The results

indicate acceptable image quality for the phase contrast images of all phantoms within the complete range of x-ray energies and magnification factors. The image quality among the kV and *M* combinations was comparable, which made it difficult to select a single optimal combination. However, the results demonstrated for the first time the ability of phase contrast imaging to sustain the image quality improvement at high x-ray energies and for clinical thicknesses, both of which indicate considerable potential to benefit fields such as mammography.

The research presented in Chapter 8 comprised separate comparisons of the relative image quality provided by high energy phase contrast with high energy and low energy conventional images. In the high energy conventional comparison, the ACR wax insert, contrast-detail and acrylic edge phantoms were completely undetectable on the conventional images, while very fine features could easily be distinguished in the phase contrast images of the phantoms. The phase contrast full ACR and tissue-equivalent images demonstrated a substantial improvement in image quality in comparison to the high energy conventional images. The low energy conventional images demonstrated an improvement as compared to the high energy conventional images, but the image quality was still inferior to the phase contrast images. The phase contrast image of all phantoms demonstrated much higher contrast than the conventional image. The results of this study strengthen the results of Chapter 7 in indicating the clinical potential of phase contrast imaging to benefit mammography through increasing the x-ray energy.

Finally, the study presented in Chapter 9 expanded the research of Chapter 8 further, through performing an image quality comparison of high energy phase contrast images with low energy conventional images at similar radiation doses, which is a more accurate and clinically relevant comparison. The image quality evaluation involved four phantoms collectively providing quantitative, qualitative and clinical comparisons. Visual comparison of the phantom images indicated comparable or improved image quality for all phantoms. In addition, quantitative comparisons were performed through ACR scores and contrast-detail curves, both of which indicated higher image quality in the phase contrast images. The results of this study clearly demonstrate the phase contrast effect through the edge enhancement, which is most notable in the contrast-detail and acrylic edge images. In addition, the results demonstrate the ability of phase contrast imaging to sustain the image quality improvement at high x-ray energies and for clinical thicknesses without a dose increase, which is a strong indication of the potential to benefit fields such as mammography.

10.2 Future Research Direction

The investigations presented in this dissertation have elucidated extensive future research capabilities. First, continuation of the beam hardening investigation could facilitate significant benefits to the fields of diagnostic imaging, especially mammography. Future studies are needed to perform similar comparisons for the full range of diagnostic x-ray energies, not only to investigate application at clinical mammography energies, but also to evaluate potential application in phase contrast

imaging at high energies for mammography and other fields. In addition, a comprehensive image quality investigation could be performed to allow direct evaluation of the effect of beam hardening on the diagnosis and detection capability.

The development and characterization of high energy phase contrast imaging for this dissertation has also established the need for future research investigations. First, the joint optimization of the x-ray energy and magnification factor must be extended, in an effort to produce a single combination delivering superior image quality. The comparison between the combinations could be made more precise through the use of similar radiation dose instead of object entrance exposure. Therefore, future studies could calculate the associated average glandular dose for each kV/*M* combination when determining the exposure time, in an effort to provide a more effective comparison. In addition, due to the lack of published tables for mammography operation at high energies, the extension of the average glandular dose calculation to the full range of x-ray energies not currently represented would be of considerable clinical and research significance. Next, an evaluation of the tradeoff between quantum efficiency and spatial resolution presented by the computed radiography detection system would identify the type of detector with which to continue the remaining high energy research. As mentioned previously, utilizing the mammography detectors at much higher energies than design specifications results in lowered quantum efficiency, while utilizing the general radiography detectors produces images with much lower resolution. Therefore, an investigation into which

type of detector more effectively balances this tradeoff to provide superior image quality would greatly benefit future studies in high energy phase contrast imaging.

Bibliography

1. A. Karellas, S. Vedantham, "Breast cancer imaging: A perspective for the next decade," Medical Physics **35**(11), 4878-4897 (2008).

2. S. Shapiro, P. Strax, L. Venet, "Periodic breast cancer screening in reducing mortality from breast cancer," Journal of American Medical Association **215**(11), 1775-1785 (1971).

3. L. Tabár, B. Vitak, H. Chen, M. Yen, S. Duffy, R. Smith, "Beyond randomized controlled trials: organized mammographic screening substantially reduces breast carcinoma mortality," Cancer **91**(9), 1724-1731 (2001).

4. E. L. Thurfjell and J. A. Lindgren, "Breast cancer survival rates with mammographic screening: similar favorable survival rates for women younger and those older than 50 years," Radiology **201**(2), 421-426 (1996).

5. S. Moss, "A trial to study the effect on breast cancer mortality of annual mammographic screening in women starting at age 40," J. Med. Screen **6**, 144-148 (1999).

6. R. E. Hendrick, R. A. Smith, J. H. Rutledge III, C. R. Smart, "Benefit of screening mammography in women aged 40-49: a new meta-analysis of randomized controlled trials.," J. Natl. Cancer Inst. Monogr. **22**, 87-92 (1997).

7. K. Kerlikowske, "Efficacy of screening mammography among women aged 40 to 49 years and 50 to 69 years: Comparison of relative and absolute benefit," J. Natl. Cancer Inst. Monogr. **22**, 79-86 (1997).

8. S. Shapiro, "Periodic screening for breast cancer:The HIP Randomized Controlled Trial.," J. Natl. Cancer Inst. Monogr. **1997**(22), 27-30 (1997).

9. L. Tabár, H. Chen, G. Fagerberg, S. Duffy, T. Smith, "Recent results from the Swedish Two-County Trial: the effects of age, histologic type, and mode of detection on the efficacy of breast cancer screening," J. Natl. Cancer Inst. Monogr. **22**, 43-47 (1997).

10. I. Andersson, L. Janzon, "Reduced breast cancer mortality in women under age 50: Updated results from the Malmo Mammographic Screening Program," J. Natl. Cancer Inst. Monogr. **22**, 63-67 (1997).

11. N. Bjurstam, L. Bjorneld, S. Duffy, T. Smith, E. Cahlin, O. Eriksson, L. Hafstrom, H. Lingaas, J. Mattssson, S. Persson, C. Rudenstam, J. Save-Soderbergh, "The Gothenburg breast screening trial: first results on mortality, incidence, and mode of detection for women ages 39-49 years at randomization," Cancer **80**(11), 2091-2099 (1997).

12. UK Trial of Early Detection of Breast Cancer Group, "16-year mortality from breast cancer in the UK Trial of Early Detection of Breast Cancer," Lancet **353**, 1909-1914 (1999).

13. F. Alexander, T. Anderson, H. Brown, A. Forrest, W. Hepburn, A. Kirkpatrick, B. Muir, R. Prescott, A. Smith, "14 years of follow-up from the Edinburgh randomised trial of breast-cancer screening," Lancet **353**(9168), 1903-1908 (1999).

14. A. Miller, T. To, C. Baines, C. Wall, "Canadian National Breast Screening study-2: 13-year results of a randomized trial in women aged 50-59 years," Journal of the National Cancer Institute **92**(18), 1490-1499 (2000).

15. A. Miller, T. To, C. Baines, C. Wall, "The Canadian National Breast Screening Study-1: breast cancer mortality after 11 to 16 years of follow-up. A randomized screening trial of mammography in women age 40 to 49 years," Ann Intern Med **137**(5 Part 1), 305-312 (2002).

16. L. Tabár, B. Vitak, H. Chen, S. Duffy, M. Yen, C. Chiang, U. Krusemo, T. Tot, R. Smith, "The Swedish Two-County Trial twenty years later. Updated mortality results and new insights from long-term follow-up," Radiologic Clinics of North America **38**(4), 625-651 (2000).

17. L. Nystrom, I. Andersson, N. Bjurstam, J. Frisell, B. Nordenskjold, L. Rutqvist, "Long-term effects of mammography screening: updated overview of the Swedish randomised trials," Lancet **359**(9310), 909-919 (2002).

18. L. Bassett, R. Gold, "The evolution of mammography," American Journal of Roentgenology **150**(3), 493-498 (1988).

19. L. Tabár, S. Duffy, B. Vitak, H. Chen, T. Prevost, "The natural history of breast carcinoma: what have we learned from screening?," Cancer **86**(3), 449-462 (1999).

20. J. Bushberg, J. Seibert, E. Leidholdt, Jr., J. Boone *The Essential Physics of Medical Imaging*, Second ed. (Lippincott Williams & Wilkins, Philadephia, Pennsylvania, 2002).

21. C. Kotre, I. Birch, "Phase contrast enhancement of x-ray mammography: a design study," Physics in Medicine and Biology **44**, 2853-2866 (1999).

22. V. Ingal, "Phase mammography-a new technique for breast investigation," Physics in Medicine and Biology **43**, 2555-2567 (1998).

23. P. Monnin, J. Hoszowska, J. Valley, R. Meuli, F. Verdun, "Quantitative characterization of edge enhancement in phase contrast x-ray imaging," Medical Physics **31**(6), 1372-1383 (2004).

24. J. Law, "The development of mammography," Physics in Medicine and Biology **51**, 155-167 (2006).

25. R. Fitzgerald, "Phase-sensitive x-ray imaging," Physics Today **53**, 23-26 (2000).

26. S. Matsuo, T. Katafuchi, K. Tohyama, J. Morishita, K. Yamada, H. Fujita, "Evaluation of edge effect due to phase contrast imaging for mammography," Medical Physics **32**(8), 2690-2697 (2005).

27. A. Pogany, D. Gao, S. Wilkins, "Contrast and resolution in imaging with a microfocus x-ray source," Review of Scientific Instruments **68**(7), 2774-2782 (1997).

28. S. Wilkins, T. Gureyev, D. Gao, A. Pogany, A. Stevenson, "Phase-contrast imaging using polychromatic hard x-rays," Nature **384**(6607), 335-338 (1996).

29. X. Wu, H. Liu, "Clinical implementation of x-ray phase-contrast imaging: theoretical foundations and design considerations," Medical Physics **30**(8), 2169-2179 (2003).

30. F. Arfelli, M. Assante, V. Bonvicini, A. Bravin, G. Cantatore, E. Castelli, L. Dalla Palma, M. Di Michiel, R. Longo, A. Olivo, S. Pani, D. Pontoni, P. Poropat, M. Prest, A. Rashevsky, G. Tromba, A. Vacchi, E. Vallazza, and F. Zanconati, "Low-dose phase contrast x-ray medical imaging," Physics in Medicine and Biology **43**(10), 2845-2852 (1998).

31. E. Donnelly, R. Price, D. Pickens, "Quantification of the effect of system and object parameters on edge enhancement in phase-contrast radiography," Medical Physics **30**(11), 2888-2896 (2003).

32. A. Momose, J. Fukuda, "Phase-contrast radiographs of non-stained rat cerebellar specimen," Medical Physics **22**(4), 375-379 (1995).

33. X. Wu, H. Liu, "A general theoretical formalism for x-ray phase contrast imaging," Journal of X-Ray Science and Technology **11**, 33-42 (2003).

34. M. Freedman, S. Lo, C. Honda, E. Makariou, G. Sisney, E. Pien, H. Ohara, A. Ishisaka, F. Shimada, "Phase contrast digital mammography using molybdenum x-ray: clinical implications in detectability improvement," SPIE **5030**, 533-540 (2003).

35. T. Tanaka, C. Honda, S. Matsuo, K. Noma, H. Oohara, N. Nitta, S. Ota, K. Tsuchiya, Y. Sakashita, A. Yamada, M. Yamasaki, A. Furukawa, M. Takahashi, and K. Murata, "The first trial of phase contrast imaging for digital full-field mammography using a practical molybdenum X-ray tube," Investigative Radiology **40**(7), 385-396 (2005).

36. D. Zhang, M. Donovan, L. Fajardo, A. Archer, X. Wu, H. Liu, "Preliminary feasibility study of an in-line phase contrast x-ray imaging prototype," IEEE Transactions on Biomedical Engineering **55**(9), 2249-2257 (2008).

37. E. Donnelly, R. Price, "Quantification of the effect of kVp on edge-enhancement index in phase-contrast radiography," Medical Physics **29**(6), 999-1002 (2002).

38. Y. Zhou, H. Pew, J. Rong, W. Chen, L. Fajardo, X. Wu, H. Liu, "Phantom imaging with a prototype phase contrast radiography system," SPIE **6163**, 61630E (2006).

39. B. Hasegawa, *The Physics of Medical X-Ray Imaging* (Medical Physics Publishing Corporation, Madison, Wisconsin, 1990).

40. J. Launders, A. Cowen, R. Bury, P. Hawkridge, "Towards image quality, beam energy and effective dose optimisation in digital thoracic radiography," European Radiology **11**, 870-875 (2001).

41. H. P. McAdams, E. Samei, J. Dobbins, III, G. D. Tourassi, and C. E. Ravin, "Recent Advances in Chest Radiography," Radiology **241**(3), 663-683 (2006).

42. S. Metz, P. Damoser, R. Hollweck, R. Roggel, C. Engelke, K. Woertler, B. Renger, E. J. Rummeny, and T. M. Link, "Chest radiography with a digital flat-panel detector: Experimental receiver operating characteristic analysis," Radiology **234**(3), 776-784 (2005).

43. M. Uffmann, U. Neitzel, M. Prokop, N. Kabalan, M. Weber, C. J. Herold, and C. Schaefer-Prokop, "Flat-Panel-Detector Chest Radiography: Effect of Tube Voltage on Image Quality," Radiology **235**(2), 642-650 (2005).

44. M. Donovan, D. Zhang, W. Chen, H. Liu "The characterization of a phase contrast x-ray imaging prototype," SPIE **6436**(643608), 9 pages (2007).

45. E. F. Donnelly, R. R. Price, and D. R. Pickens, "Experimental validation of the Wigner distributions theory of phase-contrast imaging," Medical Physics **32**(4), 928-931 (2005).

46. A. Papoulis, S. Pillai, *Probability, Random Variables and Stochastic Processes,* Fourth Edition ed. (McGraw-Hill, New York City, New York, 2002).

47. R. Larsen, M. Marx, *An Introduction to Mathematical Statistics and Its Applications,* Fourth ed. (Pearson Prentice Hall, Upper Saddle River, NJ, 2006).

48. R. Blackwell, "Contrast thresholds of the human eye," Journal of the Optical Society of America **36**, 624-643 (1946).

49. A. Rose, "The sensitivity performance of the human eye on an absolute scale," Journal of the Optical Society of America **38**, 196-208 (1948).

50. A. Rose, *Vision: Human and Electronic* (Plenum, New York, 1974).

51. M. Donovan, D. Zhang, H. Liu, "Step by step approach toward optimal MTF algorithm using an edge test device," Journal of X-Ray Science and Technology **March**(2009).

52. E. Samei, M. Flynn, D. Reimann, "A method for measuring the presampled MTF of digital radiographic systems using an edge test device," Medical Physics **25**(1), 102-113 (1998).

53. E. Samei, N. Ranger, J. Dobbins III, Y. Chen, "Intercomparison of methods for image quality characterization. I. Modulation transfer function," Medical Physics **33**(5), 1454-1465 (2006).

54. H. Fujita, D. Tsai, T. Itoh, K. Doi, J. Morishita, K. Ueda, A. Ohtsuka, "A Simple Method for Determining the Modulation Transfer Function in Digital Radiography," IEEE Transactions on Medical Imaging **11**(1), 34-39 (1992).

55. P. Judy, "The line spread function and modulation transfer function of a computed tomography scanner," Medical Physics **3**(4), 233-236 (1976).

56. F. Yin, M. Giger, K. Doi, "Measurement of the presampling modulation transfer function of film digitizers using a curve fitting technique," Medical Physics **17**(6), 962-966 (1990).

57. C. Bradford, W. Peppler, J. Waidelich, "Use of a slit camera for MTF measurements," Medical Physics **26**(11), 2286-2294 (1999).

58. M. Giger, K. Doi, "Investigation of basic imaging properties in digital radiography. 1. Modulation transfer function," Medical Physics **11**(3), 287-295 (1984).

59. J. Boone, J. Seibert, "An analytical edge spread function model for computer fitting and subsequent calculation of the LSF and MTF," Medical Physics **21**(10), 1541-1545 (1994).

60. E. Buhr, S. Gunther-Kohfahl, U. Neitzel, "Accuracy of a simple method for deriving the presampled modulation transfer function of a digital radiographic system from an edge image," Medical Physics **30**(9), 2323-2331 (2003).

61. A. Carton, D. Vandenbroucke, L. Struye, A. Maidment, Y. Kao, M. Albert, H. Bosmans, G. Marchal, "Validation of MTF measurement for digital mammography quality control," Medical Physics **32**(6), 1684-1695 (2005).

62. I. Cunningham, B. Reid, "Signal and noise in modulation transfer function determinations using the slit, wire, and edge techniques," Medical Physics **19**(4), 1037-1044 (1992).

63. J. Dobbins III, "Effects of undersampling on the proper interpretation of modulation transfer function, noise power spectra, and noise equivalent quanta of digital imaging systems," Medical Physics **22**(2), 171-181 (1995).

64. P. Greer, T. van Doorn, "Evaluation of an algorithm for the assessment of the MTF using an edge method," Medical Physics **27**(9), 2048-2059 (2000).

65. U. Neitzel, S. Gunther-Kohfahl, G. Borasi, E. Samei, "Determination of the detective quantum efficiency of a digital x-ray detector: Comparison of three evaluations using a common image data set," Medical Physics **31**(8), 2205-2211 (2004).

66. E. Samei, E. Buhr, P. Granfors, D. Vandenbroucke, X. Wang, "Comparison of edge analysis techniques for the determination of the MTF of digital radiographic systems," Physics in Medicine and Biology **50**, 3613-3625 (2005).

67. S. Mitra, *Digital Signal Processing: A Computer-Based Approach,* Third ed. (McGraw-Hill, New York, 2006).

68. J. Dobbins III, D. Ergun, L. Rutz, D. Hinshaw, H. Blume, D. Clark, "DQE(f) of four generations of computed radiography acquisition devices," Medical Physics **22**(10), 1581-1593 (1995).

69. J. Dobbins III, E. Samei, N. Ranger, Y. Chen, "Intercomparison of methods for image quality characterization. II. Noise power spectrum," Medical Physics **33**(5), 1466-1475 (2006).

70. M. Flynn, E. Samei, "Experimental comparison of noise and resolution for 2k and 4k storage phosphor radiography systems," Medical Physics **26**(8), 1612-1623 (1999).

71. ICRU, "Medical Imaging - The Assessment of Image Quality," International Commission on Radiation Units and Measurements **54**(1996).

72. H. Jiang, W. Chen, H. Liu, "Techniques to improve the accuracy and to reduce the variance in noise power spectrum measurement," IEEE Transactions on Biomedical Engineering **49**(11), 1270-1278 (2002).

73. D. Zhang, J. Rong, R. Chu, X. Wu, H. Liu, "Imaging characteristics of a high resolution computed radiography system," Journal of X-Ray Science and Technology **14**, 273-282 (2006).

74. M. Williams, P. Mangiafico, P. Simoni, "Noise power spectra of images from digital mammography detectors," Medical Physics **26**(7), 1279-1293 (1999).

75. W. Hillen, U. Schiebel, T. Zaengel, "Imaging performance of a digital storage phosphor system," Medical Physics **14**(5), 744-751 (1987).

76. E. Samei, M. Flynn, "An experimental comparison of detector performance for computed radiography systems," Medical Physics **29**(4), 447-459 (2002).

77. R. Aufrichtig, "Comparison of low contrast detectability between a digital amorphous silicon and a screen-film based imaging system for thoracic radiography," Medical Physics **26**(7), 1349-1358 (1999).

78. H. Liu, L. Fajardo, J. Barrett, R. Baxter, "Contrast-detail detectability analysis: comparison of a digital spot mammography system and an analog screen-film mammography system," Academic Radiology **4**(3), 197-203 (1997).

79. B. Pogue, C. Willscher, T. McBride, U. Osterberg, K. Paulsen, "Contrast-detail analysis for detection and characterization with near-infrared tomography," Medical Physics **27**(12), 2693-2700 (2000).

80. X. Rong, C. Shaw, X. Liu, M. Lemacks, S. Thompson, "Comparison of an amorphous silicon/cesium iodide flat-panel digital chest radiography system with screen/film and computed radiography systems - a contrast-detail phantom study," Medical Physics **28**(11), 2328-2335 (2001).

81. Q. Zhang, Y. Li, B. Steele, X. Wu, W. Chen, J. Rong, H. Liu, "Comparison of a CMOS-based and a CCD-based digital x-ray imaging system: observer studies," Journal of Electronic Imaging **14**(2), 23002 (23006 pages) (2005).

82. H. Liu, L. Fajardo, R. Baxter, "A theoretical model for contrast-detail detectability prediction in digital radiography," SPIE **2676**, 116-121 (1996).

83. G. Cohen, D. McDaniel, L. Wagner, "Analysis of variations in contrast-detail experiments," Medical Physics **11**(4), 469-473 (1984).

84. V. A. Gurvich, "Statistical approach for image quality evaluation in daily medical practice," Medical Physics **27**(1), 94-100 (2000).

85. O. Hamer, M. Volk, N. Zorger, S. Feuerbach, M. Strotzer, "Amorphous silicon, flat-panel, x-ray detector versus storage phosphor-based computed radiography: contrast-detail phantom study at different tube voltages and detector entrance doses," Investigative Radiology **38**(4), 212-220 (2003).

86. K. Imai, M. Ikeda, T. Niimi, "The application of Markov theory to contrast-detail analysis," Academic Radiology **13**, 152-158 (2006).

87. J. Thomas, K. Chakrabarti, R. Kaczmarek, A. Romanyukha, "Contrast-detail phantom scoring methodology," Medical Physics **32**(3), 807-814 (2005).

88. A. Burgess, "Comparison of ROC and forced choice observer performance," Medical Physics **22**(5), 643-655 (1995).

89. S. Peer, U. Neitzel, S. Giacomuzzi, R. Peer, E. Gassner, I. Steingruber, W. Jaschke, "Comparison of low-contrast detail perception on storage phosphor radiographs and digital flat panel detector images," IEEE Transactions on Medical Imaging **20**(3), 239-242 (2001).

90. K. R. Bijkerk, J. M. Lindeijer, and M. A. O. Thijssen, "Manual, CDMAM-Phantom," Department of Diagnostic Radiology, University Hospital Nijmegen, St. Radboud **4**(7)(1995).

91. R. Hendrick, L. Bassett, M. Botsco, P. Butler, G. Dodd, S. Feig, J. Gray, A. Haus, M. Harvey, R. Heinlein, R. Holland, E. Kitts Jr., R. McLelland, J. McCrohan, R. Rossi, D. Sullivan, "Mammography Quality Control Manual," American College of Radiology, pp. 43-51 (1994).

92. N. Associates, "Manual, Mammographic Accreditation Phantom," Nuclear Associates **Model 18-220**(1999).

93. E. A. Berns, R. Edward Hendrick, Gary R. Cutter, "Performance comparison of full-field digital mammography to screen--film mammography in clinical practice," Medical Physics **29**(5), 830-834 (2002).

94. M. Wong, X. Wu, H. Liu, "Image quality comparison of high energy phase contrast x-ray images with low energy conventional images: phantom studies," SPIE Proceedings on Dynamics and Fluctuations in Biomedical Photonics VII **7563**(756305), 9 (2010).

95. A. Fandos-Morera, M. Prats-Esteve, J. Tura-Soteras, A. Traveria-Cros, "Breast tumors: composition of microcalcifications," Radiology **169**, 325-327 (1988).

96. M. Galkin, S. Feig, A. Patchefsky, J. Rue, W. Gamblin, D. Gomez, L. Marchant, "Ultrastructure and microanalysis of 'benign' and 'malignant' breast calcifications," Radiology **124**, 245-249 (1977).

97. S. Olson, B. Fam, P. Winter, F. Scholz, A. Lee, S. Gordon, "Breast calcifications: analysis of imaging properties," Radiology **169**(329-332)(1988).

98. E. Sickles, "Mammographic features of "early" breast cancer," American Journal of Roentgenology **143**, 461-464 (1984).

99. IEC, "Medical electrical equipment - Characteristics of digital imaging devices - Part 1: Determination of the detective quantum efficiency," International Electrotechnical Commission International Standard 62220-1 (2003).

100. J. Dainty, R. Shaw, *Image Science* (Academic Press, New York, 1974).

101. H. Liu, L. Fajardo, B. Penny, "Signal-to-noise ratio and detective quantum efficiency analysis of optically coupled CCD mammography imaging systems," Academic Radiology **3**(10), 799-805 (1996).

102. P. Granfors, R. Aufrichtig, "Performance of a 41x41-cm^2 amorphous silicon flat panel x-ray detector for radiographic imaging applications," Medical Physics **27**(6), 1324-1331 (2000).

103. M. Wong, D. Zhang, J. Rong, X. Wu, H. Liu, "Optimizing photon fluence measurements for the accurate determination of detective quantum efficiency," Journal of Electronic Imaging **18**(4), 043010 (2009).

104. J. Sandrik, R. Wagner, "Absolute measures of physical image quality: Measurement and application to radiographic magnfication," Med Phys **9**(4), 540-549 (1982).

105. K. Fetterly, N. Hangiandreou, B. Schueler, E. Ritenour, "Measurement of the presampled two-dimensional modulcation transfer function of digital imaging systems," Med Phys **29**(5), 913-921 (2002).

106. J. Boone, J. Seibert, "An accurate method for computer-generating tungsten anode x-ray spectra from 30 to 140 kV," Medical Physics **24**(11), 1661-1670 (1997).

107. D. Zhang, X. Wu, M. Wong, Y. Ni, J. Rong, W. Chen, H. Liu, "Error analysis in the measurement of x-ray photon fluence: an analysis on the uncertainty from energy calibration," SPIE Proceedings on Dynamics and Fluctuations in Biomedical Photonics **7176**(7176OI)(2009).

108. U. Bottigli, B. Golosio, G. Masala, P. Oliva, S. Stumbo, P. Delogu, M. Fantacci, L. Abbene, F. Fauci, G. Raso, "Comparison of two portable solid state detectors with an improved collimation and alignment device for mammographic x-ray spectroscopy," Medical Physics **33**(9), 3469-3477 (2006).

109. S. Miyajima, K. Imagawa, M. Matsumoto, "An alignment method for mammographic X-ray spectroscopy under clinical conditions," British Journal of Radiology **75**(897), 763-766 (2002).

110. K. Nishizawa, H. Maekoshi, Y. Kamiya, Y. Kobayashi, K. Ohara, S. Sakuma, "Alignment of x-ray tube focal spots for spectral measurement," Medical Physics **9**(2), 284-287 (1982).

111. W. Huda, E. Nickoloff, J. Boone, "Overview of patient dosimetry in diagnostic radiology for the past 50 years," Medical Physics **35**(12), 5713-5728 (2008).

112. F. Arfelli, M. Assante, V. Bonvicini, A. Bravin, G. Cantatore, E. Castelli, L. Dalla Palma, M. Di Michiel, R. Longo, A. Olivo, S. Pani, D. Pontoni, P. Poropat, M. Prest, A. Rashevsky, G. Tromba, A. Vacchi, E. Vallazza, F. Zanconati, "Low-dose phase contrast x-ray medical imaging," Physics in Medicine and Biology **43**, 2845- (1998).

113. C. Kimme-Smith, L. Bassett, R. Gold, "Evaluation of Radiation Dose, Focal Spot, and Automatic Exposure of Newer Film-Screen Mammography Units," American Journal of Roentgenology **149**, 913-917 (1987).

114. Q. Wang, X. Wu, W. Chen, J. Cheung, H. Liu, "Quantum efficiency of a digital x-ray imaging system for small animal studies," Proceedings of SPIE in Advanced Biomedial and Clinical Diagnostic Systems II **5318**, 94-98 (2004).

115. Q. Zhang, J. Rong, X. Wu, Y. Li, W. Chen, H. Liu, "Impacts of filtration on contrast-detail detectability of an x-ray imaging system," International Journal of Biomedical Imaging **2006**(95754), 1-8 (2006).

116. X. Wu, H. Liu, "An experimental method of determining relative phase-contrast factor for x-ray imaging systems," Medical Physics **31**(5), 997-1002 (2004).

117. J. Jansen, W. Veldkamp, M. Thijssen, S. van Woudenberg, J. Zoetelief, "Method for determination of the mean fraction of glandular tissue in individual female breasts using mammography," Physics in Medicine and Biology **50**, 5953-5967 (2005).

118. J. Zoetelief, N. de Wit, J. Broerse, "Dosimetric aspects of film/screen mammography: In-phantom dosimetry with thimble-type ionisation chambers," Physics in Medicine and Biology **34**(9), 1169-1177 (1989).

119. W. Argo, K. Hintenlang, D. Hintenlang, "A tissue-equivalent phantom series for mammography dosimetry," Journal of Applied Clinical Medical Physics **5**(4), 112-119 (2004).

120. H. Warren-Forward, Duggan, L., "Towards in vivo TLD dosimetry in mammography," British Journal of Radiology **77**(917), 426-432 (2004).

121. L. Hartley, B. Cobb, D. Hutchinson, "Estimating mean glandular dose using proprietary mammography phantoms," Applied Radiation and Isotopes **50**(1), 205-213 (1999).

122. CIRS, "Mammography BR3D Phantom Model 020 User Guide and Technical Information," Computerized Imaging Reference Systems, Inc. (2009).

123. W. Mendenhall, T. Sincich, *Statistics for Engineering and the Sciences*, 5th Edition ed. (Prentice Hall, Upper Saddle River, New Jersey, 2007).

124. ANSI/ASME, *Test Uncertainty*, ANSI/ASME PTC 19.1 (American National Standards Institute / American Society of Mechanical Engineers, New York, 1998).

125. ISO, *Guide to the expression of uncertainty in measurement*, First ed. (International Organization for Standardization (ISO), Geneva, 1993).

126. G. Upton, and I. Cook, *Oxford Dictionary of Statistics*, Second ed. (Oxford University Press, 2006).

127. S. Sasaki, "Numerical Tables of Anomalous Scattering Factors Calculated by the Cromer and Liberman's Method," National Laboratory for High Energy Physics (KEK Report No. 88-14)(1989).

128. S. Sasaki, "X-Ray Absorption Coefficients of the Elements (Li to Bi, U)," National Laboratory for High Energy Physics (KEK Report No. 90-16)(1990).

129. D. Chapman, W. Thomlinson, R. Johnston, D. Washburn, E. Pisano, N. Gmur, Z. Zhong, R. Menk, F. Arfelli, D. Sayers, "Diffraction enhanced x-ray imaging," Physics in Medicine and Biology **42**, 2015-2025 (1997).

130. M. Kiss, D. Sayers, Z. Zhong, "Measurement of image contrast using diffraction enhanced imaging," Physics in Medicine and Biology **48**, 325-340 (2003).

131. E. Pisano, R. Johnston, D. Chapman, J. Geradts, M. Iacocca, C. Livasy, D. Washburn, D. Sayers, Z. Zhong, M. Kiss, W. Thomlinson, "Human breast cancer specimens: diffraction-enhanced imaging with histologic correlation-improved conspicuity of lesion detail compared with digital radiography," Radiology **214**, 895-901 (2000).

132. T. Takeda, A. Momose, K. Hirano, S. Haraoka, T. Watanabe, Y. Itai, "Human carcinoma: early experience with phase-contrast x-ray CT with synchrotron radiation - comparative specimen sudy with optical microscopy," Radiology **214**, 298-301 (2000).

133. Institute of Physical Sciences in Medicine, "The Commissioning and Routine Testing of Mammographic X-Ray Systems," IPSM Group Report 59 (1989).

134. J. Bailar, "Screening for early breast cancer: pros and cons," Cancer **39**, 2783-2795 (1977).

135. P. C. Gotzsche, O. Olsen, "Is screening for breast cancer with mammography justifiable?," Lancet **355**, 129-134 (2000).

136. O. Olsen, Gotzsche, P. C., "Screening for breast cancer with mammography," Cochrane Database Sys Rev **4**(CD001877)(2001).

137. R. Smith, D. Saslow, K. Sawyer, W. Burke, M. Costanza, W. P. Evans III, R. Foster, Jr., E. Hendrick, H. Eyre, S, Sener, "American Cancer Society Guidelines for Breast Cancer Screening: Update 2003," CA Cancer J Clin **53**(3), 141-169 (2003).

138. American College of Radiology, "Mammography Quality Control Manual," ACR (1994).

139. American Association of Physicists in Medicine, "Equipment requirements and quality control for mammography," AAPM Report 29 (1990).

140. International Commission on Radiological Protection, "Managing patient dose in digital radiology," ICRP Report 93 (2003).

141. National Council on Radiation Protection and Measurements, "Mammography - a user's guide," NCRP Report Number 85, 40-48 (1986).

142. Food and Drug Administration, "Mammography Program (MQSA)," www.fda.gov/cdrh/mammography (1992).

143. J. Boone, T. Fewell, R. Jennings, "Molybdenum, rhodium, and tungsten anode spectral models using interpolating polynomials with application to mammography," Medical Physics **24**(12), 1863-1874 (1997).

144. J. Boone, "Glandular Breast Dose for Monoenergetic and High-Energy X-ray Beams: Monte Carlo Assessment," Radiology **213**(1), 23-37 (1999).

145. J. Boone, "Normalized glandular dose (DgN) coefficients for arbitrary x-ray spectra in mammography: Computer-fit values of Monte Carlo derived data," Medical Physics **29**(5), 869-875 (2002).

146. D. Dance, C. Skinner, K. Young, J. Beckett, C. Kotre, "Additional factors for the estimation of mean glandular breast dose using the UK mammography dosimetry protocol," Physics in Medicine and Biology **45**, 3225-3240 (2000).

147. D. R. Dance, "Monte Carlo calculation of conversion factors for the estimation of mean glandular breast dose," Physics in Medicine and Biology **35**(9), 1211 (1990).

148. D. R. Dance, A. K. Thilander, M. Sandborg, C. L. Skinner, I. A. Castellano, and G. A. Carlsson, "Influence of anode/filter material and tube potential on contrast, signal-to-noise ratio and average absorbed dose in mammography: a Monte Carlo study," Br J Radiol **73**(874), 1056-1067 (2000).

149. R. E. Hendrick, "Standardization of image quality and radiation dose in mammography," Radiology **174**, 648-654 (1990).

150. M. Rosenstein, L. Andersen, G. Warner, *Handbook of glandular tissue doses in mammography* (United States Government Printing Office, Washington, D.C., 1985), Vol. HHS (FDA) Publication Number 85-8243.

151. S. Skubic, P. Fatouros, "Absorbed breast dose: dependence on radiographic modality and technique, and breast thickness," Radiology **161**, 263-270 (1986).

152. X. Wu, G. Barnes, D. Tucker, "Spectral dependence of glandular tissue dose in screen-film mammography," Radiology **179**, 143-148 (1991).

153. X. Wu, "Breast Dosimetry in Screen Film Mammography," Screen Film Mammography: Imaging Considerations and Medical Physics Responsibilities, 159-175 (1991).

154. X. Wu, E. Gingold, G. Barnes, D. Tucker, "Normalized Average Glandular Dose in Molybdenum Target-Rhodium Filter and Rhodium Target-Rhodium Filter Mammography," Radiology **193**(1), 83-89 (1994).

155. G. Hammerstein, D. Miller, D. White, M. Masterson, H. Woodard, J. Laughlin, "Absorbed radiation dose in mammography," Radiology **130**, 485-491 (1979).

156. R. Kinsey, "Data formats and procedures for the Evaluated Nuclear Data File, ENDF," BNL-NCS-50496(Ed.2) United StatesWed Feb 06 15:01:46 EST 2008NTIS, PC A24/MF A01.BNL; INS-80-018233; ERA-06-001540; EDB-80-125508English (1979).

157. I. A. Brezovich, S. Jordan, "A device for precision positioning and alignment of room lasers to diminish their contribution to patient setup errors," J Appl Clin Med Phys **8**(4), 2398 (2007).

158. R. T. Droege, "A megavoltage MTF measurement technique for metal screen-film detectors," Med Phys **6**(4), 272-279 (1979).

159. E. R. Epp and H. Weiss, "Experimental study of the photon energy spectrum of primary diagnostic x-rays," Phys Med Biol **11**(2), 225-238 (1966).

160. H. Kubota, Y. Ozaki, M. Matsumoto, and H. Kanamori, "Determination of x-ray tube focal spot position," Med Phys **20**(4), 1029-1031 (1993).

161. H. MacMahon, N. J. Yasillo, and M. Carlin, "Laser alignment system for high-quality portable radiography," Radiographics **12**(1), 111-120 (1992).

162. D. Zhang, M. Wong, X. Wu, H. Liu, "A convenient alignment approach for x-ray imaging experiments based on laser positioning devices," Medical Physics **35**(11), 4907-4910 (2008).

163. Amptek, *Amptek Multi-Channel Analyzer 8000A Instruction Manual* (Amptek Incorporated, Bedford, MA, 2002).

164. G. Lubberts, "The line spread function and the modulation transfer function of x-ray fluorescent screen-film systems - problems with double-coated films," American Journal of Roentgenology **105**(4), 909-917 (1969).

165. K. Rossmann, G. Sanderson, "Validity of the Modulation Transfer Function of Radiographic Screen-Film Systems Measured by the Slit Method," Physics in Medicine and Biology **13**(2), 259-268 (1968).

166. H. Fujita, K. Ueda, J. Morishita, T. Fujikawa, A. Ohtsuka, T. Sai "Basic imaging properties of a computed radiography system with photostimulable phosphors," Medical Physics **16**(1), 52-59 (1989).

167. N. W. Marshall, "Early experience in the use of quantitative image quality measurements for the quality assurance of full field digital mammography x-ray systems," Physics in Medicine and Biology **52**, 5545-5568 (2007).

168. S. Reichenbach, S. Park, R. Narayanswamy, "Characterizing digital image acquisition devices," Optical Engineering **30**(2), 170-177 (1991).

169. A. Tabatabai, O. Mitchell, "Edge location to subpixel values in digital imagery," IEEE Transactions on Pattern Analysis and Machine Intelligence **6**, 188-201 (1984).

170. W. Pratt, *Digital Image Processing* (Wiley, New York City, New York, 1991).

171. R. Haralick, L. Shapiro, *Computer and Robot Vision* (Addison-Wesley, Reading, Massachusetts, 1992), Vol. Vol. 1.

172. J. Princen, J. Illingworth, J. Kittler, "A formal definition of the hough transform: Properties and relationships," Journal of Mathematical Imaging and Vision **1**(2), 153-168 (1992).

173. D. Ballard, "Generalizing the Hough transform to detect arbitrary shapes," Pattern Recognition **13**(2), 111-122 (1981).

174. O. Chutatape, L. Guo, "A modified Hough transform for line detection and its performance " Pattern Recognition **32**(2), 181-192 (1999).

175. R. Duda, P. Hart, "Use of the Hough transformation to detect lines and curves in pictures," Coummunications of the ACM **15**(1), 11-15 (1971).

176. J. Canny, "A computational approach to edge detection," IEEE Transactions on Pattern Analysis and Machine Intelligence **8**(6), 679-698 (1986).

177. I. Abdel-Qader, O. Abudayyeh, M. Kelly, "Analysis of edge-detection techniques for crack identification in bridges," Journal of Computing in Civil Engineering **17**(4), 255-263 (2003).

178. P. Worthington, "Enhanced Canny edge detection using curvature consistency," IEEE Proceedings on Pattern Recognition **1**(11-15), 596-599 (2002).

179. S. Chang, L. Gong, M. Li, X. Hu, J. Yan, "Small retinal vessal extraction using modified Canny edge detection," IEEE Proceedings on Audio, Language and Image Processing, 125-1259 (2008).

180. M. Ali, D. Clausi, "Using the Canny edge detector for feature extraction and enhancement of remote sensing images," IEEE International Geoscience and Remote Sensing Symposium **5**, 2298-2300 (2001).

181. T. Lindeberg, "Edge detection and ridge detection with automatic scale selection," International Journal of Computer Vision **30**(2), 117 - 154 (1998).

182. K. Fetterly, N. Hangiandreou, "Image quality evaluation of a desktop computed radiography system," Medical Physics **27**(12), 2669-2679 (2000).

183. R. Saunders, E. Samei, "A method for modifying the image quality parameters of digital radiographic images," Medical Physics **30**(11), 3006-3017 (2003).

184. I. Cunningham, A. Fenster, "A method for modulation transfer function determination from edge profiles with correction for finite-element differentiation," Medical Physics **14**(4), 533-537 (1987).

185. E. Samei, M. Flynn, "An experimental comparison of detector performance for direct and indirect radiography systems," Medical Physics **30**(4), 608-622 (2003).

186. Oxford, "UltraBright Microfocus X-Ray Source," X-Ray Technology, Inc. **Scott Valley, CA**(2006).

187. E. Elbakri, M. Tesic, Q. Xiong, "Physical characterization of a high-resolution CCD detector for mammography," Physics in Medicine and Biology **52**, 2171-2183 (2007).

188. E. Storm, "Calculated bremsstrahlung spectra from thick tungsten targets," Physical Review A **5**(6), 2328-2338 (1972).

189. E. Storm, "Emission of characteristic L and K radiation from thick tungsten targets," Journal of Applied Physics **43**(6), 2790-2796 (1972).

190. Radcal, *Model 9095 Measurement System Instruction Manual* (Radcal Corporation, Monrovia, California, 2005).

191. S. Vedantham, A. Karellas, S. Suryanarayanan, D. Albagli, S. Han, E. Tkaczyk, C. Landberg, B. Opsahl-Ong, P. Granfors, I. Levis, C. D'Orsi, R. Hendrick, "Full breast digital mammography with an amorphous silicon-based flat panel detector: Physical characteristics of a clinical prototype," Medical Physics **27**(3), 558-567 (2000).

192. R. Redus, J. Pantazis, T. Pantazis, A. Huber, B. Cross, "Characterization of CdTe detectors for quantitative x-ray spectroscopy," Submitted to IEEE Transactions on Nuclear Science (2007).

193. M. Wong, X. Wu, and H. Liu, "Preliminary investigation on the effect of x-ray beam hardening on detective quantum efficiency and radiation dose," presented at the Image Analysis & Interpretation (SSIAI), 2010 IEEE Southwest Symposium on, 23-25 May 2010, 2010.

194. D. White, R. Martin, R. Darlison, "Epoxy resin based tissue substitutes," British Journal of Radiology **50**(599), 814-821 (1977).

195. M. Wong, X. Wu, H. Liu, "The effects of x-ray beam hardening on detective quantum efficiency and radiation dose," Submitted to Medical Physics (2011).

196. M. Wong, X. Wu, H. Liu, "Preliminary investigation of a high energy in-line phase contrast x-ray imaging system: Phantom studies," Submitted to Medical Physics (2011).

197. CIRS, "Mammography BR3D Phantom Manual," CIRS Tissue Simulation and Phantom Technology (2009).

198. M. Wong, X. Wu, H. Liu, "Image quality and dose efficiency of high energy phase contrast x-ray imaging: Phantom studies," Preparing for Submission (2011).